

REPORT DOCUMENTATION PAGE

FORM APPROVED
OMB No. 0704-0188

Public reporting burden for this collection of information is estimated to average 1 hour per response, including the time for reviewing instructions, searching existing data sources, gathering and maintaining the data needed and completing and reviewing the collection of information. Send comments regarding this burden estimate or any other aspect of the collection of information, including suggestions for reducing the burden to Washington Headquarters Services, Directorate for Information Operations and Reports, 1215 Jefferson Davis Highway, Suite 1204, Arlington, VA 22202-4302 and to the Office of Management and Budget, Paperwork Reduction Project (0704-0188), Washington, DC 20503.

1. AGENCY USE ONLY (Leave blank)	2. REPORT DATE 4/30/97	3. REPORT TYPE AND DATES COVERED Final 03/01/90-09/30/95
4. TITLE AND SUBTITLE OF REPORT Fracture Analysis of Diamond Materials		5. FUNDING NUMBERS N00014-90-J-1726
6. AUTHOR(S) J.J. Mecholsky, Jr Lucien P. Hehn		
7. PERFORMING ORGANIZATION NAME(S) AND ADDRESS(ES) University of Florida Division of Sponsored Research 208 Grinter Hall Gainesville, Florida 32611		8. PERFORMING ORGANIZATION REPORT NUMBER: 4910 4509268-12 4910 4509431-12 B
9. SPONSORING/MONITORING AGENCY NAME(S) AND ADDRESS(ES) Office of Naval Research 800 North Quincy St. Arlington, VA 22217-5660		10. SPONSORING/MONITORING AGENCY REPORT NUMBER:
11. SUPPLEMENTARY NOTES:		
12a. DISTRIBUTION AVAILABILITY STATEMENT Unlimited		
13. ABSTRACT (Maximum 200 words) Polycrystalline CVD diamond disks were fractured in ball-on-ring loading. Fractographic analysis was performed on the fractured specimens using both optical and scanning electron microscopy. Fracture surface analysis was used to locate and measure the size of the failure initiating critical flaws in over 60 specimens. The combined data from the different sources showed that different processing conditions could lead to widely varying fracture toughness values. The strength was found to be an unreliable material property measure as it was found to vary strongly with thickness whereas the fracture toughness, K_{Ic} , was independent of sample thickness. Residual stresses in (2.5 to 15 μ m thick) diamond coatings deposited on (110) surfaces of single crystal silicon by hot-filament CVD were measured using both the $\sin^2\psi$ X-ray diffraction method and a curvature technique. The curvature method verified the results of the X-ray diffraction technique. Residual stresses in the coatings were found to be in tensile and in the range 65-355 MPa. This is opposite in sign and different in magnitude to that predicted by thermal expansion mismatch, indicating the presence of intrinsic stresses. We determined the presence of a temperature independent "intrinsic" stress of about 520 ± 75 MPa.		
14. SUBJECT TERMS Diamond Materials		15. NUMBER OF PAGES: 123
		16. PRICE CODE
17. SECURITY CLASSIFICATION OF REPORT:	18. SECURITY CLASSIFICATION OF THIS PAGE	19. SECURITY CLASSIFICATION OF ABSTRACT
		20. LIMITATION OF ABSTRACT Unlimited

FRACTURE ANALYSIS DIAMOND MATERIALS

Lucien P. Hehn and J.J. Mecholsky, Jr.
Department of Materials Science & Engineering
University of Florida

FINAL REPORT
on
ONR Grant# N00014-90-J-1726

MAY 1997

TABLE OF CONTENTS

	<u>Page</u>
ABSTRACT.....	v
CHAPTERS	
1 INTRODUCTION.....	1
Background.....	1
Polycrystalline/Single Crystal Toughness Ratio.....	3
Outline of Study.....	3
2 MECHANICS.....	5
Fracture Mechanics.....	5
Loading of Samples.....	7
3 FRACTURE SURFACE ANALYSIS.....	12
The Characteristic Features of Brittle Fracture.....	12
Analysis of Macroscopic Crack Branching Patterns.....	14
Locating the Origin of Failure.....	14
Determination of Strength and Toughness.....	20
Indentation Toughness Measurements.....	20
Cleavage Marks.....	26
River Marks.....	26
Examination of Matching Halves of Fracture Surface.....	27
Growth Surface Cracks.....	28
4 RESULTS OF OTHER STUDIES.....	31
Fracture Toughness (K_{Ic}) of Polycrystalline CVD Diamond.....	31
Strength of Polycrystalline CVD Diamond.....	32
Transgrannular and Intergrannular Fracture.....	33
Residual Stress Measurement in CVD Diamond Deposited on Silicon.....	34
5 STRENGTH AND FRACTURE RESULTS FOR GROUP A, SAMPLE SET A.I.....	35
The Texas Instruments Study.....	35
Strength vs Thickness.....	35
Maximum Stress and Failure Load vs Thickness.....	37
Maximum Stress vs Load.....	40
Relationships Between Flaw Size, Sample Thickness, Fracture Toughness, and Strength.....	43
Sharp vs. Blunt Cracks.....	52

6 FLAW SHAPE DISTRIBUTION.....	53
7 RESULTS OBTAINED FROM SAMPLES FROM OTHER SOURCES.....	57
Description of Figures.....	57
Fracture Toughness, Flaw Size, and Sample Thickness.....	57
Strength, Maximum Stress, Critical Flaw Size, and Sample Thickness.....	63
8 THE EFFECT OF SAMPLE POLISHING AND CHOICE OF SAMPLE FRACTURE SURFACE.....	64
Fracture of Polished Specimens.....	64
Fracture on the Substrate Surface.....	64
9 MAXIMUM STRESS AS A MEASURE OF STRENGTH.....	68
Motivation.....	68
Background.....	68
Justification.....	70
10 MEASUREMENT OF RESIDUAL STRESSES IN CVD DIAMOND DEPOSITED ON SILICON.....	74
Introduction.....	74
Experimental Details.....	75
X-ray stress Measurement Conditions.....	77
Zero-Stress Reference.....	79
Curvature Stress Method.....	80
Qualitative Analysis of Diffraction Patterns.....	82
Pole Figures.....	84
Stress vs. Coating Thickness.....	85
Analysis of Coating Stresses.....	86
Comparison of Results with other Studies.....	88
Review of Results.....	89
11 CONCLUSIONS.....	90
Fracture Measurements.....	90
Residual Stress Measurement.....	91

APPENDICES

A BALL-ON-RING LARGE DEFLECTION SOLUTION FOR STRESS.....	93
Theoretical Development.....	93
Verification of Results.....	97
Mathematica TM Computer Program for Calculation of Stresses.....	101
B DATA SET A.I.....	105
C DATA SET A.II.....	113
D DATA SET A.III.....	115

E DATA SET B.....	117
F RING-ON-RING DATA.....	118
REFERENCES.....	119

FRACTURE IN POLYCRYSTALLINE CVD DIAMOND

By

Lucien Hehn
and
J. J. Mecholsky, Jr.

ABSTRACT

Polycrystalline CVD diamond disks supplied by Texas Instruments Corp., Norton Co., and Raytheon Inc., were fractured in ball-on-ring loading. Fracture surface analysis was performed on the fractured specimens using both optical and scanning electron microscopy. Fracture surface analysis was used to locate and measure the size of the failure initiating critical flaws in over 60 specimens. The distribution of the a/b ratio which characterizes the shape of the critical flaws suggested that the cause of the strength reducing flaws was mechanical in origin, i.e., from the handling of the samples or from residual stresses. The main part of the fracture study was the Texas Instruments study in which twenty different "process" conditions were examined for strength and fracture toughness. A total of two hundred samples were fractured in this study (ten samples of each process condition). The fracture toughness and strength was obtained for 2-3 samples for each "process" condition. The specifics of the processing were not provided by Texas Instruments for proprietary reasons, however, the study offered an unprecedented opportunity to study fracture in CVD diamond with a large sample set. Through the examination of the matching halves of a representative fracture specimen fracture in the samples was demonstrated to be mostly transgranular. The combined data from the different sources showed that different processing conditions could lead to widely varying fracture toughness values. The strength was found to be an unreliable material property measure as it was found to vary strongly with thickness in the Texas Instruments study whereas the fracture toughness, K_{Ic} , varied in a random manner with sample thickness.

Residual stresses in diamond coatings deposited on (110) surfaces of single crystal Silicon by hot-filament CVD were measured. The residual stresses were

measured using both the $\sin^2\psi$ X-ray diffraction method and a curvature technique. The coatings were deposited on the (110) surfaces of Si bars of dimension 4 X 0.8 cm and thickness 2 mm. The diamond coating thicknesses varied from 2.5 to 15 μ m. In addition to residual stress, the (220) pole figures were measured for each sample and showed that no preferred orientation (texture) was present. Seven samples were evaluated using the X-ray diffraction method. The curvature method verified the results of the X-ray diffraction technique. Residual stresses in the coatings were found to be in tensile and in the range 65-355 MPa. This is opposite in sign and different in magnitude to that predicted by thermal expansion mismatch, indicating the presence of intrinsic stresses. The results of the X-ray diffraction technique showed the stresses to decrease in magnitude (less tensile) with increase in thickness over the range of thicknesses examined. The curvature of one of the samples was measured over the cooling temperature range from near the deposition temperature (850°C) to room temperature. The resulting stress (calculated from the curvature) vs. temperature curve followed that expected from thermal expansion mismatch but was shifted by a constant, temperature independent, value of about 520 ± 75 MPa. This demonstrated the presence of a temperature independent "intrinsic" stress of 520 ± 75 MPa.

CHAPTER I INTRODUCTION

Background

Polycrystalline diamond produced by chemical vapor deposition (CVD) has several properties which make it one of the most important materials today.^[1] These include high hardness, high electrical resistance, high thermal conductivity (five times that of copper at room temperature^[2]), high strength, low coefficient of friction^[3], chemical inertness, and optical transparency from the ultraviolet to the infrared.^[1] Potential applications are widespread. The high strength and hardness make it an excellent candidate for machine tool applications. The high electrical resistance and thermal conductivity suggest a number of applications in microelectronics. The optical properties make it an ideal material for improved infrared and high energy X-ray windows.^[1,4] Diamond's chemical inertness also allows for a number of potential applications, with the ability to withstand very aggressive environments, e.g., oxygen atmospheres up to 600°C.^[5]

As a material, diamond has a tremendous range of potential applications. The fact that it can be used as a hard, chemically resistant coating upon ceramics and metals in addition to the free-standing form makes it one of the most important new materials. Prior to the development of the CVD process, diamond could only be obtained in the form of natural gems and compacts, which limited their use to abrasives, cutting tools, and decorative jewelry.^[5] This technology (CVD of diamond) makes it possible to apply thin coatings of diamond to a variety of materials, allowing materials to be coated with a surface exhibiting several outstanding properties. Polycrystalline CVD diamond has been successfully coated

on Al₂O₃,^[6] silicon,^[7-8] and steel.^[9] In addition, free-standing diamond of thicknesses over 1mm are also being produced by several sources.

There remain two obstacles to the implementation of polycrystalline CVD diamond in applications: The cause of strength limiting flaws, and high residual stresses which occur during fabrication. It is with these two problems that this research program will be concerned.

One of the remaining questions in the study of mechanical behavior of CVD diamond is the cause of strength limiting cracks. The failure initiating cracks may be created as a result of residual stresses during processing while the coating is still adhered to the growth substrate. The intrinsic stresses have been shown to be tensile in several studies^[8,10] and thus may causing cracking at the growth temperature prior to cool-down and the establishment of thermal expansion mismatch stresses. Cracking of the coating could therefore occur even if the calculated thermal expansion mismatch stress was compressive.

The presence of large residual stresses in CVD diamond films has been identified as a major obstacle to the commercialization of these films.^[7] Residual stresses in these films can often be as large as the failure stress and can exceed the film/substrate adhesion strength causing cracking and delamination of the coating.^[7] These stresses are due, in part, to thermal expansion mismatch between the growth substrate and the diamond coating. In addition, substantial "intrinsic" or growth stresses may exist whose cause is the subject of debate.

Polycrystalline CVD diamond can be classified as a ceramic; brittle fracture is expected to be the primary mode of failure. To study fracture in this new material, a new approach was used in which samples were fractured in the ball-on-ring loading arrangement followed by examination of the fracture specimens using the techniques of fracture surface analysis.

To date, a comprehensive study of fracture in this material has not been made. From the results of other researchers in the literature,[1,3,11] the strength of this new material is well below it's potential. This study will be the first to characterize the fracture mechanism in this new material (the cause of the failure initiating flaws).

Polycrystalline/Single Crystal Toughness Ratio

A general "rule of thumb" for the strength and toughness of a polycrystalline ceramic based on the corresponding single crystal value is that the polycrystalline value is 2-4 times greater than the single crystal value. Single crystal fracture toughness values and their corresponding polycrystalline fracture toughness values are shown in Table 1.1 for several hard, brittle, ceramics. From Table 1.1. it can be seen that the polycrystalline/single crystal toughness ratio for polycrystalline ceramics is indeed about 2-4 times the single crystal value. Based on the single crystal value of strength and toughness, the strength and toughness of CVD diamond is below it's potential.

Outline of Study

The purpose of this study is to investigate strength limiting flaws and "intrinsic" residual stresses. The methods developed in this study will be equally applicable to other CVD ceramic systems, i.e., SiC, Si₃N₄, ZrO₂, Al₂O₃, and others. There are two major obstacles to the implementation of CVD diamond: the existance of strength limiting flaws, and the presence of large residual "intrinsic" stresses which occur in both coatings and free-standing bodies.

The first part of this study is on the fracture properties; fracture toughness (K_{Ic}), strength, and fracture surface analysis of a series of CVD diamond samples supplied by Texas Instruments. The second part of this study is to relate the results pertaining to the

Table 1.1 Fracture Toughness Values of Several Polycrystalline Ceramics with Corresponding Single Crystal Values

Material	Single Crystal K_{Ic} (MPa \sqrt{m})	Polycrystal K_{Ic} (MPa \sqrt{m})
Al_2O_3	2.6 ^[12]	3-5 ^[13]
ZrO_2 (Y_2O_3)	1.3 ± 0.2 ^[12]	2.6 ^[12]
SiC	2 ± 1 ^[12]	3-4 ^[12]
Si_3N_4	NA	4-5 ^[14]
TiO_2	0.8 ± 0.2 ^[12]	3-6 ^[12]
ZnSe	0.2 ^[15]	0.9 ^[15]
Diamond	3.4 ^[2]	1-8 (Present study)

Texas Instruments to results obtained on samples obtained from a number of other manufacturers and then to look for overall general characteristics which are specific to CVD diamond. The third part of this study is on the measurement of residual stresses which evolve during the growth of CVD diamond as the residual stresses may play an important role in the fracture properties.

CHAPTER 2 MECHANICS

Fracture Mechanics

Starting with Irwin's^[16] expression for the stress intensity, K, around the periphery of a semielliptical (half ellipse) surface crack:

$$K = \sqrt{1.2\pi} \sigma \sqrt{\frac{a}{Q}} \left(\frac{a^2}{b^2} \cos^2 \theta + \sin^2 \theta \right)^{1/4} \quad (2.1)$$

where σ is the far-field stress, the factor 1.2 the so-called front face correction factor^[17] to account for the increase in K for a surface crack in relation to a through, elliptical center crack. a in the factor $\sqrt{a/Q}$ is the smaller of the semiminor and semimajor axes of the semiellipse (see Fig. 2.1). The expression raised to the one-fourth power gives the variation of the stress intensity around the periphery of the ellipse. a and b in this expression are defined as in Fig. 2.1a. $Q = \phi^2$, where ϕ is an elliptic integral given by

$$\phi = \int_0^{\pi/2} \sqrt{\left(1 - \frac{b^2 - a^2}{b^2}\right) \sin^2 \theta} d\theta \quad (2.2)$$

Randall^[17] demonstrated that "normal" cracks or cracks observed in practice can be treated as being semielliptical even though they may deviate significantly from the ideal semielliptical shape.

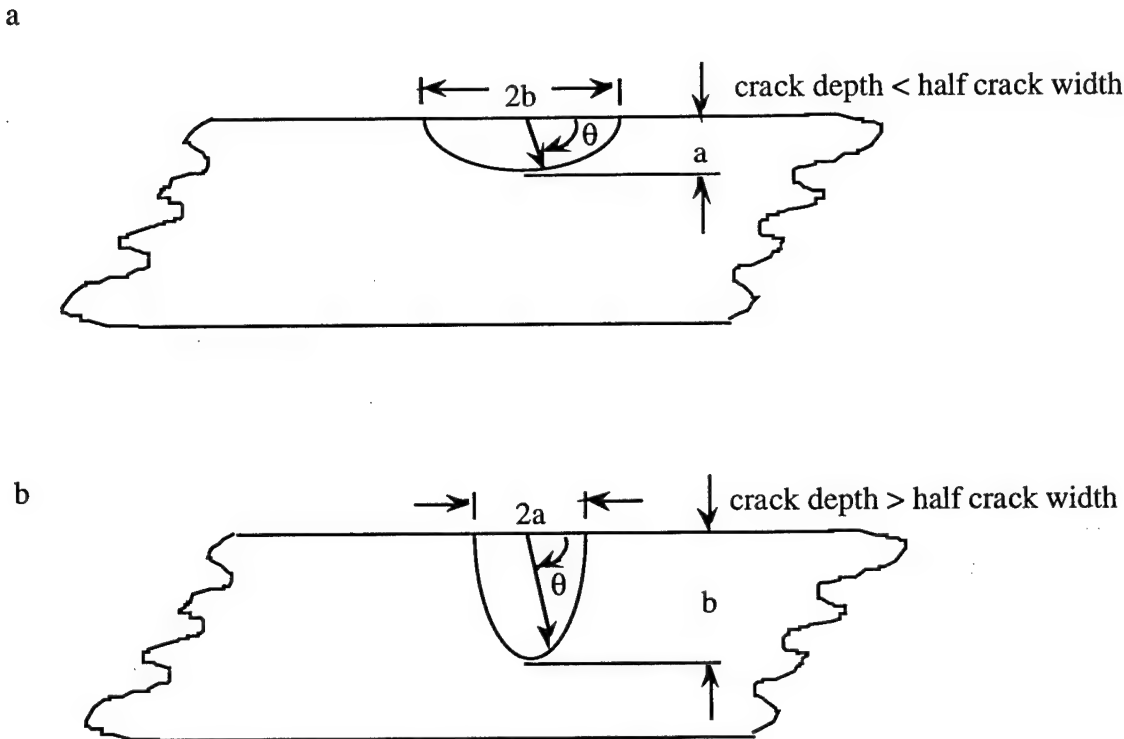


Fig. 2.1. Definition of the terms a and b of the semielliptical surface crack. The smaller of the semimajor and semiminor axes is defined as a in the factor $\sqrt{a/Q}$ of eqn. 2.1.

Following Randall, Bansal^[18] showed that the area of the semiellipse, $A = \pi ab/2$, could be used as a measure of stress intensity through the approximation

$$K_{Ic} \approx \frac{Y\sigma_f A^{1/4}}{1.68} \quad (2.3)$$

for a/b ratios (a and b defined as in Fig. 2.1a.) between 0.2 and 3. The approximation has a maximum error of less than 5%. Therefore, for cracks not of extreme shape, i.e., very deep and short or shallow and very wide, use of eqn. 2.3 yields accurate results. Using $Y = \sqrt{2/\pi}$ from eqn. 2.1, gives

$$K_{Ic} \approx \sigma_f \frac{\sqrt{1.2\pi}}{1.68} \sqrt{c} \quad (2.4)$$

where $c = \sqrt{ab}$ (a and b defined as in Fig. 2.1a.). From Randall,^[17] eqn. 2.4 is also accurate for "normal" cracks which may deviate significantly from the ideal semielliptical shape. Equation 2.4 was used to calculate the fracture toughness values used in this study.

A critical assumption in the use of eqns 2.1-2.4 is that the crack is atomically sharp. Failure from a blunt crack will give a K_{Ic} value much higher than that from a sharp crack.

Loading of Samples

In ball-on-ring loading (see Fig. 2.2), the disk is placed over a ring and the load is applied at the center of the disk through a ball. The solution for the radial (σ_r) and tangential (σ_θ) stresses on the tensile surface of a simply supported circular plate loaded over an area of small circular radius r_o , given by Roark and Young,^[19] is

$$\sigma_r = \sigma_\theta = \frac{3P}{2\pi t^2} \left[(1+v) \ln \frac{a}{r_o} + 1 \right] \quad \text{at } r = 0 \quad (2.5)$$

$$\sigma_\theta = \frac{3P}{8\pi t^2} \left[4(1+v) \ln \frac{a}{r} + (1-v) \left(4 - \frac{r_o^2}{r^2} \right) \right] \quad \text{if } r > 0 \quad (2.6)$$

$$\sigma_r = \frac{3P}{8\pi t^2} \left[4(1+v) \ln \frac{a}{r} + (1-v) \frac{(a^2-r^2)}{a^2} \frac{r_o^2}{r^2} \right] \quad \text{if } r > 0 \quad (2.7)$$

The samples were loaded to fracture in ball-on-ring loading. However, the principal stress components, σ_r and σ_θ given should be modified by the factor a^2/R^2 as suggested by Vitman and Pukh^[20] to account for the constraining effect of the annular overhang portion of the disk.^[20-22] The stress components are then given by

$$\sigma_r = \sigma_\theta = \sigma_{max} = \frac{3P(1+v)}{4\pi t^2} \left[1 + 2 \ln \frac{a}{b} + \frac{(1-v)}{(1+v)} \left(1 - \frac{r_o^2}{2a^2} \right) \frac{a^2}{R^2} \right] \quad \text{if } r < r_o \quad (2.8)$$

$$\sigma_r = \frac{3P(1+v)}{4\pi t^2} \left[2\ln \frac{a}{r} + \frac{(1-v)}{2(1+v)} \left(\frac{a^2 - r^2}{a^2} \right) \frac{r_0^2}{r^2} \frac{a^2}{R^2} \right] \quad \text{if } r > r_0 \quad (2.9)$$

$$\sigma_\theta = \frac{3P(1+v)}{4\pi t^2} \left[2\ln \frac{a}{r} + \frac{(1-v)}{2(1+v)} \left(4 - \frac{r_0^2}{r^2} \right) \frac{r_0^2}{r^2} \frac{a^2}{R^2} \right] \quad \text{if } r > r_0 \quad (2.10)$$

$$r'_0 = \sqrt{1.6r_0^2 + t^2} - 0.675t \quad \text{for } r_0 < 0.5t, \quad r'_0 = r_0 \quad \text{if } r_0 > 0.5t \quad (2.11)$$

where P is the load, a the radius of the ring, t the thickness of the disk, and r the radial distance from the center of the disk r'_0 an equivalent radius of loading for concentrated loading.[19] For concentrated loading as in ball-on-ring loading an equivalent radius r'_0 can be used in eqns. (2.8-2.11), where r_0 is the effective contact radius between the ball and the disk.[19, 21] Shetty et al.[21] showed via strain gage measurements that, choosing a value of $r'_0 = .33t$ ($r_0 = 0.1t$) for ball-on-ring loading gave good agreement between the measured stresses and those predicted by eqns. 2.8-2.11.[21] Equations (2.8-2.10) are valid for maximum deflections less than half the thickness of the disk.[19-22] Under this type of loading, the stress decreases rapidly as the position changes radially away from the center of the disk (see Fig. 2.3).

After fracture of the disks, observation of the fracture surface was made by optical and scanning electron microscopy to locate fracture surface features and hence locate and measure the critical flaw. The radial position of the failure origin r was measured to obtain σ_f (failure strength) from eqns. 2.8-2.11.

The critical fracture toughness, K_{Ic} , was then be calculated from eqn. 2.4. If the crack is created by Vickers indentation, eqn. 2.4 must be modified to account for the contact residual stresses caused by the indentation process, the toughness is obtained from the linear best fit calibration function,[23]

$$K_{Ic} = K_0 + A\sigma_f \sqrt{c_m} \quad (2.12)$$

where $A = 2.02$, $K_0 = -0.68 \text{ MPa}\sqrt{\text{m}}$, and c_m the half diameter of the trace of a "surviving" indentation crack on the tensile surface of the sample. The crack size in this method is obtained by placing three indentations on the sample surface measuring c_m after fracture from one of the surviving indentation cracks on the sample surface. Chan^[24] demonstrated that the crack size, c , measured from the fracture surface, ($c = \sqrt{ab}$) could be used in eqn. 2.12 leading to the expression,

$$K_{Ic} = \sigma_f 1.65 \sqrt{c}, \text{ where } c = \sqrt{ab} \quad (2.13)$$

where the $c = \sqrt{ab}$ is the crack size measured from the fracture surface.

Under this type of loading, the stress decreases rapidly as the position changes radially away from the center of the disk (Fig. 2.3-2.4). Since the radial and tensile stress component values decrease rapidly as the location moves away from the center of the disk, the measurement of the radial position, r , is one of the leading sources of error in calculating the stresses.

Shetty et al.^[25] demonstrated that the direction of propagation of an advancing crack is perpendicular to the direction of the maximum principal tensile stress. The crack driving stress must be the maximum principal tensile component on the disk surface and is therefore given by the tangential (σ_θ) component since it is always the largest principal stress component (Fig. 2.3-2.4). Inspection of the crack patterns of the fractured disks showed that the cracks always propagated radially outward from the center of the disk

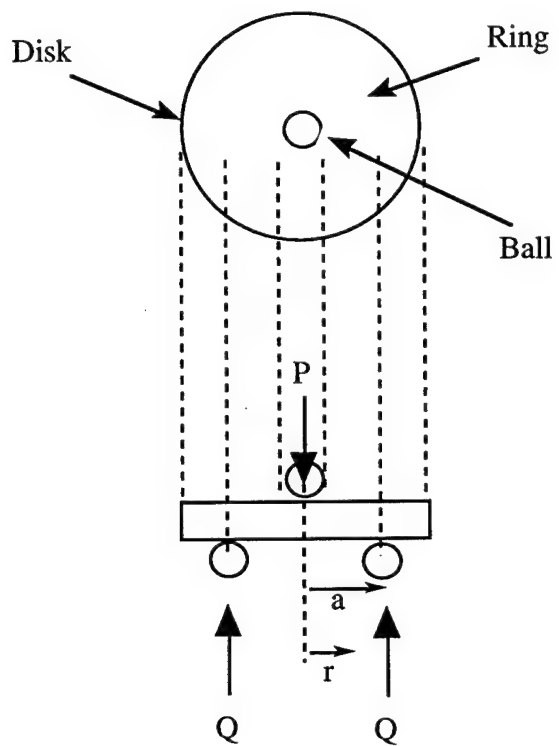


Fig. 2.2 Free-body diagram of ball-on-ring loading. P is the applied load, Q the intensity of loading, a the ring radius, and r the radial coordinate.

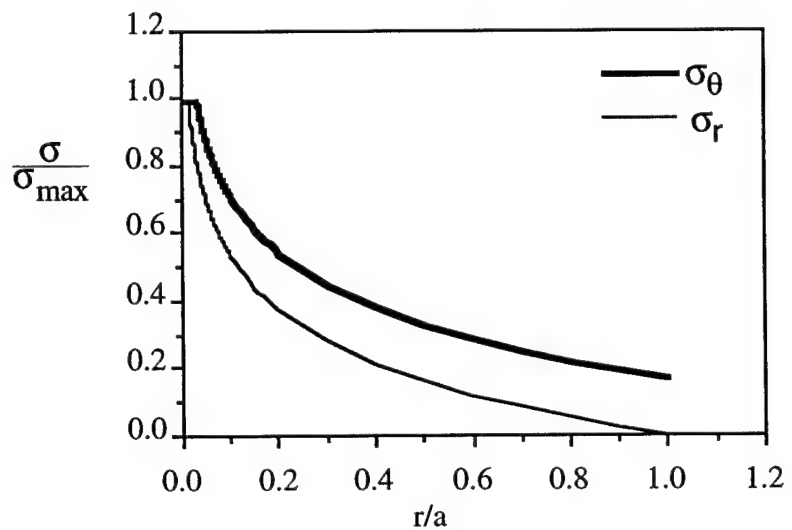


Fig. 2.3 Plot of reduced radial (σ_r) and tangential (σ_θ) stress components vs. r/a using the formulas given by Roark [19] (eqns. 2.5 - 2.7) with $a/t = 10$, and $v = 0.07^{[2]}$ (polycrystalline diamond).

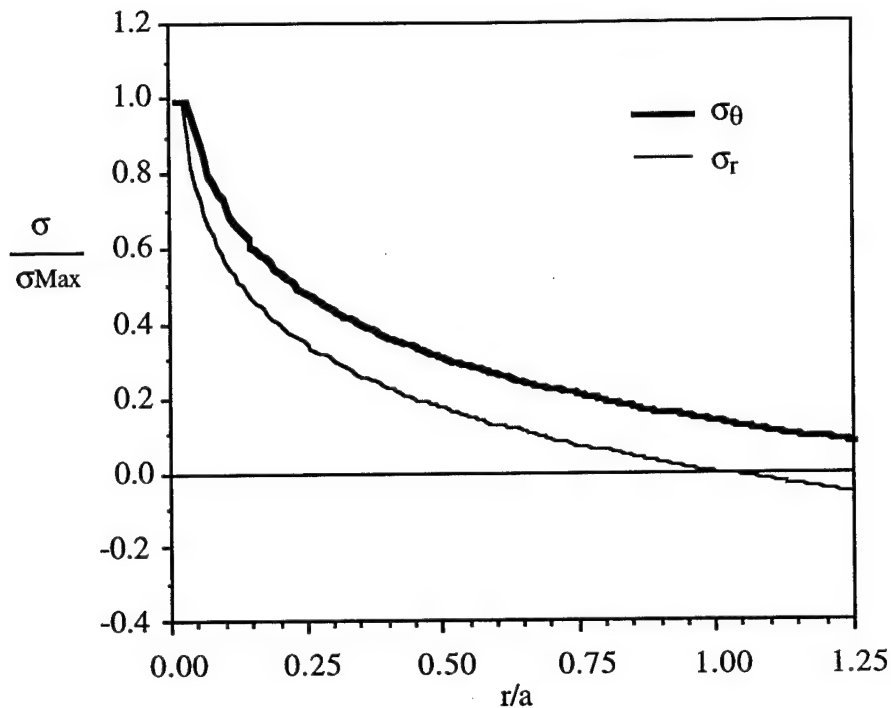


Fig. 2.4 Plot of reduced radial (σ_r) and tangential (σ_θ) stress components vs. r/a using eqns. 2.8 - 2.11 with $a/t = 10$, and $v = 0.07^{[2]}$ (polycrystalline diamond).

thus verifying the choice of the σ_θ component in the calculation of strength and fracture toughness.

Ring-on-ring loading was also considered because of the advantage of constant stress within the inner ring, thus eliminating the need to measure the radial position, r , of the failure origin to calculate the stress. Ring-on-ring has the disadvantage of significant stress concentrations occurring along the inner loading ring that are not predicted by plate theory, and the occurrence of friction and wedging effects.^[26] In addition, the alignment of the test fixtures is critical. These effects must be carefully analyzed in order to use this type of testing.^[26] Ball-on-ring has the advantage of simplicity, easier alignment, and accuracy.^[26]

CHAPTER 3 FRACTURE SURFACE ANALYSIS

The Characteristic Features of Brittle Fracture

The characteristic features of the fracture surface of a brittle fracture are shown schematically in Fig. 3.1.[27] The critical flaw is surrounded by the so-called mirror region. As the crack continues to propagate through the mirror region it makes a transition to the hackle region and then branches to form two crack fronts. The boundary between each of these regions (mirror, mist, hackle, and macroscopic branching) is distinct in that the transition from one region to the next is discreet. The various distances, r_j , shown in Fig. 3.1 are the distances along the surface from the failure origin to the particular boundary (mirror, mist, hackle, and macroscopic branching).

It has been shown experimentally that the r_j distances are related to the stress at the surface, σ , by the relation^[27-29]

$$\sigma r_j^{1/2} = A_j \quad (3.1)$$

where $r_j = r_1, r_2, \text{ and } r_{cb}$ and A_j is a separate constant for each mirror boundary. Through the use of eqn. (3.1) and a subsequent modification to include the effect of the free surface on the shape of the mirror boundary away from the surface, measurement of the various boundary shapes can be used to quantify the residual stress level on the fracture surface. In addition, the shape of the mirror boundary could be used to identify variation in Young's modulus about the mirror periphery.^[27,30] The fracture surfaces of polycrystalline CVD diamond have a complex microstructure and the various mirror

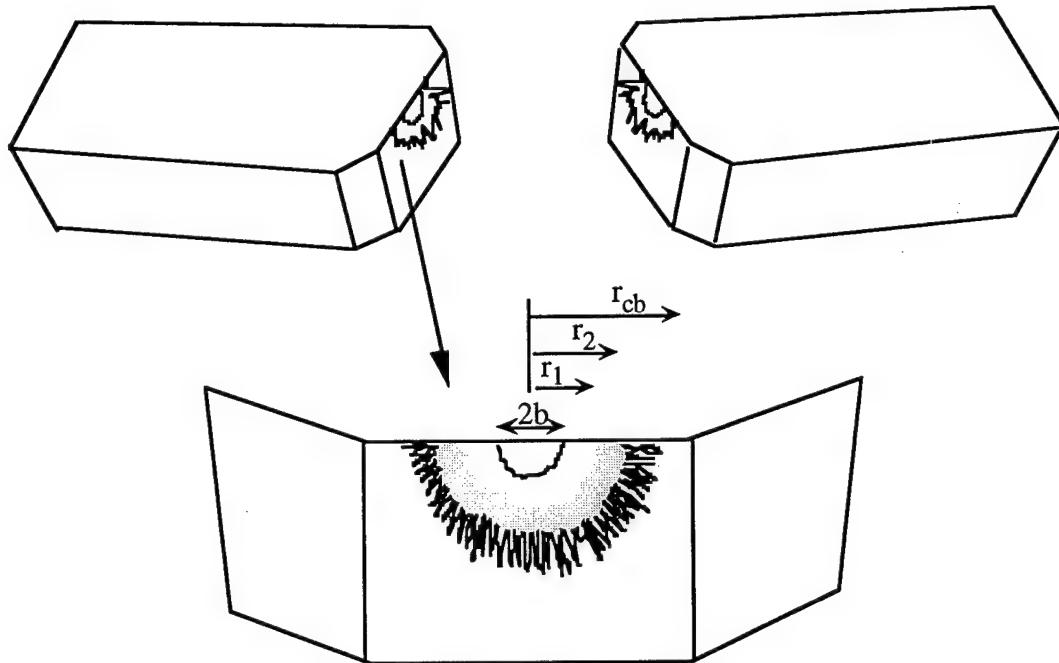


Fig. 3.1 Schematic of the characteristic features of brittle fracture surrounding the failure origin on the fracture surface. The initial critical crack width is represented by $2b$. r_1 , r_2 , and r_{cb} are the mirror/mist, mist/hackle, and macroscopic crack branching boundaries.

boundaries, in general, can not be identified. However, in one sample all three of the mirror boundaries were discernible and are identified in the schematic in Fig 3.2.

Analysis of Macroscopic Crack Branching Patterns

A synopsis of the macroscopic crack branching patterns observed is shown in Fig. 3.3. All of the samples broke in a small number of pieces, i.e., less than six. Prior to scanning the fracture surfaces for river marks, the fragment containing the fracture origin can usually be found by analysis of the pattern. As the crack propagates it bifurcates (branches), thus revealing the path and likely fracture origin.^[25]

The number of pieces is expected to increase with fracture energy and fracture energy with strength. The strength is seen to increase with number of fracture pieces as is demonstrated for a particular group of specimens in Fig. 3.4. The specimens shown in Fig. 3.4 were not part of the Texas Instruments study and were shown here because they are the largest data set of strength data in which all of the samples were fabricated from similar process conditions. The samples all broke in a small number of pieces, i.e., 2, 3, 4, and 5. In addition, it was not always possible to exactly distinguish which of the forms the pattern belonged to amongst those of Fig. 3.3.

Locating the Origin of Failure

The fracture process in general produced only two to six fragments. Before testing, cellophane tape was placed on the compressive surface of the disks to keep the fragments together after the fracture event. The tape was cut with an "X" pattern to ensure that the tape would have no effect on the stress distribution of the tensile surface. The center of the "X" was cut away so that the ball made contact with the disk only.

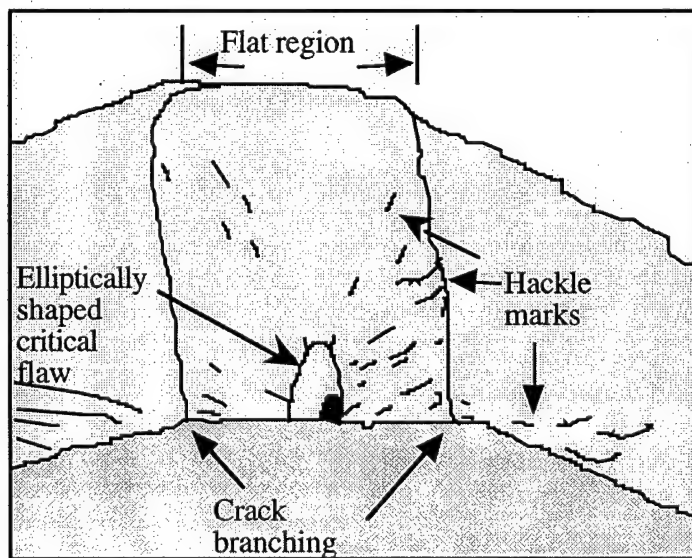
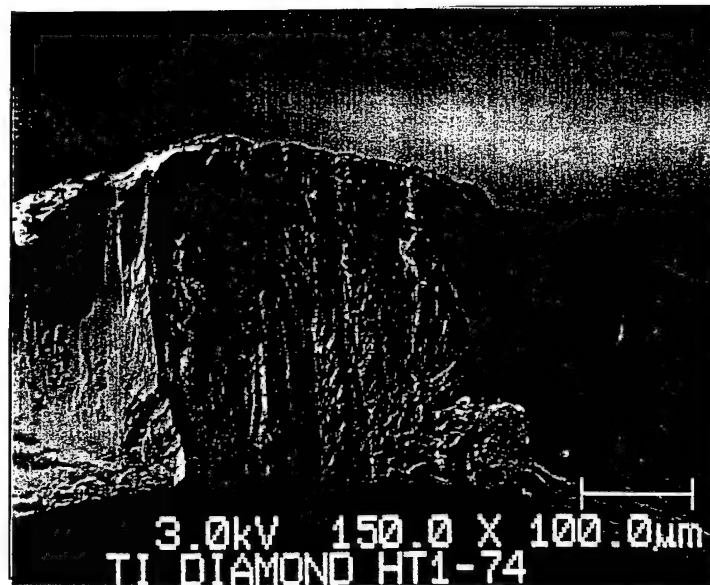


Fig. 3.2 In a, a scanning electron micrograph of fracture surface of polycrystalline CVD diamond sample in which all the fracture mirror boundaries could be identified. In b, a diagram showing the fracture features. Hackle marks indicate direction of propagation away from origin of failure.

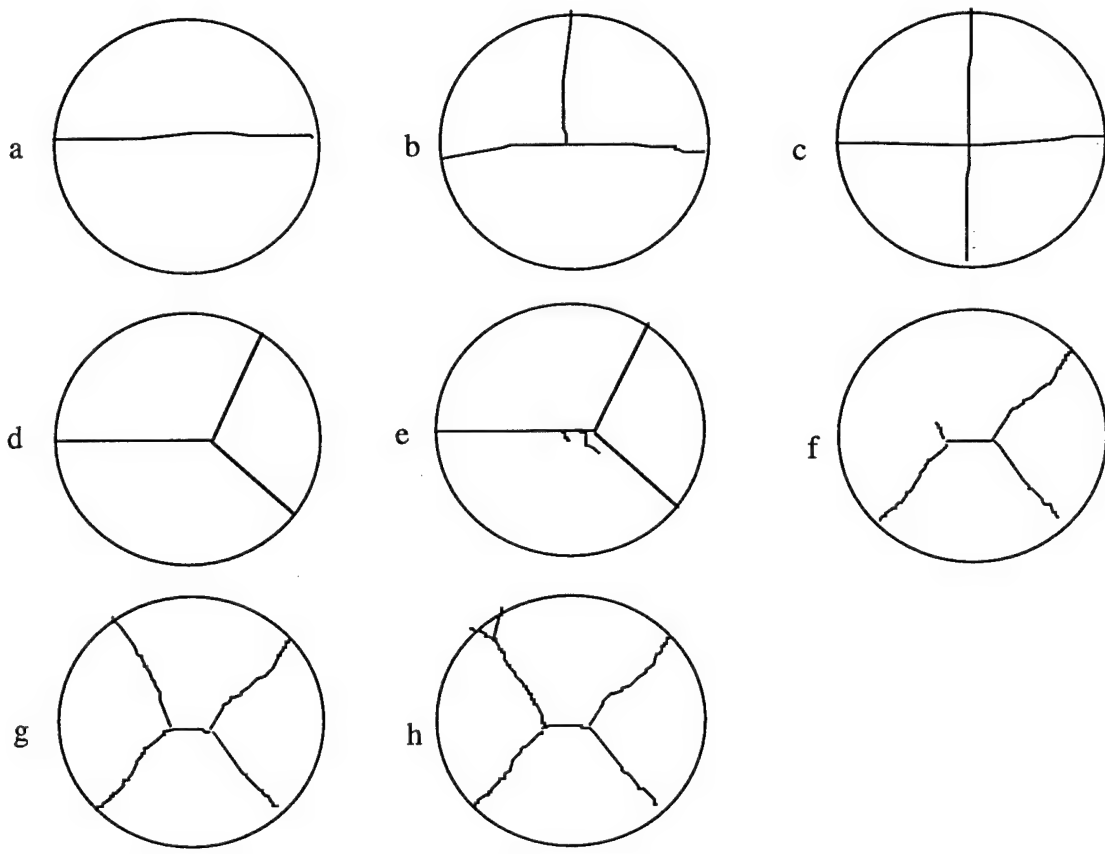


Fig. 3.3 A synopsis of the macroscopic crack branching patterns observed. In a-c, the specimen is broken into two pieces with a secondary crushing crack occurring later and breaking the disk into three pieces (b), and four pieces (c). In d-e, the disk is broken into three pieces with fracture occurring near the center of the disk with failure to branch on the left side. In e, small attempted branching points are visible. In f-g, the disk is broken into four pieces, but in f, one branch point is incomplete. In h, the specimen is broken into five pieces.

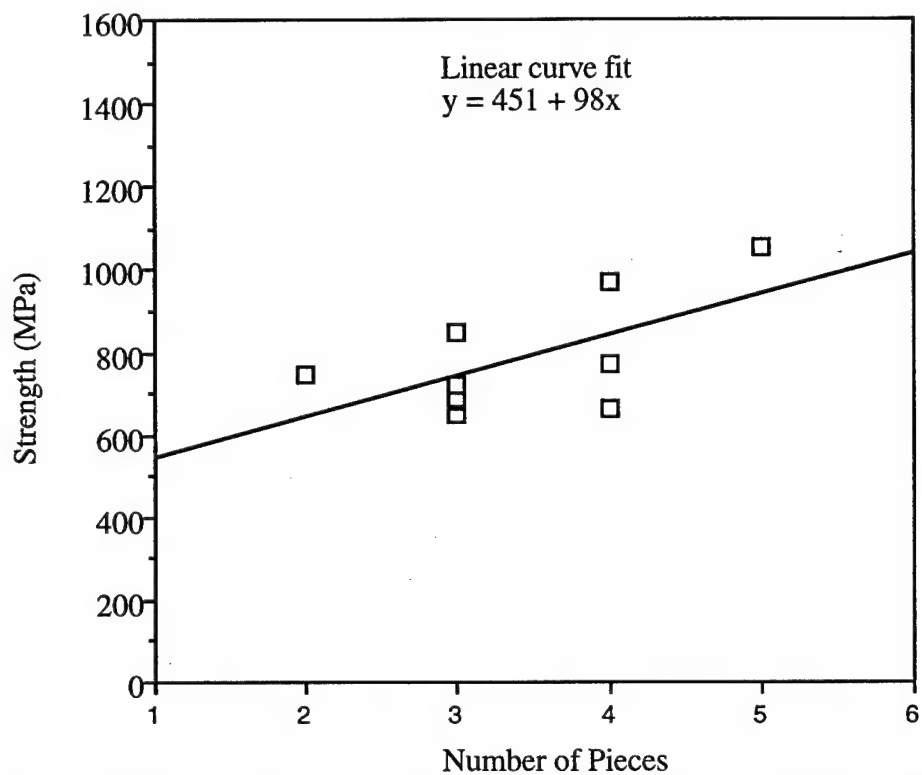


Fig. 3.4. Plot of strength vs. number of fracture pieces for a group of similarly processed samples.

On most specimens, the fracture surface contained at least a few small flat areas containing distinct river patterns. These flat areas were due to the advancing crack cleaving a grain (transgranular fracture). The river patterns appeared as very fine markings resembling a flowing river. The "flow" of the river pattern is in the direction of advancement of the crack. We used these patterns as a guide in finding the origin of failure. The river patterns seemed to be the most reliable markings to identify the direction of propagation of the crack. Note that the direction of flow of the river marks is opposite to the river marks described by Hertzberg.^[28] The reason for this is that the branching of the marks (which determines the direction of flow) is caused by a different mechanism in metals as described by Hertzberg. However, the mechanism for the formation of these markings in both metals and in ceramics is very similar.

A typical procedure for locating the origin of failure was the following:

- I.) The fracture event produces several fragments two of which contain the failure origin (one being the mirror image of the other). Selection of a fragment containing the failure origin can often be made without having to examine all fragments. The failure origin will always exist on a flat region and is bounded on either side by branching of the crack (Fig. 3.2).
- II.) While viewing a specimen under the optical microscope or SEM, locate a river pattern and scan towards the direction indicated by the river marks which lead back to the origin.
- III.) Continue scanning towards the origin (the direction as indicated by the river marks) until more river marks are found which "flow" in the opposite direction. Now we know we have passed the origin and have set an "upper bound" as to its location. We continue to scan in the opposite direction until again the river marks have changed direction and hence

further narrowing the bounds around the origin. Eventually the region containing the origin of failure can be found and this region can be examined for any features resembling the elliptically shaped flaw.

If, when scanning the fracture surface, the river marks continue to "flow" off the end of the fragment, then the fragment does not contain the failure origin and another fragment should be examined.

The biggest difficulty in locating the origin of failure (and subsequently measuring the flaw size) is the lack of recognizable fracture surface markings in some specimens and the disruption of fracture features by the large grains. In a few cases the formation of the elliptically shaped critical flaw was disrupted by one or more grain boundaries; in these cases, an estimate of the crack shape and size by continuation of the existing crack was made.

One of the other difficulties in "reading" the fracture surface markings is the separation of markings due to the fracture process (cleavage marks, hackle, and river patterns) from those due to the grain structure. The CVD diamond microstructure contains typically large elongated crystallites. The crystallites grow upwards from the bottom of the disk to the top.

As an example of the procedure given above for finding and measuring the critical flaw is shown through the series of SEM images in Fig. 3.5 and Fig 3.6. In Fig. 3.5, an enlargement of the area around the critical flaw of a typical sample is shown. The critical flaw is outlined with a white dashed line. In this view, the tensile surface is the top surface which is also the substrate surface. In Fig 3.6 are shown two split screen SEM images (the area in the white box on the right side of the image is shown at 10X in the left image) just to right (top) and just to the left (bottom) of the critical flaw shown in Fig. 3.5. Some of the features between Fig.'s 3.5 and 3.6 overlap, and the river marks can be seen to flow away from the failure origin.

An SEM image enlarging the area surrounding the critical flaw is shown in Fig. 3.2 and in Fig. 3.7. The top image in Fig. 3.7 is an enlargement of the flat region with a white dashed line outlining the shape of the critical flaw. A nearly perfect semicircular critical flaw is shown in at the top of Fig. 3.8. At the bottom of Fig. 3.8 is an enlargement of the flaw.

Determination of Strength and Toughness

After fracturing the specimens, the failure origin was located and it's radial position, r , measured. As described in the previous chapter, the strength (σ_f) is defined as the tangential stress at the radial position r , measured from the center of contact of the ball to the failure origin at fracture. The failure load, radial position of the failure origin, r , and disk thickness, t , were used in eqn. 2.10 to obtain σ_f . If the failure origin was found within a radial position of $r < 0.33t$, eqn. 2.08 was used to obtain σ_f since failure occurred with the equivalent radius of contact, r'_0 , defined as $0.33t$ in the previous chapter. t was measured at the location of the failure origin since t typically varied by up to 15% throughout a disk. The toughness was calculated from eqn. 2.4 using the strength (σ_f) and width $2b$, and depth a , of the critical flaw measured from the fracture surface.

Indentation Toughness Measurements

In order to verify the fracture surface analysis measurements and the loading procedure, the fracture toughness was also measured on several specimens using an indentation method. The fracture toughness was obtained from the trace of the indentation cracks emanating from the corners of a Vickers indentation and the "crack-indentation" equation^[31]:

$$K_c = \frac{R}{4} \left(\frac{E}{H} \right)^{1/2} \left(\frac{P}{c_0^3} \right)^{1/2} \quad (3.2)$$

where E/H is the ratio of Young's modulus to the hardness, P the indentation load, c_0 the trace of the indentation crack, and $\$V^R$ is a material independent parameter equal to 0.016.^[31]

The hardness was calculated from the equation:

$$H = \frac{P}{2a^2} \quad (3.3)$$

where $2a$ = indent diagonal, P = indent load. A load of 500 grams was used in all indent measurements. The results of the Vickers indentation measurements are shown in Table 3.1 along with the corresponding fracture toughness, K_{Ic} , values obtained from fracture surface analysis.

Table 3.1 Indentation and FSA Fracture Toughness Data.

Sample number	Average 1/2 diagonal, a (μm)	Hardness (GPa)	Average radial crack length (μm)	Indentation toughness ($\text{MPa}\sqrt{\text{m}}$)	FSA toughness ($\text{MPa}\sqrt{\text{m}}$)
1	9.8	26	34	7	6
2	3.7	180	20	6	8
3	4.3	140	14	12	6
4	3.8	170	21	6	9
5	4.1	150	17	8	N/A
6	N/A	N/A	N/A	N/A	9
7	N/A	N/A	N/A	N/A	9
8	N/A	N/A	N/A	N/A	8
			Average	8	8

The one to one match up of FSA results with indentation results (Table 3.1) for each sample in which both measurements were made was fair for three of the samples but rather poor for sample 3 (compare 12 $\text{MPa}\sqrt{\text{m}}$ for indentation with 6 $\text{MPa}\sqrt{\text{m}}$ for FSA). The fracture toughnesses obtained from the indentation method varied considerably,



Fig. 3.5 An enlargement of the area around the critical flaw of a typical sample is shown. The critical flaw is outlined with a white dashed line. In this view, the tensile surface is the top surface which is also the substrate surface



Fig 3.6 Two split screen SEM images (the area in the white box on the right side of the image is shown at 10X in the left image) just to the right (top) and just to the left (bottom) of the critical flaw shown in Fig. 3.5.

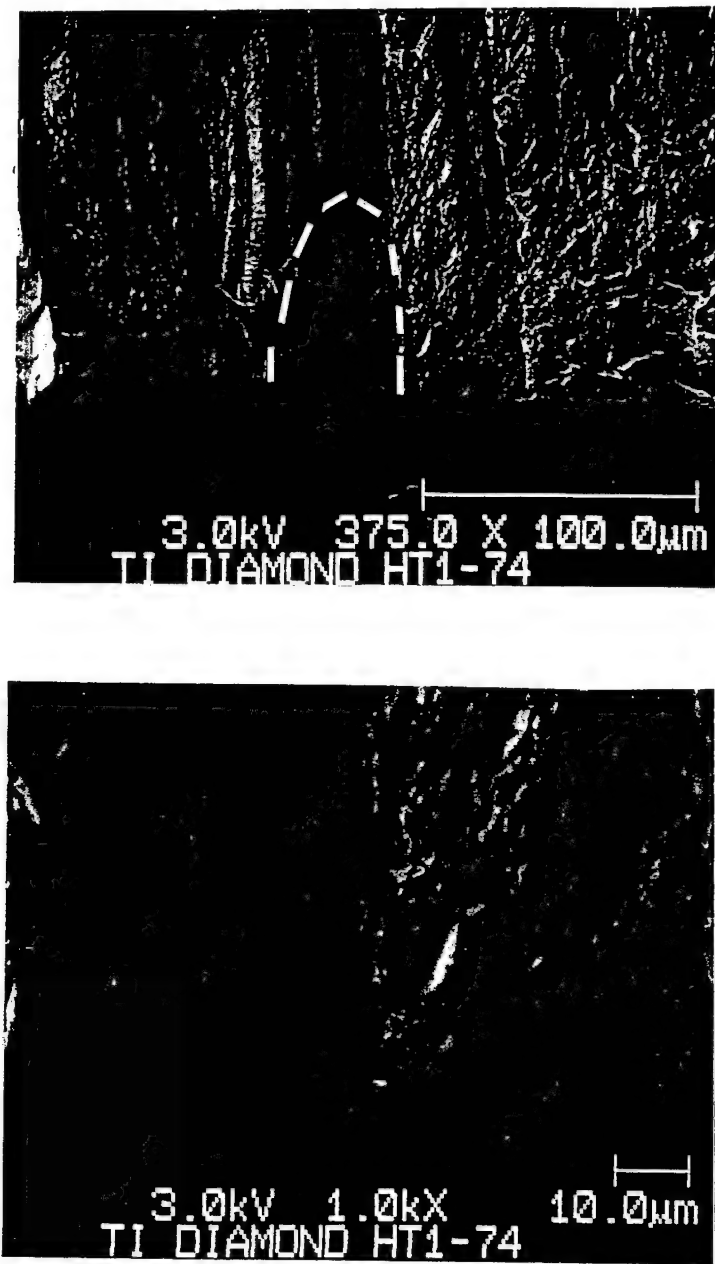


Fig. 3.7 An SEM image enlarging the area surrounding the critical flaw shown in Fig. 3.2. (top) an enlargement of the flat region with a white dashed line outlining the shape of the critical flaw. (bottom) an enlargement of the area shown in the top image.



Fig 3.8 (top) A nearly perfect semicircular critical flaw is shown. At the bottom is an enlargement of the flaw

although when averaged they matched the average value obtained from the fracture surface analysis reasonably well (compare $8 \text{ MPa}^{\sqrt{m}}$ for FSA to $8 \text{ MPa}^{\sqrt{m}}$ for indentation). The lack of one to one correspondence between the indentation results and FSA results may be due to the following: in order to obtain maximum accuracy using the indentation technique, several measurements must be made on a sample and then averaged because of the variation which occurs between repeated measurements. This repetition was not done in order to minimize costly indentor damage.

Cleavage Marks

Cleavage marks on the fracture surface can be identified as several parallel lines or edges in a row (see Fig. 3.5 and Fig. 3.6). The cleavage marks are caused by the propagating fracture surface penetrating through a grain and in addition entering a small distance perpendicular to the direction of propagation of the crack front. The perpendicular propagation is cleavage along crystallographic directions of "easy" fracture or lowest fracture energy of the crystal (grain), forming a series of edges appearing like successive steps of a staircase.

River Marks

River marks on the fracture surface appear as very fine lines flowing like a river. When the propagating fracture surface cleaves a grain the surface appears very smooth when viewed optically and the fine river marks are occasionally left on the cleaved surface. The fine marks on the cleaved surface fan out in the direction of propagation of the crack front.

Examination of Matching Halves of Fracture Surface

From the description of the cleavage and river markings, it is clear that where these markings exist, the fracture surface is transgranular. All of CVD diamond fracture surfaces observed in this study consisted mostly of regions containing river markings and cleavage marks. This indicates that fracture in CVD diamond is mostly transgranular.

Another method of analysing the fracture surface is through observation of the matching halves. When the sample is fractured the matching halves would appear as identical, mirror images if the fracture were fully transgranular. However, some small fragments of the fracture surface may fly off during the fracture event. SEM micrographs of the matching halves of one fracture surface are shown in Fig. 3.10. The schematic in Fig 3.9 describes how the two photos are to be superimposed upon one another for comparison purposes. In comparing the two photos the consideration must be taken that the photos are of different samples and at best, are mounted in the SEM at slightly different tilt orientations. SEM images are strongly dependent on tilt orientation in terms of brightness and contrast to the different regions of the sample and tilt dependent distortions of the image.

Visually superimposing the matching halves in Fig. 3.10 it is clear that the majority of the fracture surface features between the two photos are identical, i.e., they are nearly mirror images of one another.

From the matching halves of Fig. 3.10, the area within the failure origin and about its perimeter is not only riddled with cleavage and river marks, but is nearly identical in appearance between the two photos. This clearly indicates the failure is mostly transgranular.

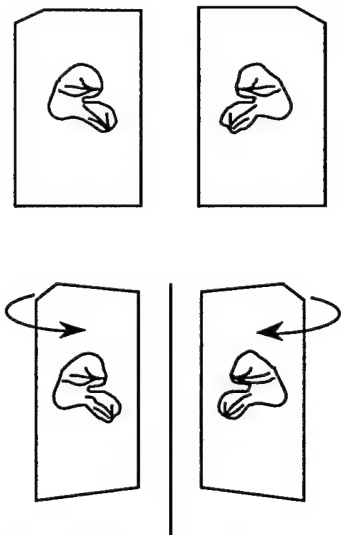


Fig. 3.9 Examination of matching halves of fracture surface. Diagram explaining the superposition of the two photos in Fig 3.10.

Growth Surface Cracks

In all of the over eighty samples investigated in which failure origins were located, failure was found to have initiated from surface cracks. Figure 3.11 shows an SEM photograph of the growth surface of a typical sample investigated in this study. The growth surface shown in Fig. 3.11 reveals a network of grain boundary cracks. However, the overall fracture surface was previously shown to be mostly transgrannular fracture. From Fig. 3.11 it is clear that fracture likely initiates from grain boundary or intergrannular cracks. After initiation, fracture proceeds transgrannularly. The cause of this is most likely grain to grain residual stresses or microresidual stresses within the grains.

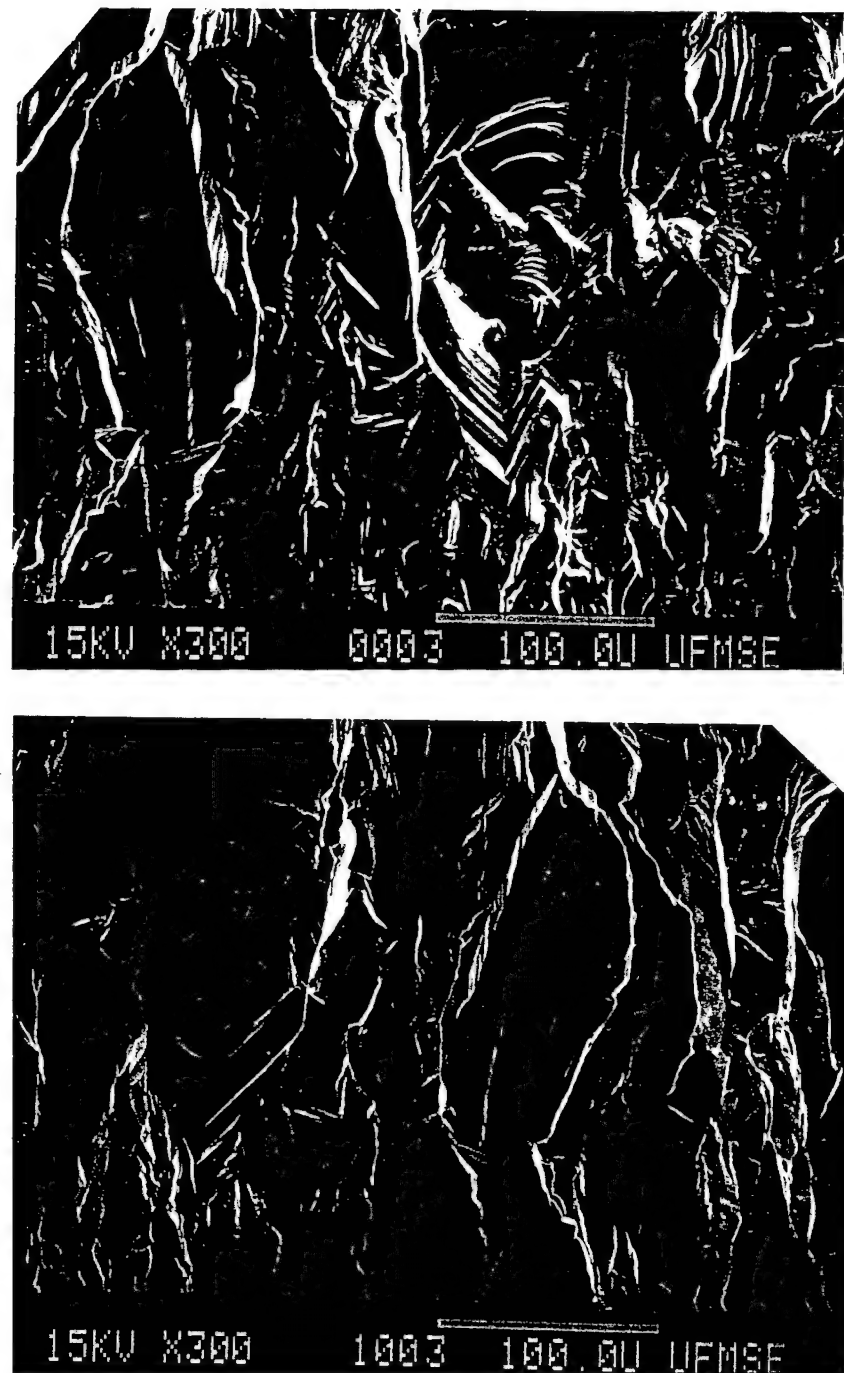


Fig. 3.10 SEM micrographs of the matching halves of one fracture surface around the failure origin. The schematic in Figs. 3.9 describes how the two photos are to be superimposed upon one another for comparison purposes.



Fig. 3.11 An SEM image of the growth surface of a typical sample investigated in this study.

CHAPTER 4 RESULTS OF OTHER STUDIES

Fracture Toughness (K_{Ic}) of Polycrystalline CVD Diamond

Only a limited number of studies on fracture properties of CVD diamond exist at present. Fracture toughness values, K_{Ic} , of single crystal diamond, polycrystalline diamond compacts (composites), and CVD diamond obtained in other studies are shown in Table 4.1. The K_{Ic} values obtained in this study (the Texas Instruments study plus other sources) varied considerably between the different sample sources (1-9 MPa \sqrt{m}). With the exception of one sample set obtained from one source (outside the Texas Instruments study), the variation in K_{Ic} values within each source was much narrower.

Drory et al.[11,32] used the Vickers indentation technique and a disk-shaped compact-tension test method to determine K_{Ic} . The two methods were used on samples from the same source using the same processing technique and the values obtained from the two methods matched well (Table 4.1). Single crystal K_{Ic} values were obtained by Field[2] and Novikov and Dub[33] using indentation and the values corresponded closely (Table 4.1). In addition, K_{Ic} values were obtained by Field for diamond composites, 7.3 and 8.6 MPa \sqrt{m} . The K_{Ic} values for the diamond composites are about twice that of the single crystal values.

Table 4.1 Fracture Toughness (K_{Ic}) Values of Diamond from Different Studies

Study	K_{Ic} (MPa \sqrt{m})	Testing Method	Comment
Field[2]	7.3	not available	10 μm grain composite
	8.6	not available	25 μm grain composite
	3.4		single crystal
This study	1-8	fracture surface analysis (FSA)	samples obtained from several sources
This study	8	indentation	samples obtained from one source
Drory et al.[32]	5.3 ± 1.3	indentation	
Drory et al.[11]	5.6 ± 0.4	indentation	
Novikov and Dub[33]	4	indentation	Single crystal
Drory et al.[11]	6.3	disk-shaped compact-tension	

Strength of Polycrystalline CVD Diamond

Cardinale and Robinson^[1] and Valentine et al.^[34] measured strengths in polycrystalline CVD diamond using the so-called burst pressure technique (in Valentine et al., the Young's modulus was also measured using the same loading procedure).

Cardinale and Robinson obtained an average fracture strength of 730 MPa for CVD diamond for film thicknesses in the range of 3.5 to 160 μm .^[1] The loading arrangement was effectively treated as an edge-clamped circular membrane under uniform pressure. In this type of loading the stress is assumed to be the same everywhere on the sample. Valentine et al. measured strengths between 746 to 1138 MPa for disk-shaped specimens 179 to 319 μm thick.

In reviewing the work of Cardinale and Robinson, Valentine et al.^[34] noted that the equation used to model the loading may be applicable only to diamond films in the pure membrane regime, i.e., a few microns or less in thickness. By showing the linearity

between the applied load and displacement, Valentine et al. showed that plate equations were necessary (i.e., bending stresses were dominant). In addition, it was found necessary to assume an edge condition intermediate between the simply supported condition and fully clamped condition. The form of the stress state produced by the two conditions is identical and differs only by an added constant.^[35-36] The stress state has a maximum in the center and drops off more slowly away from the center than with the ball-on-ring loading used in the present study. Through the examination of the macroscopic crack pattern of the fractured specimens Valentine et al. concluded that failure occurred at the disk center and the sample strengths calculated from the center stress. A photograph showing the macroscopic crack pattern of a particular fractured specimen was given which was similar in appearance to those of the present study. However, as shown later in this study, the failure origin may not always be at the position of maximum tensile stress.

Transgrannular and Intergrannular Fracture

Valentine et al.^[34] concluded that fracture in polycrystalline CVD diamond was a mixture of transgrannular and intergrannular fracture and therefore the grain boundaries were not inherently weak. However, no photographs of fracture surfaces were shown along with any fractography to support this conclusion. Hoff et al. concluded that fracture was different for the two types of diamond examined: CVD produced diamond and that produced by oxy-acetylene torch (combustion).^[37] The combustion specimens were observed to fracture by intergrannular fracture and the CVD produced diamond by transgrannular fracture. The fracture surface photos shown were not clear, and hence, the qualitative fracture surface analysis given from the photos is difficult to correlate with the photos. Drory et al.^[11] concluded that fracture in polycrystalline CVD was intergrannular and included a photo of a fracture surface. However, no qualitative or quantitative fractography was used to demonstrate this conclusion. The features present in the fracture

surface photo shown are quite similar to several photos given here, some discussion is given in a later section on the fractographic analysis of these features.

Residual Stress Measurement in CVD Diamond Deposited on Silicon

Windischmann et al.^[8] demonstrated the dependence of processing conditions on the residual stress in CVD diamond deposited on silicon. However, the dependence of stress on coating thickness and temperature has received little attention and hence is the primary focus of this study. Using a vibrating membrane technique, Berry et al.^[6] found the room temperature stress in CVD diamond coatings deposited on Silicon at 850°C to be in the range 10-140 MPa (tensile), with a growth stress (intrinsic stress) of about 500 MPa (tensile). Using a curvature method, Baglio et al.^[7] obtained room temperature stresses in the range 4-326 MPa (tensile) with corresponding intrinsic stresses in the range 465-730 MPa for the diamond/Si system with deposition temperatures in the range 775-950°C. Also using a curvature technique, Windischmann et al.^[8] obtained a value of 200 MPa (tensile) for the diamond/Si system coatings deposited at 850°C. However, the value used for the CTE stress at room temperature, -220 MPa, is much lower than calculated here, -479 MPa. This discrepancy was also noted in Baglio et al.,^[7] and the cause is unclear. Using the CTE stress values calculated here gives an intrinsic stress of 679 MPa (tensile).

CHAPTER 5 STRENGTH AND FRACTURE RESULTS FOR GROUP A, SAMPLE SET A.I

The Texas Instruments Study

Fracture properties were measured in a series of CVD diamond samples supplied by Texas Instruments. The goal of this study was to find an optimal set of processing parameters in which the fracture toughness (K_{Ic}) was maximized. This was carried out by systematically varying five processing variables (such as deposition temperature, and gas pressures) to create twenty different "process" conditions. Texas Instruments provided two hundred samples, ten of each "process" condition. The fracture toughness and strength was obtained for 2-3 samples for each "process" condition. The specifics of the processing were not provided by Texas Instruments for proprietary reasons; however, the study offered an unprecedented opportunity to study fracture in CVD diamond with a large sample set. All of the samples were broken with the growth surface (large grain surface) in tension as requested by Texas Instruments since it was thought that the lowest strength would occur on the large grain surface.

Strength vs Thickness

In Fig. 5.1, the strength is plotted as a function of disk thickness for all of the samples of the Texas Instruments study (Group A, sample set A.I) in which failure origins could be found (a total of 52 in all). The strength appears to have a strong correlation with thickness. This is due to either a material property which changes with microstructure or is an artifact of the loading. The greater volume due to the

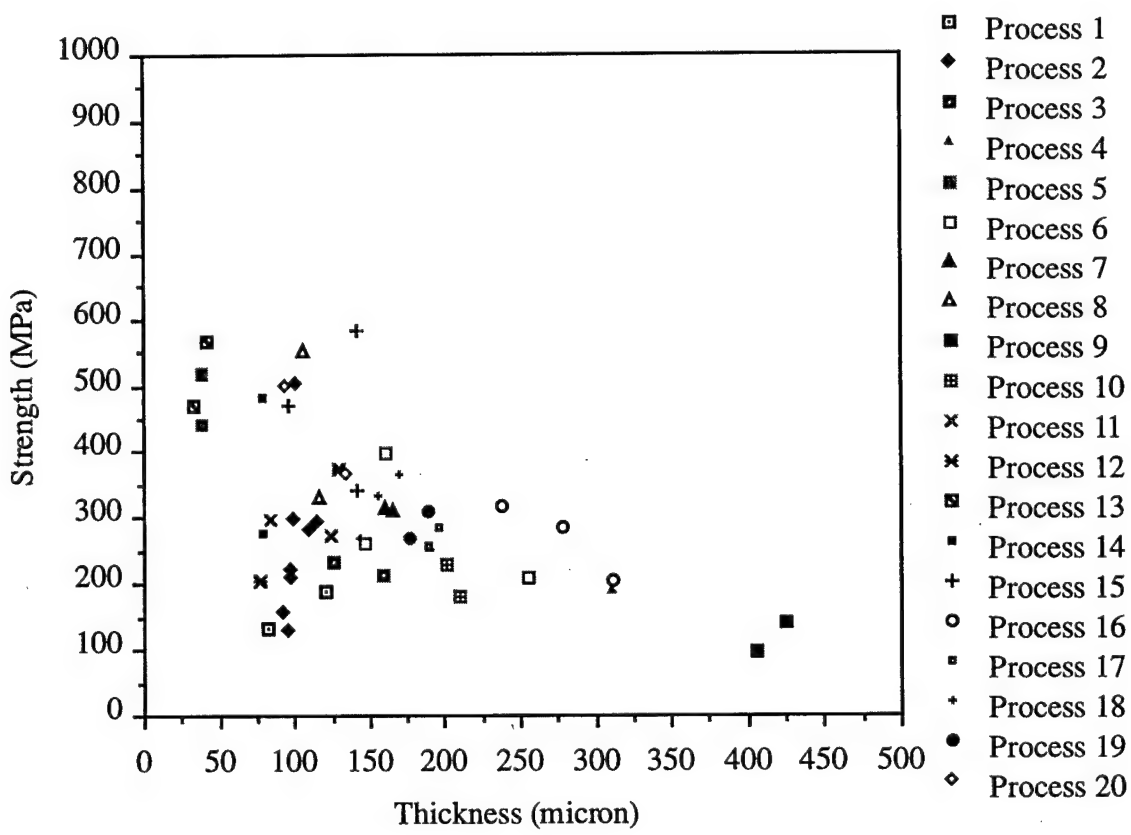


Fig. 5. 1. Strength vs. disk thickness.

increase in thickness would be expected to give a lower strength value due to the increased number of flaws as potential failure origins. However, as stated previously, all of the failure origins were found to be from surface flaws and since the ring diameter was the same for all the samples the area of surface loading is also constant. No difference in strength should have occurred with thickness variation due to failure origin statistics. In what follows, the increase of strength with thickness will be examined more closely.

Maximum Stress and Failure Load vs. Thickness

For most of the samples, failure origins could not be found. However, maximum stress (center stress at failure) and failure load data were available. These are shown as a function of thickness in Fig. 5.2 and Fig. 5.3. The maximum stress data (Fig. 5.2) follow the same trend as the strength vs. thickness plot (Fig. 5.1). As the thickness is decreased from the highest thickness (about 430 μm) the maximum stress is relatively constant (at a value of about 500 MPa) until about 125-150 μm , then the maximum stress begins to rapidly increase with further decrease in thickness. This trend appears to occur for the strength also but due to the smaller amount of data is not as apparent. The maximum stress appears to be unacceptably high for the thinnest samples, i.e., one sample (process 13) apparently survived a stress of over 2700 MPa and several others over 1700 MPa within the small region surrounding the center of the disk. Physically, this seems unlikely since the failure stress is an order of magnitude lower (i.e., 100-550 MPa). For the thinnest samples it is likely that the high maximum stresses may be due to the deflection of the disk entering the large deflection regime which would have the effect of overestimating the stress.

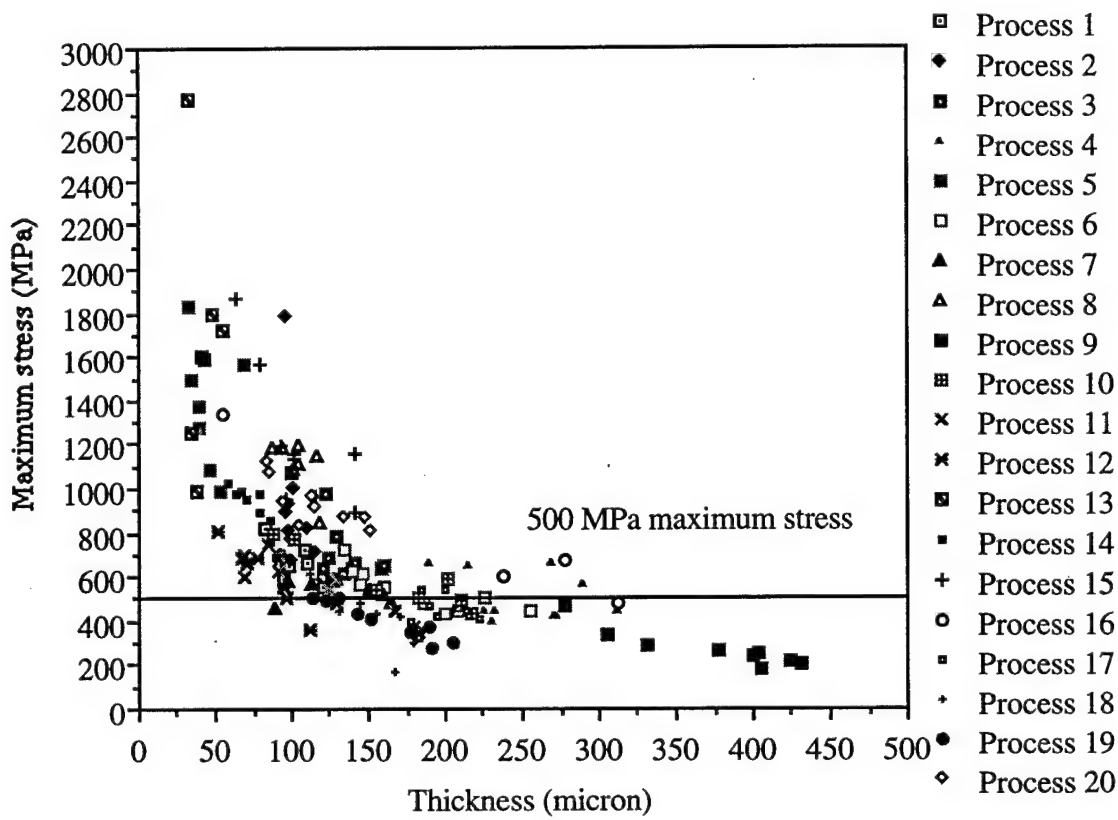


Fig. 5.2 Maximum stress (center stress at failure) vs. disk thickness.

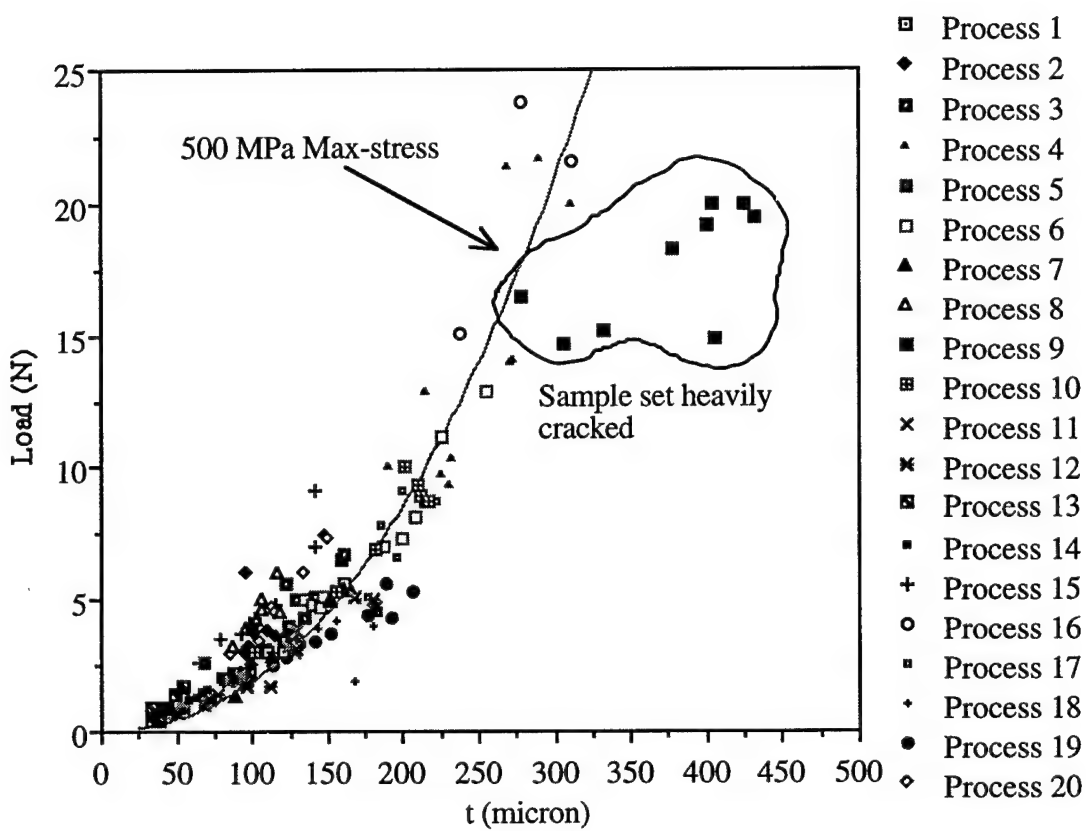


Fig. 5.3 Failure load vs. disk thickness.

The failure load vs. thickness relation is independent of the stress/thickness ball-on-ring relations in eqns. 2.8-2.11, i.e., it reflects only direct measurements and not the results of equations as are the stress and maximum stress vs. thickness relations. In Fig. 5.3, the failure load is seen to have the opposite trend with increase in thickness than that of the strength and maximum stress, i.e., the failure load increases with increase in thickness, as expected. The plot appears to branch off with increase in thickness after about 275 μm . One branch is the set of highest thickness samples (process 9) and the other branch shows a rapid increase of failure load with thickness. The line shown in Fig. 5.3 is the load calculated through eqn. 2.8 assuming a maximum stress of 500 MPa. The constant maximum stress was chosen as 500 MPa because this is roughly the constant value in the maximum stress vs. thickness plot (Fig. 5.2) for the thickness range 125-430 μm . The process 9 samples were re-inspected optically to see if any evidence could be found to explain why the set deviates so markedly from the 500 MPa maximum stress line which all other data appear to follow. The samples were found to be heavily cracked with a network of cracks as opposed to the other samples which only occasionally contained a few crushing cracks (i.e., cracks due to loading of the sample after fracture has occurred). The cracks were only visible with careful inspection by changing the direction of the lighting. It is clear that the cracks existed previous to fracture and hence may contribute to the degradation of the strength and fracture toughness. In many of plots involving strength, maximum stress, load, and thickness, these samples (process 9) appear to be anomalous with respect to the form of the general trend of the remaining data.

Maximum Stress vs. Load

The maximum stress should be independent of load (and strength) since a high maximum stress could be achievable under a low load (if the sample was very thin) or a high load (the high load may occur due to high sample strength). A plot of maximum

stress vs. load is shown in Fig. 5.4. In Fig. 5.4, for loads above about 10 N, the maximum stress is randomly scattered about the 500 MPa maximum stress shown for reference. For loads below 10 N, the maximum stress rises rapidly with further decrease in load from 10 N down to zero load. The 500 MPa maximum stress line was useful in identifying the set of heavily cracked samples (process 9) which deviated from the general trend of the load vs. thickness data (Fig. 5.3). From Figs. 5.1-5.4, it is clear that as the thickness decreases below about 150-175 μm , the strength and maximum stress increase rapidly. The load is measured directly and is independent of eqns. 2.8-2.11, which used the load and thickness to obtain values for $\sigma_\theta(r)$, and $\sigma_{\text{Max}}(r)$. Intuitively, the load must be a function of the thickness since a thick disk should survive a higher load than a thin disk.

The rapid increase of $\sigma_\theta(r)$ and $\sigma_{\text{Max}}(r)$ with decrease in thickness below about 150-175 μm may be due to an inaccuracy in eqns. 2.8-2.11 due to the deflection of the disk entering the large deflection regime. The linear (or small deflection) solution for the stresses in a circular plate is valid only when the deflection, ω , is less than about half the thickness, t , of the plate.^[35,36,38] When $\omega > t/2$, stresses due to stretching of the plate (membrane stresses) exist, which in turn, alter the bending stresses of the plate. If the large deflection condition is exceeded, $\sigma_\theta(r)$ and $\sigma_{\text{Max}}(r)$ are overstated by the linear solution.

An approximate solution for the tangential stress component for the case of moderately large deflection was developed using the strain energy method and the computer program MathematicaTM. The derivation and verification of the computer program large deflection solution is given in Appendix I. The tangential stress at some radial position is now the sum of the tangential membrane stress and tangential bending stress at that position.

In recalculating the stresses, it was found that there was virtually no difference between the large deflection solution and linear solution unless the thickness of the disks

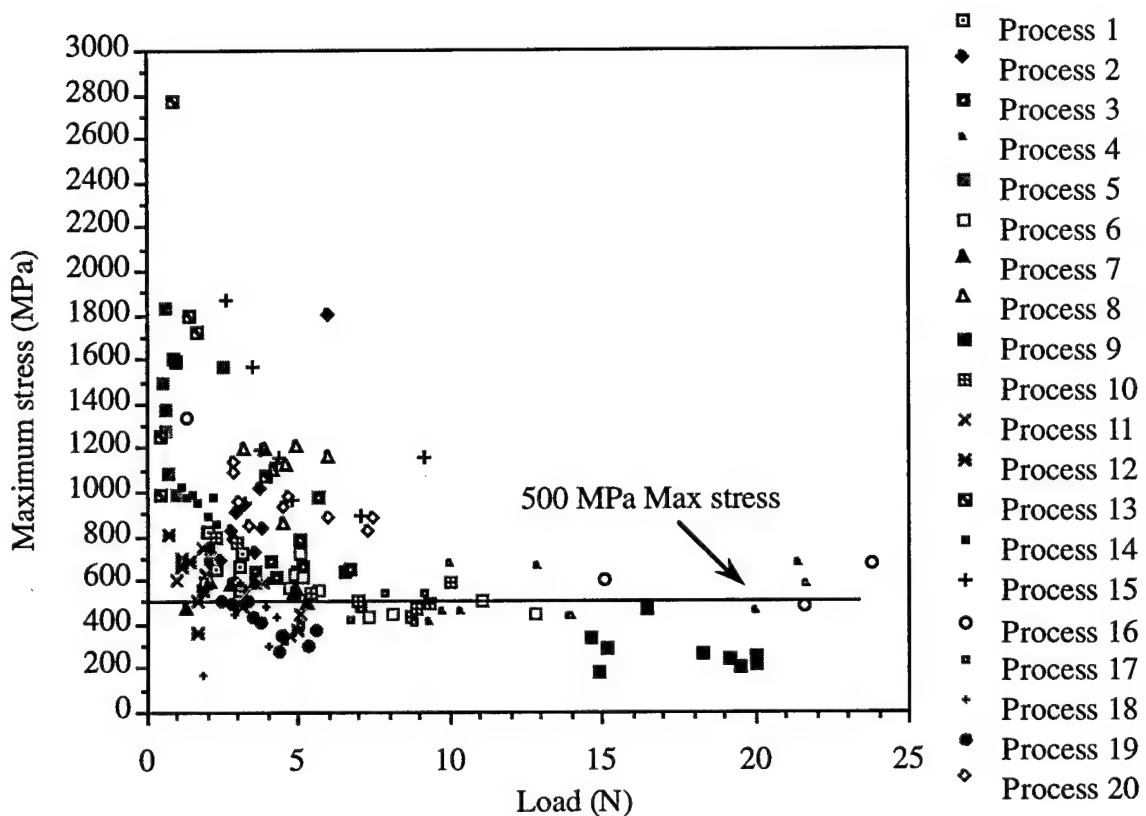


Fig. 5.4 Maximum stress (center stress at failure) vs. failure load.

was less than about 100 μm . Between 90-100 μm , the difference between the two solutions was between about 8-5%. However, between about 50-30 μm , the difference increased about 30-125%, respectively.

Only the strength and maximum stress are changed by the large deflection solution, so the $\sigma_\theta(r)$ vs. t , $\sigma_{\text{Max}}(r)$ vs. t , and $\sigma_{\text{Max}}(r)$ vs. load plots (Figs. 5.1, 5.2, and 5.4, respectively) were re-plotted and shown in Figs. 5.5-5.7, respectively. Comparing the new plots with the previous ones, the highest stress values (which occurred for the thinnest samples) are reduced whereas the majority of the data remains unchanged. The increase in stress values with decrease in thickness still exists but is less rapid.

The highest maximum stresses for the samples using the linear model were over 2700 MPa with several others over 1700 MPa. These values appear to be surprisingly high. The highest maximum stress of the large deflection corrected solution is 1600 MPa with several samples surviving 1300-1500 MPa within the small area surrounding the center of the sample. This seems more reasonable with respect to the failure stresses (100-550 MPa) obtained before.

Relationships Between Flaw Size, Sample Thickness, Fracture Toughness, and Strength

The critical flaw size and sample thickness relationship is shown in Fig. 5.8. The critical flaw size increases linearly with increase in sample thickness with the critical flaw size being about one third the thickness. The cause of this is likely due to unintended pre-testing carried out in the processing. The larger the critical flaw size, the smaller the stress required to cause fracture. Obviously, the flaw size is restricted by the thickness, i.e., the flaw size can not be greater than the thickness. In addition, if the flaw size is very large in relation to the thickness, the slightest stress applied on the sample during handling or incurred during processing would be sufficient to fracture the sample. Hence, cracked

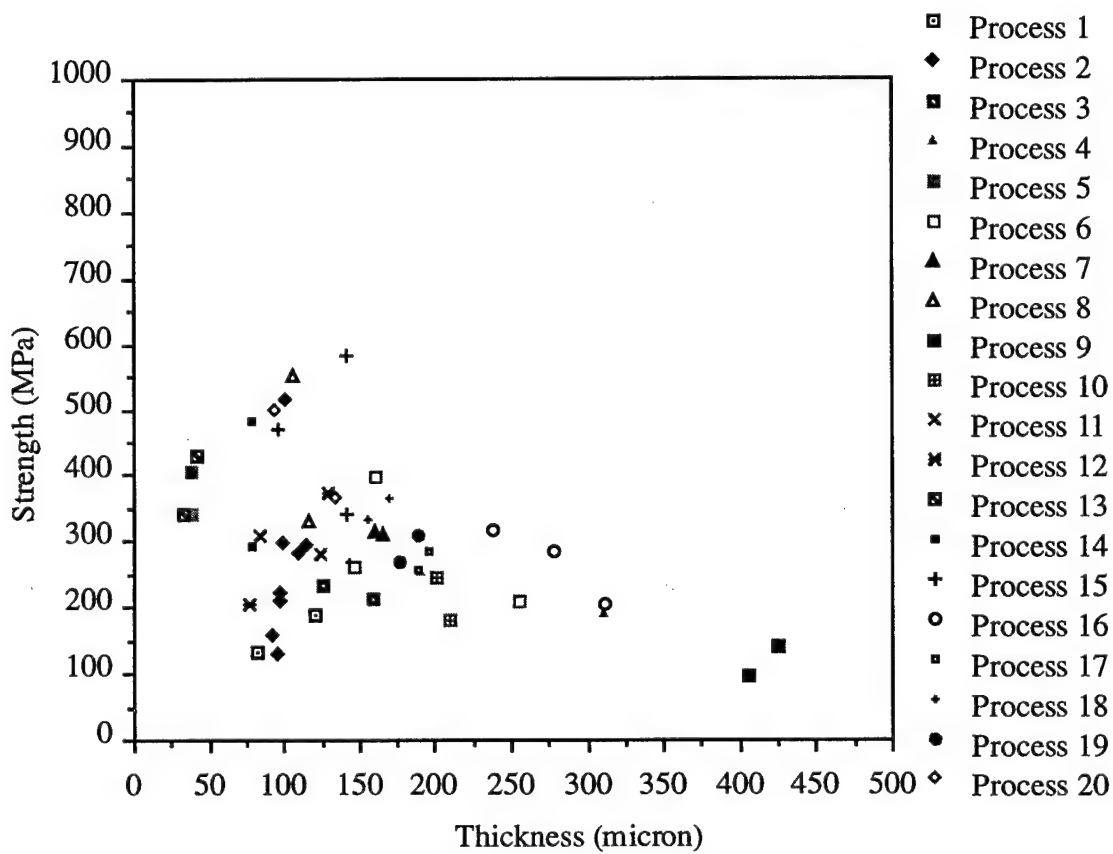


Fig. 5.5 Large deflection strength vs. thickness.

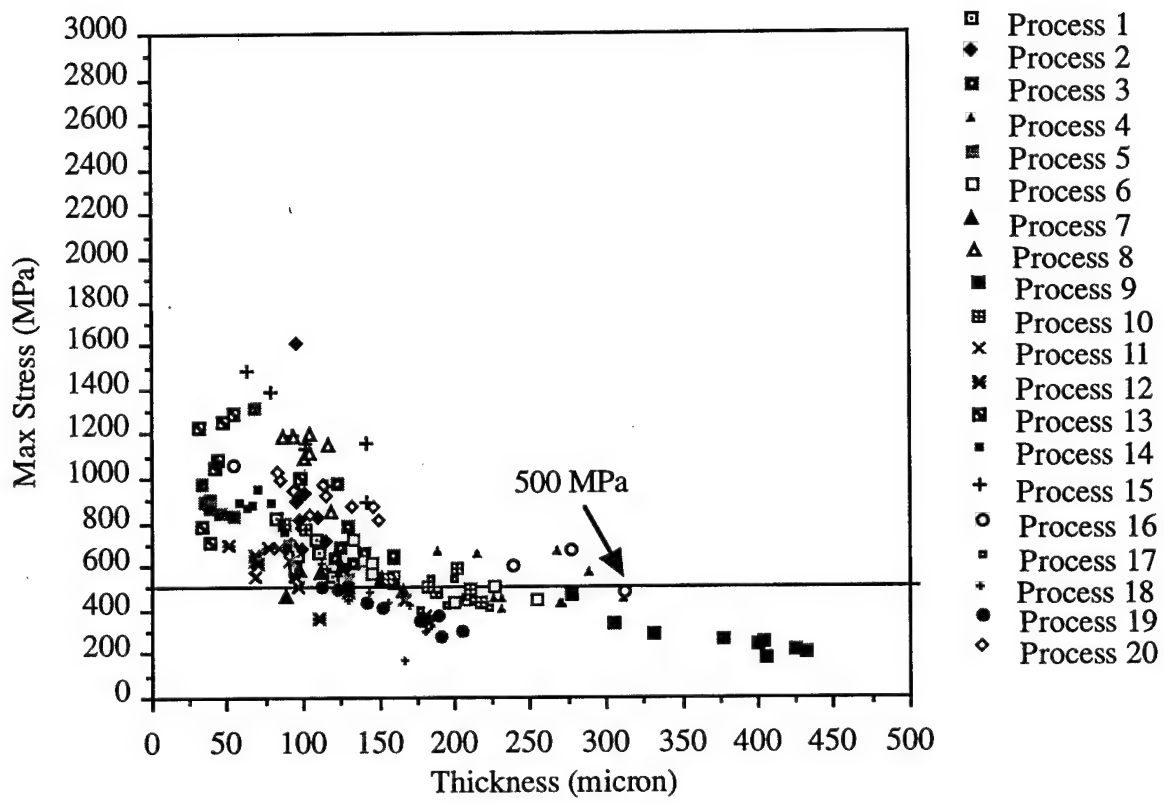


Fig. 5.6 Large deflection maximum stress vs. thickness.

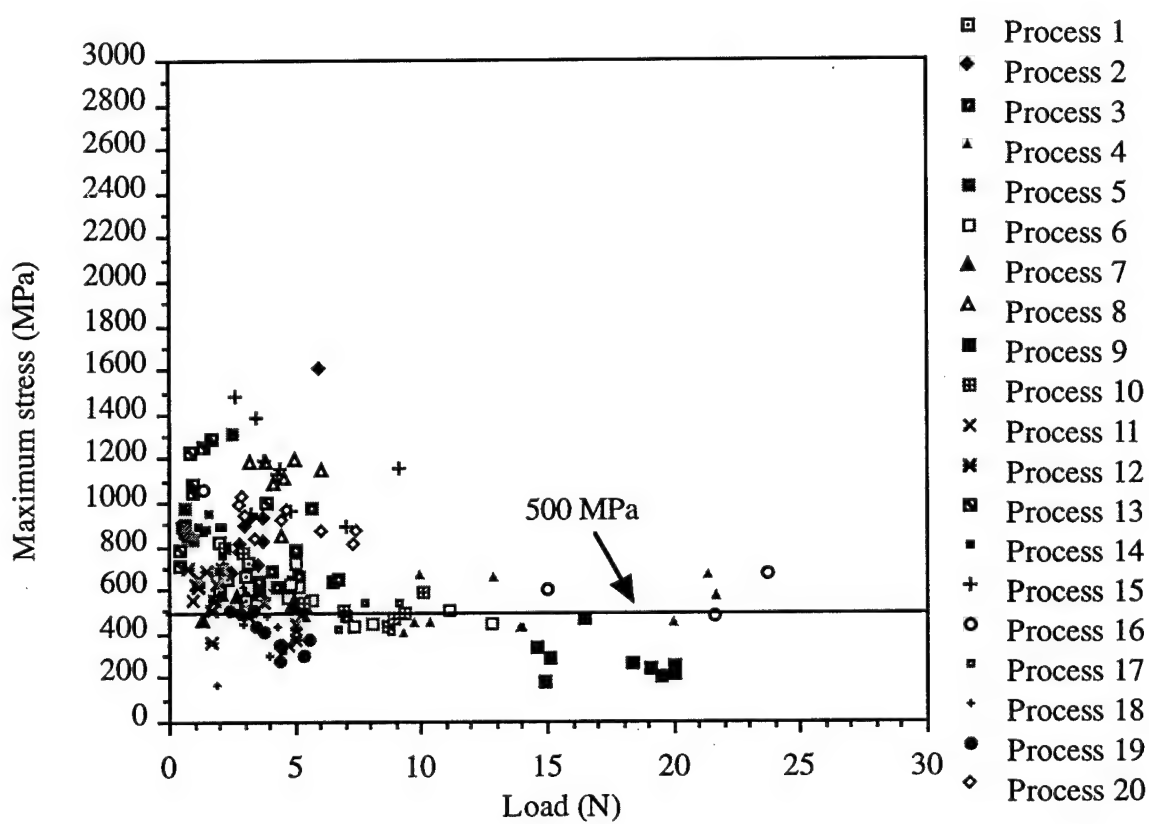


Fig. 5.7 Large deflection maximum stress vs. load.

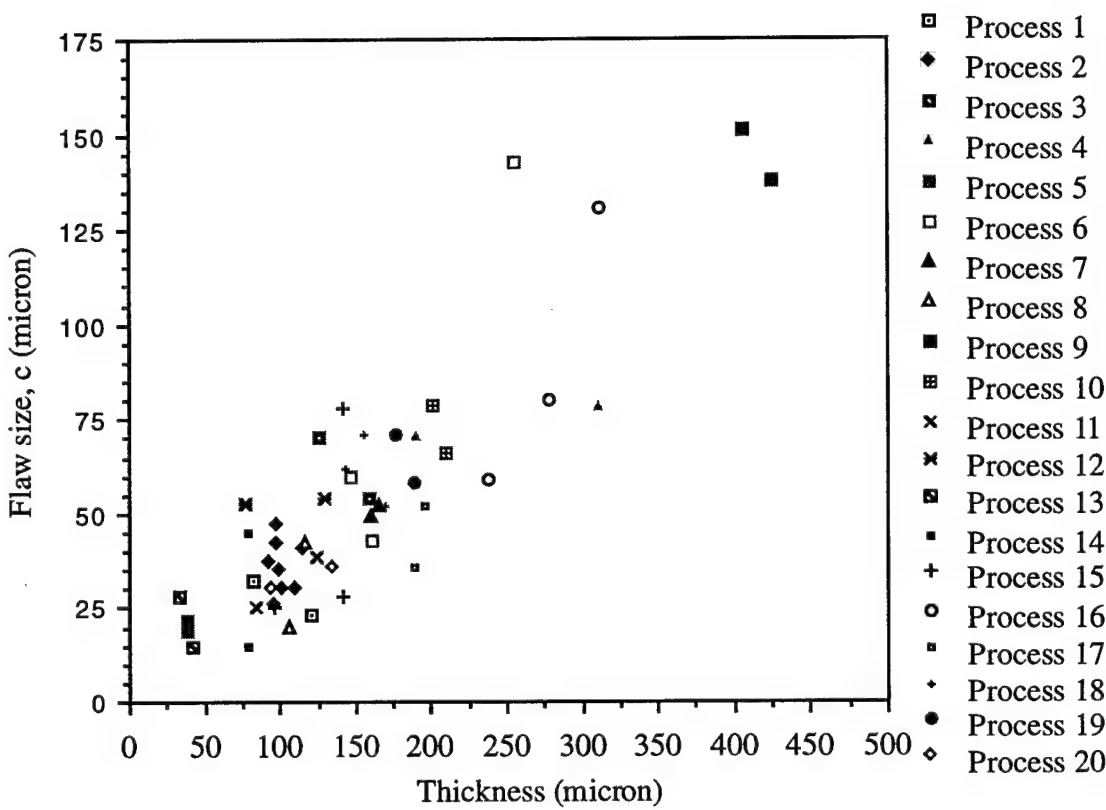


Fig. 5.8 Plot of critical flaw size vs. sample thickness.

samples would be discarded prior to testing and would not contribute to the fracture statistics.

The critical fracture toughness and flaw size relationship is shown in Fig. 5.9. There is no obvious relationship between the critical fracture toughness and the flaw size. The critical fracture toughness appears to be randomly scattered in relation to the flaw size.

The critical fracture toughness (calculated using eqn. 2.4) and sample thickness relationship is shown in Fig. 5.10. The critical fracture toughness also appears to be randomly scattered in relation to the sample thickness. This would be expected since the flaw size is linearly related to the sample thickness (Fig. 5.8). Hence, if the critical fracture toughness is random with flaw size, it should also be random with thickness.

The strength and critical flaw size relationship is shown in Fig. 5.11. The strength follows the critical flaw size in similar fashion as the relationship with sample thickness (Fig. 5.1). This would be expected since the flaw size is linearly related to the sample thickness (Fig. 5.8). Hence, if the strength decreases with increase in thickness the relationship between strength and flaw size should be similar.

Superimposed on the strength and critical flaw size plot in Fig. 5.11 are the strengths predicted by eqn. 2.4 for a given critical flaw size assuming K_{Ic} values of 2.0 and 3.0 MPa \sqrt{m} . These values of K_{Ic} were chosen because they roughly bracket the range of values for K_{Ic} obtained in the study of the set A.I samples. The data in Fig. 5.11 appear to follow the relationship between strength and critical flaw size predicted by eqn. 2.4.

After correcting for large deflection, and examining the relationships between the strength, critical flaw size, K_{Ic} , and sample thickness, an explanation for the rapid increase in strength with sample thickness (Fig. 5.1) can now be made. Previously, it was surmised that the increase in strength with sample thickness may be due to a material property change with thickness. However, as shown in Figs. 5.9 and 5.10, K_{Ic} , which is a material property, is randomly scattered with respect to thickness and critical flaw size. The critical flaw size was shown to be linearly related to the sample thickness (Fig. 5.8).

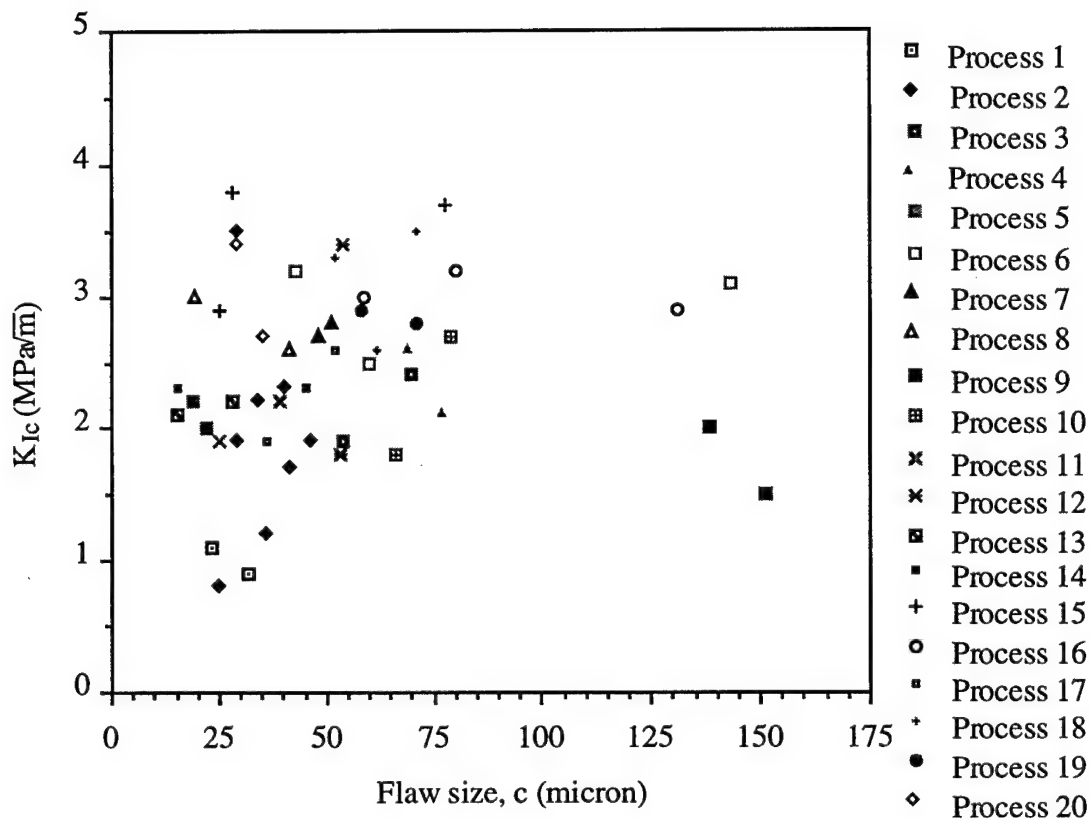


Fig. 5.9 Plot of critical fracture toughness vs. flaw size.

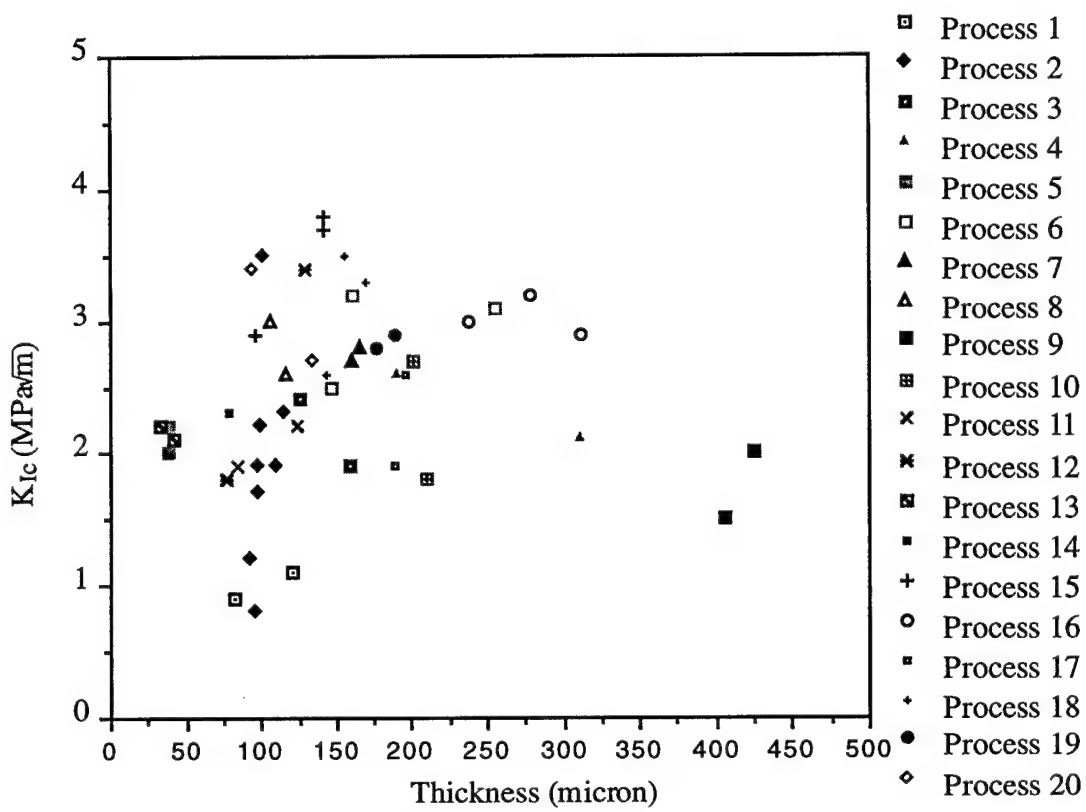


Fig. 5.10 Plot of critical fracture toughness vs. sample thickness.

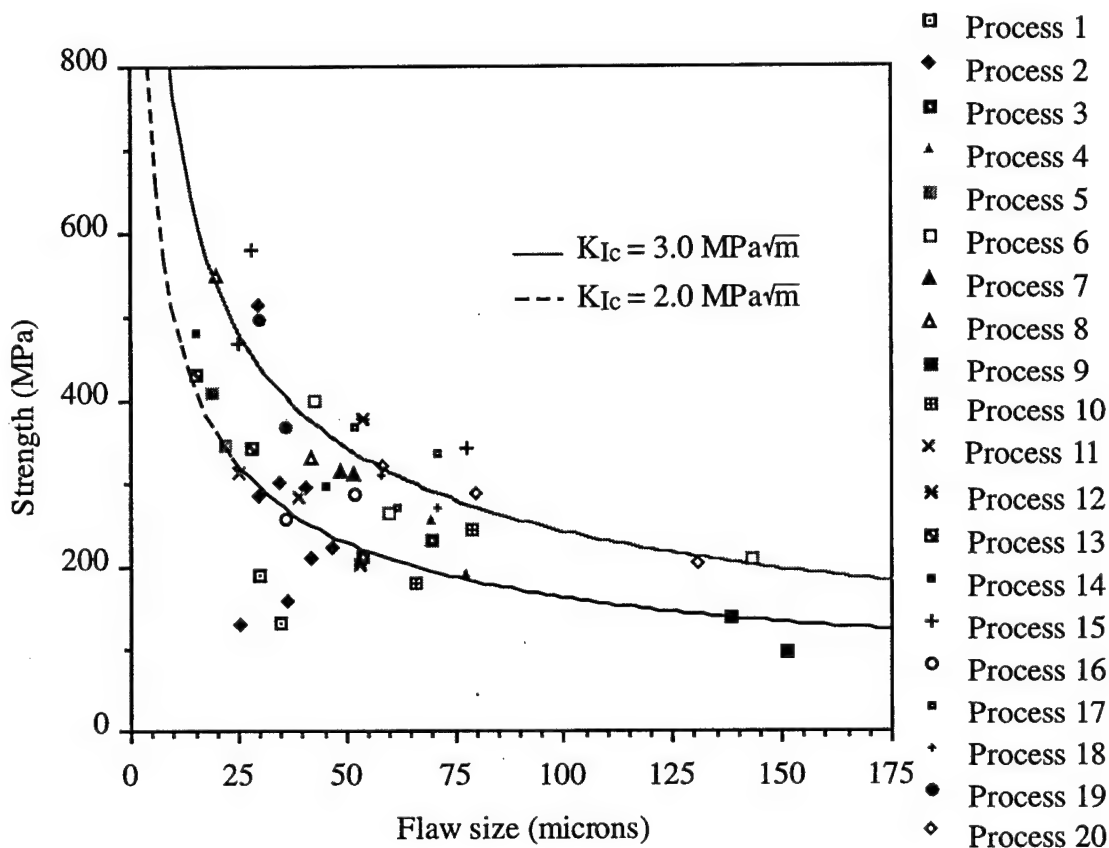


Fig. 5.11 Plot of strength vs. critical flaw size. Superimposed on the plot are the strengths predicted by eqn. 2.4 for a given critical flaw size assuming K_{Ic} values of 2.0 and 3.0 $\text{MPa}\sqrt{\text{m}}$.

The increase in strength with sample thickness therefore follows the increase of strength with critical flaw size which is dictated by eqn. 2.4. However, preexisting cracks in the samples (which are potential failure origins upon loading) increase in size with thickness, which in turn, decreases the strength.

Sharp vs. Blunt Cracks

As stated previously, in using eqns. 2.1-2.4 it was assumed that the cracks were atomically sharp. Failure from a blunt crack will give a K_{Ic} value much higher than that from a sharp crack, and as such, is not useful as a material property. Consideration must be made as to whether or not the failure origins (cracks) examined in this study are in fact sharp or can be considered as sharp. The question as to whether the failure origins examined were from blunt or atomically sharp cracks is not obvious by observation of the fracture surface.

In Fig. 5.11, it is clear that the strength and flaw size (which are independently measured) obey the relationship of eqn. 2.4. If all or some of the samples for which failure origins were located and measured were indeed blunt cracks, then the data would not readily follow eqn. 2.4. For the few strength values which fall below the curve, the reason for the deviation would have to be other than blunt cracks such as residual stress. For blunt cracks we would expect the strength to be greater than the prediction of eqn. 2.4, i.e., the strength would be larger for a given crack size.

CHAPTER 6 FLAW SHAPE DISTRIBUTION

The flaw shape (a/b ratio) distribution for the Texas Instruments study (set A.I) is shown in Fig. 6.1, where the flaw shape is characterized by the a/b ratio (a is defined as the depth of the flaw and b the half width). Mecholsky et al.^[39] demonstrated that the flaw shape distribution could separate different flaw types which are created by different mechanisms. The flaw shape distribution shown in Fig. 6.1 is clearly of one type, i.e., there is one distinct peak in the distribution. Hence, all the flaws are likely to be caused by the same stress field. Interestingly, the flaw shape distribution is skewed to the left as were the two distributions in the study of Mecholsky et al. This skewed distribution implies that a similar stress field existed which caused similar flaw shapes.

The average a/b ratio and the spread (one standard deviation) for the flaws in the diamond disks is 1.61 ± 0.7 . By fracturing glass bars parallel and perpendicular to the direction of grinding, Mecholsky et al.^[39] demonstrated that two different flaw types were observed as failure origins on the fracture surface. Along the direction of grinding, elongated flaws were created by the joining together of smaller flaws to make long and shallow flaws of average a/b ratio 0.5. Perpendicular to the direction of grinding, the flaws were found to be radial cracks which were created in a manner similar to the radial/median cracks created through Vickers indentation (when the load is sufficiently high to produce radial/median cracks such that $c \geq 2c'$, where c is the radius of the radial/median crack, and c' the diameter of the indent impression).^[31]

Ideally, the radial cracks produced by Vickers indentation are semicircular, i.e., the a/b ratio should be one.^[40] Marshall showed that for indents, the a/b ratio is ≈ 0.8 .^[41]

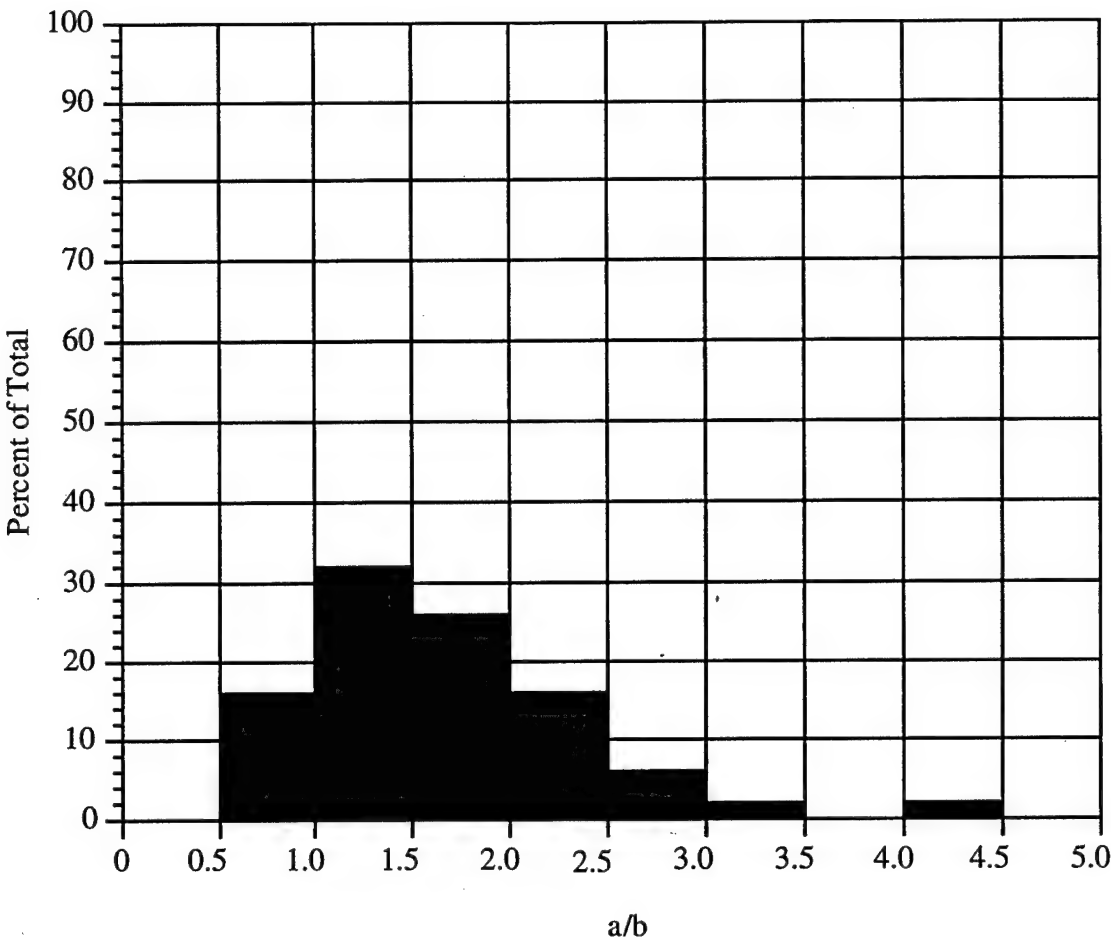


Fig. 6.1 Flaw shape (a/b ratio) Distribution for the Texas Instruments Study (set A.I).

Tsai et al. demonstrated in single crystal silicon that the shape of the critical flaw (and corresponding fracture mirror) is related to the local elastic constant.^[30] The change in the average a/b ratio measured here (compare 1.6 to 0.8) may be due to the elastic anisotropy from the elongated grain structure.

With ceramics, the strength for a given crack size, for cracks produced by Vickers indentation, is less than that for cracks produced by non-contact means. This is due to the local contact residual stress and can be seen through the modification of eqn. 2.4 to yield eqn. 2.12.^[31] Similarly, surface treatments such as polishing, grinding, and machining, remove material through microscopic fracture caused by contact forces.^[27] These surface

treatments can cause a decrease in strength (for a given crack size) because of contact residual stresses just as in the case of a Vickers indentation crack.

The flaw sizes measured from the fracture surface are most likely either the original crack prior to loading or very close to the critical size just before catastrophic failure.^[39] Flaw growth may occur upon loading, but it is not uniform with time; the largest part of flaw growth occurs just prior to catastrophic failure. The critical size measured from the fracture surface is therefore very close to the size of the preexisting crack.^[39] In addition, it is highly unlikely that the preexisting (e.g., failure initiating) flaw would exist on a plane surface exactly perpendicular to the direction of the maximum principal stress in the specimen. The flaw therefore must propagate on a surface oriented in a direction slightly different than that of the surface containing the preexisting flaw. This tends to form a demarcation which is detectable and constitutes the measured critical flaw.^[42] Indeed, knowledge of this effect was helpful in determining the trace of the critical flaw in some samples where the fracture topography obscured some of the boundary of the critical flaw.

Most of the flaws in the Texas Instruments study (sample set A.I) were quite irregularly shaped with regards to the shape of the periphery. Cracks which grow under the action of slow crack growth tend to have a smooth shaped periphery.^[43] This precludes any corrosion or chemical/stress cause and points to a purely mechanical cause of the cracks.

The results of the flaw distribution study indicate that the flaws were caused by some mechanical means rather than chemical or corrosion effects or processing defects. Some possible explanations:

- I.) Subsequent handling after fabrication, i.e., handling with tweezers, or some other tool contact.

II.) Mechanical stressing during fabrication, e.g., high residual stresses during fabrication between the growth substrate and coating or high grain to grain microresidual stresses within the specimens.

III.) Thick CVD diamond such as that examined in the present study are deposited through the use of an oxygen-acetylene torch. During deposition the torch is on until the desired thickness is achieved and the torch is then extinguished causing rapid cooling. This rapid cooling presents the possibility of thermal shock induced cracking.

IV.) The a/b distribution (single mode with near semicircular crack shape) is consistent with a mechanical cause in a similar way as the Vickers indentation produced radial/median cracks.

CHAPTER 7

RESULTS OBTAINED FROM SAMPLES FROM OTHER SOURCES

Description of Figures

Data were also obtained from polycrystalline CVD diamond disk samples obtained from various other sources, i.e., Raytheon Corp., Norton Co., and Texas Instruments. The Texas Instruments samples were processed differently than those of the Texas Instruments study (set A.I) investigated previously and are labeled Group A set II, III. Since the details of the processing conditions (and in some cases the results) were to remain confidential, the samples from the different sources will be labeled as Group B set I, II, and III to maintain the confidentiality of the results. The data for Group A and B is tabulated in Appendices II-V. The fracture toughness, K_{Ic} , for the combined data is plotted as a function of critical flaw size and sample thickness, respectively, in Fig. 7.1 and Fig. 7.2, respectively. For the combined data; the critical flaw size is plotted as a function of sample thickness in Fig. 7.3, the strength as a function of flaw size in Fig. 7.4, and the maximum stress as a function of sample thickness in Fig. 7.5.

Fracture Toughness, Flaw Size, and Sample Thickness

The fracture toughness, K_{Ic} , is randomly scattered with respect to critical flaw size (Fig. 7.1) and sample thickness (Fig. 7.2). This follows the relationship shown previously for the Texas Instruments study (set A.I) . The relationship between critical flaw size and sample thickness (Fig. 7.3) is similar to that shown previously. As the thickness increases from the thinnest samples it is first linear with critical flaw size. Above

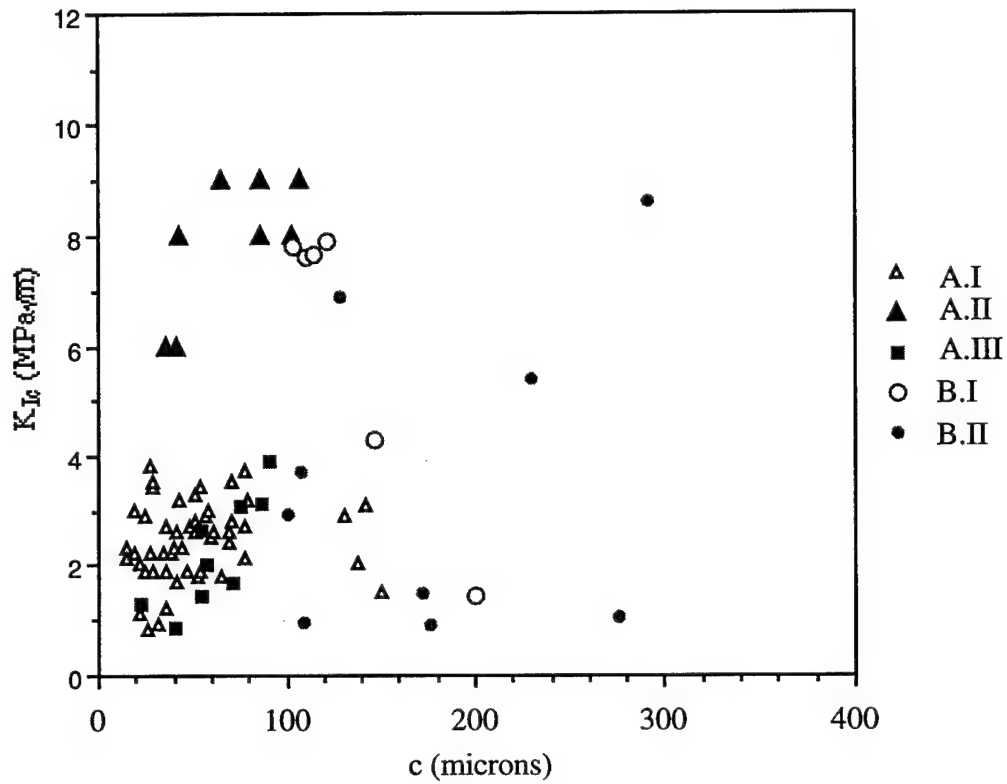


Fig. 7.1 The plot of fracture toughness, K_{Ic} , vs. critical flaw size for the combined data.

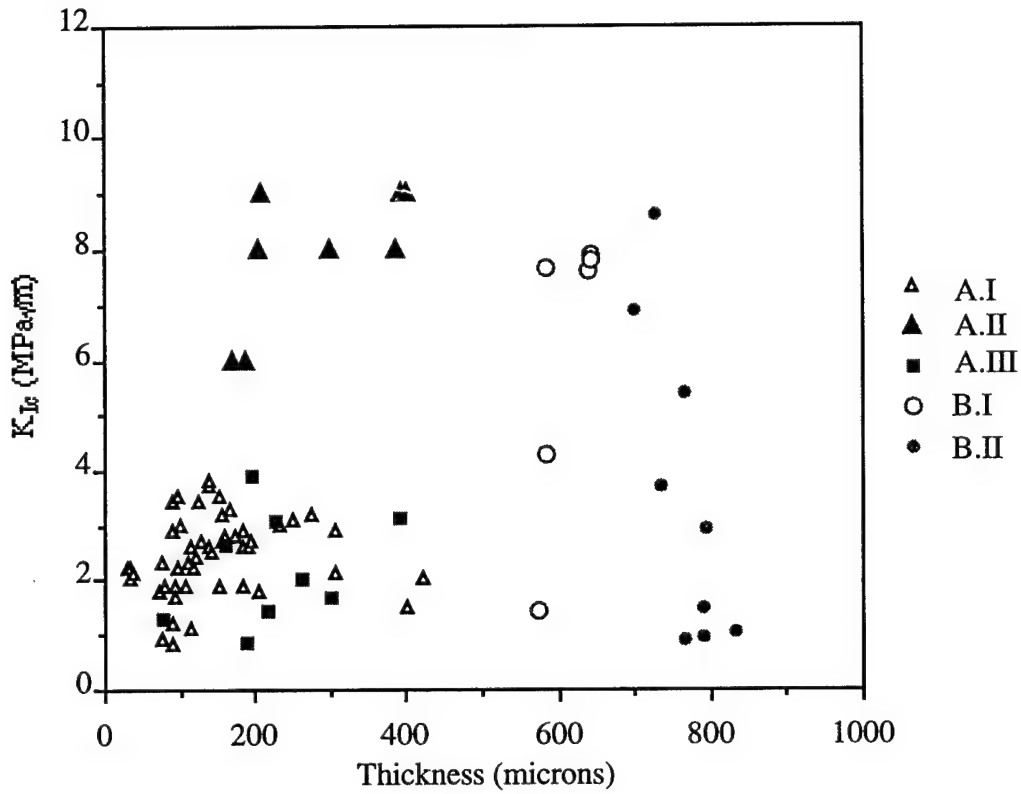


Fig. 7.2 The plot of fracture toughness, K_{Ic} , vs. sample thickness for the combined data.

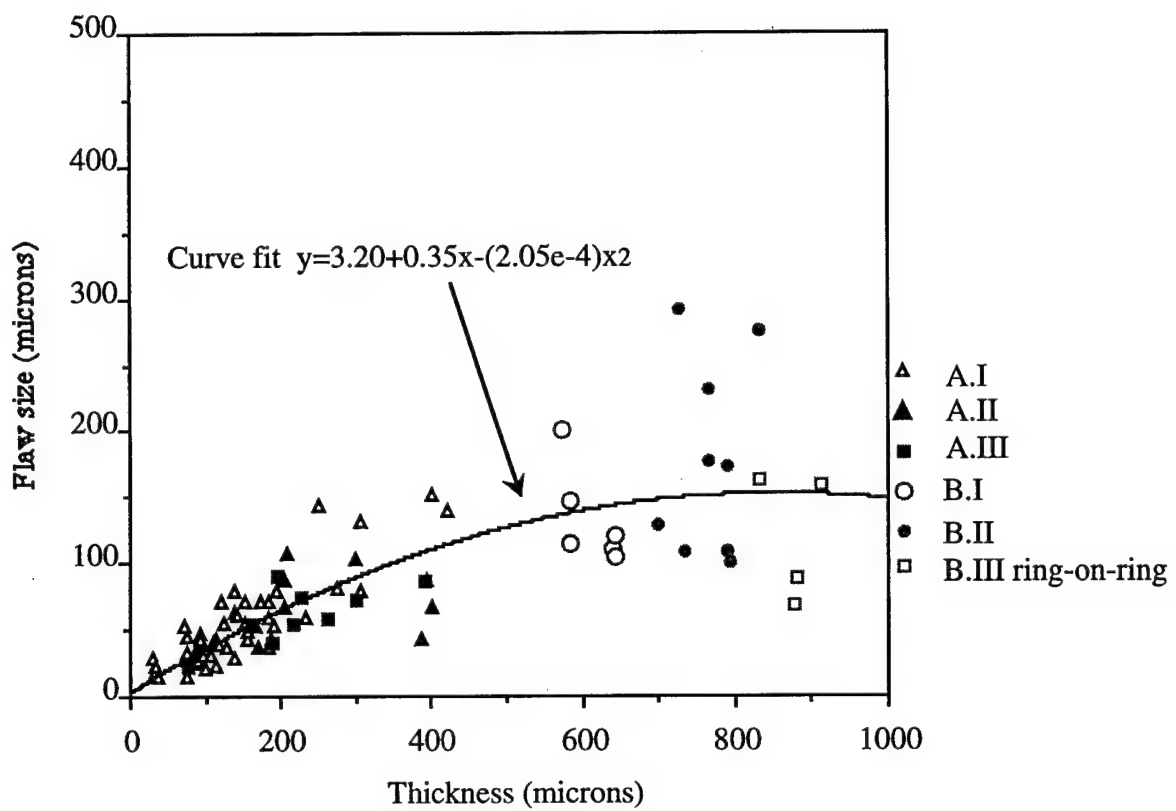


Fig. 7.3 The plot of critical flaw size vs. sample thickness for the combined data.

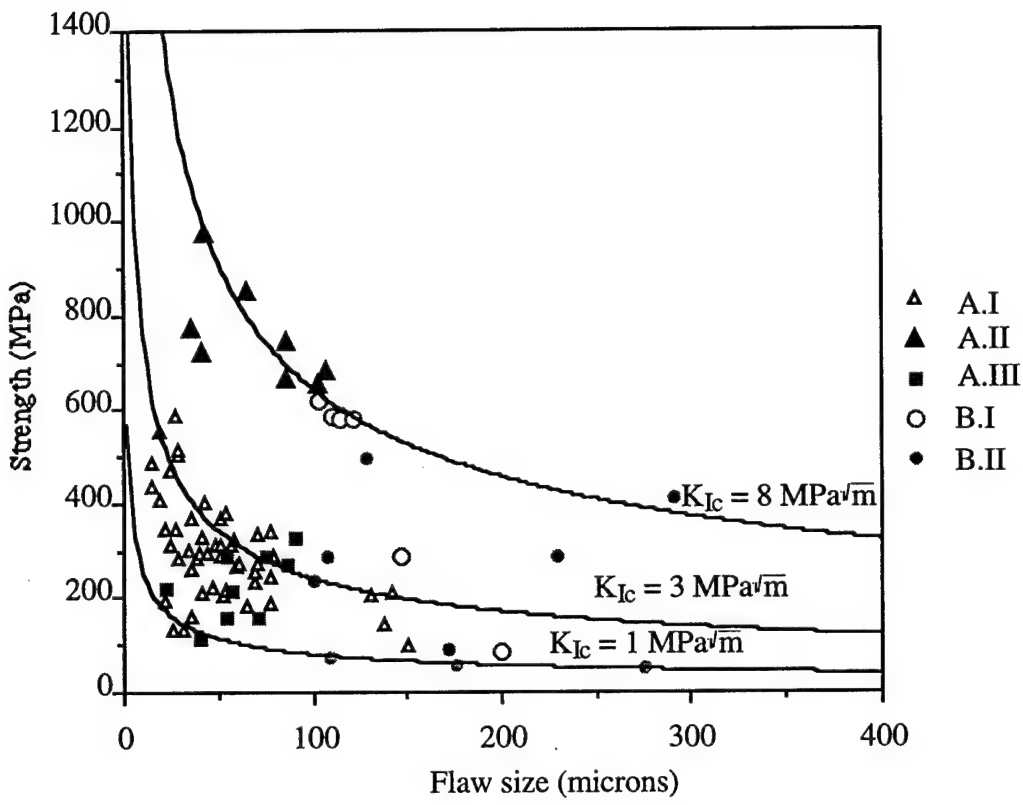


Fig. 7.4 The plot of strength vs. critical flaw for the combined data (Group A, set A, labeled as A.I, was shown previously). Superimposed on the plot are strengths predicted by eqn. 2.4 for a given critical flaw size assuming K_{Ic} values of 2.0, 3.0, and 8.0 $\text{MPa}\sqrt{\text{m}}$.

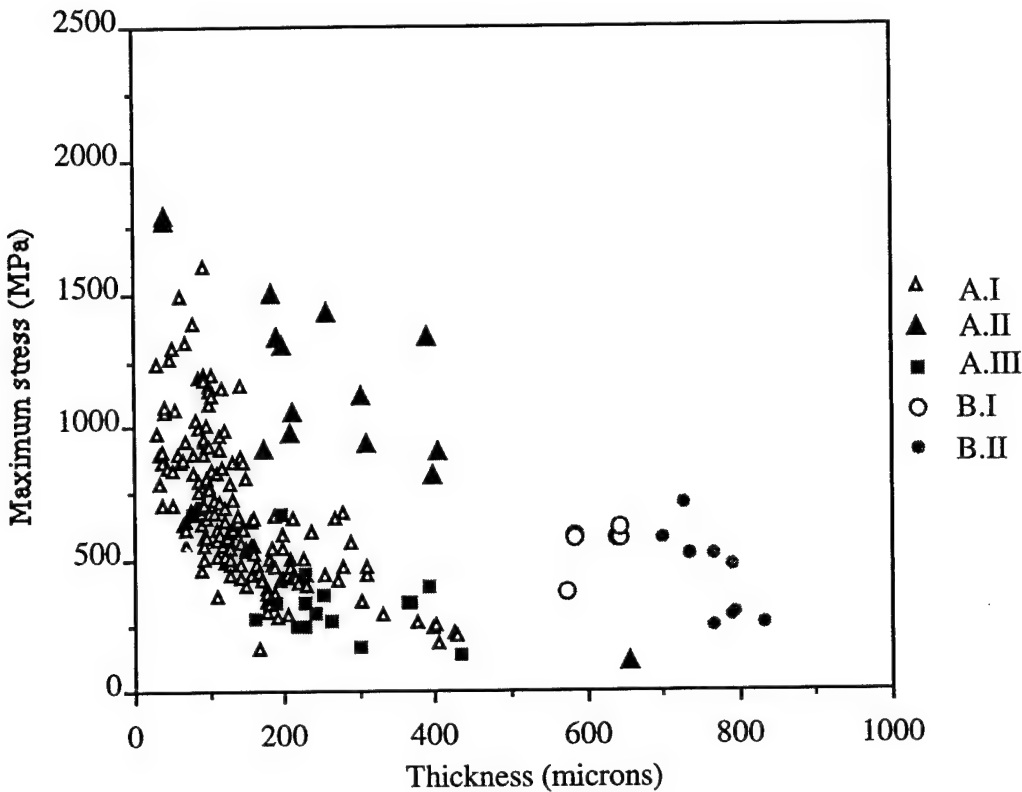


Fig. 7.5 Plot of maximum stress vs. sample thickness for the combined data.

a sample thickness of about 400 μm the flaw size is roughly constant with further increase in sample thickness. As an aid in viewing this trend a second order polynomial curve fit is also shown on the plot. This indicates that the critical flaw size is first limited by the thickness as described previously. Above a sample thickness of about 400 μm a constant flaw size is reached which is independent of sample thickness. In the flaw size vs. thickness plot of the combined data (Fig. 7.3) are shown several data labeled B.III ring-on-ring. These data are from samples from the various sources listed previously which were broken elsewhere in ring-on-ring loading and then donated for the purpose of fracture surface analysis. The samples were the largest examined in this study (i.e., diameter 2.54 cm and thickness averaging about 900 μm). Flaw sizes were found for several of these samples and since they represent data of very thick polycrystalline CVD diamond it was added to this plot in order to extend the information shown to higher thicknesses.

However, since the loading is quite different than that used in this study the strength information was omitted from the corresponding plot.

Strength, Maximum Stress, Critical Flaw Size, and Sample Thickness

Superimposed on the strength and critical flaw size plot in Fig. 7.4 are strengths predicted by eqn. 2.4 for a given critical flaw size assuming K_{Ic} values of 2.0, 3.0, and 8.0 MPa \sqrt{m} . The K_{Ic} values of 2.0 and 3.0 MPa \sqrt{m} bracket the results of the TI-study (set A.I) as previously shown. In addition, the value of 8.0 MPa \sqrt{m} was also superimposed on Fig. 7.4. The set of samples, A.II, appear to fall along the $K_{Ic} = 8.0$ MPa \sqrt{m} line. The data of B.I and B.II do not fall along any constant K_{Ic} line. Sample set A.III appears to be roughly bracketed between the $K_{Ic} = 2.0$ and 3.0 MPa \sqrt{m} line but the amount of data is insufficient to determine if the data follows eqn. 2.4. However, if we examine the maximum stress vs. sample thickness shown in Fig. 7.5, a much greater amount of strength related data for sample set A.III is shown. If we consider that the flaw size is linear with sample thickness for sample thicknesses under 400 μm as shown previously (Fig. 7.3), then sample set A.III can be seen to follow the form of eqn. 2.4 more closely.

The results shown here emphasize that different fabrication processes produce different CVD diamond material. Some processes result in high toughness material and other processes result in low toughness material. The key to future success in producing high toughness CVD diamond is reliability.

CHAPTER 8

THE EFFECT OF SAMPLE POLISHING AND CHOICE OF SAMPLE FRACTURE SURFACE

Fracture of Polished Specimens

In the combined data some of the samples were polished by the manufacturers to a fine optical finish. The purpose of the polishing was to increase the strength by reducing the size of the surface cracks.

In sample set A.II, six of the sixteen samples were polished in order to examine the effect of polishing on fracture. In Fig. 8.1, the strength and flaw size relationship is shown with the polished specimens in black. There is no apparent difference in either strength or flaw size due to the polishing, however, the amount of data is limited.

All of the samples in sets B.I, B.II, and B.III, were polished. Therefore, all of the samples above 500 μm were polished samples. This may explain why the flaw size appears to level off with increase in thickness above 400-500 μm (Fig. 7.3).

Fracture on the Substrate Surface

Nearly all of the samples in the combined data were fractured on the growth surface. Two of the samples in set A.III and six samples in set B.II were broken on the substrate adjacent surface to examine the effect of sample surface choice on fracture. The substrate adjacent surface is composed of randomly oriented grains ranging from submicron dimensions to several microns in size. The growth surface grain size is of the order of about one quarter the sample thickness and has a strong texture or preferred grain

orientation. In Fig. 8.2, the strength and flaw size relationship is shown for sample sets A.III and B.II with the samples broken on the substrate surface shown in black. The failure origin could be found in only one of the two samples broken on the substrate side in sample set A.III. However, this one sample is the highest strength sample in the set. In sample set B.II, nearly all of the samples broken on the substrate surface have a higher strength than those broken on the growth surface for similar flaw size.

In Fig. 8.3, the fracture toughness, K_{Ic} , and flaw size relationship is shown for sample sets A.III and B.II with the samples broken on the substrate surface shown in black. For both sample sets K_{Ic} was larger for nearly all of the samples for similar flaw size.

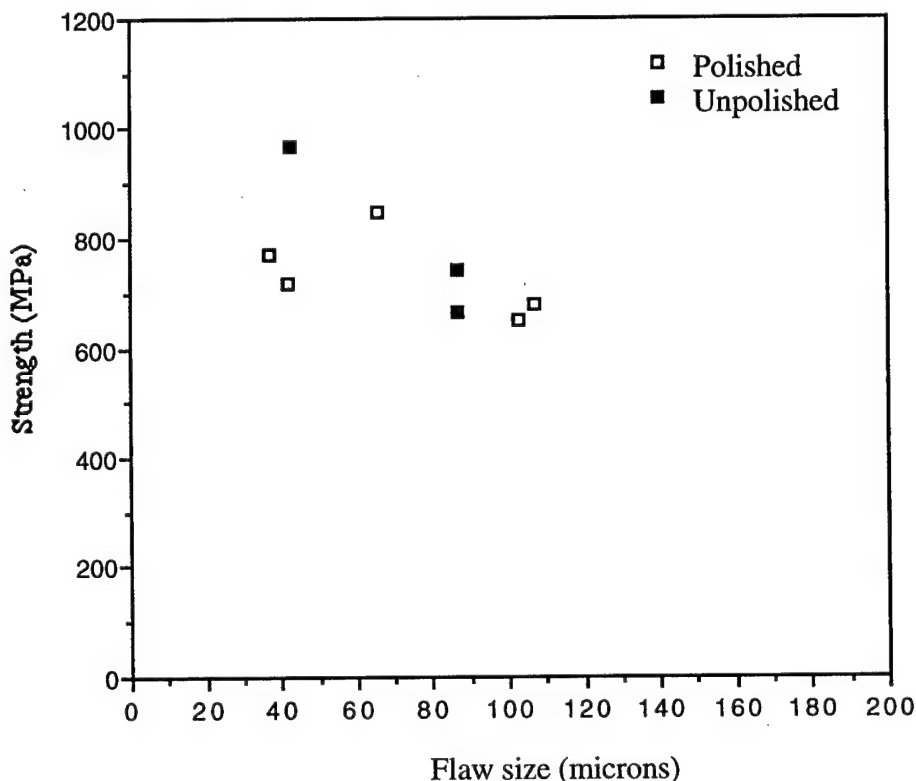


Fig. 8.1 Strength and flaw size relationship for sample set A.II which contained both polished and unpolished samples.

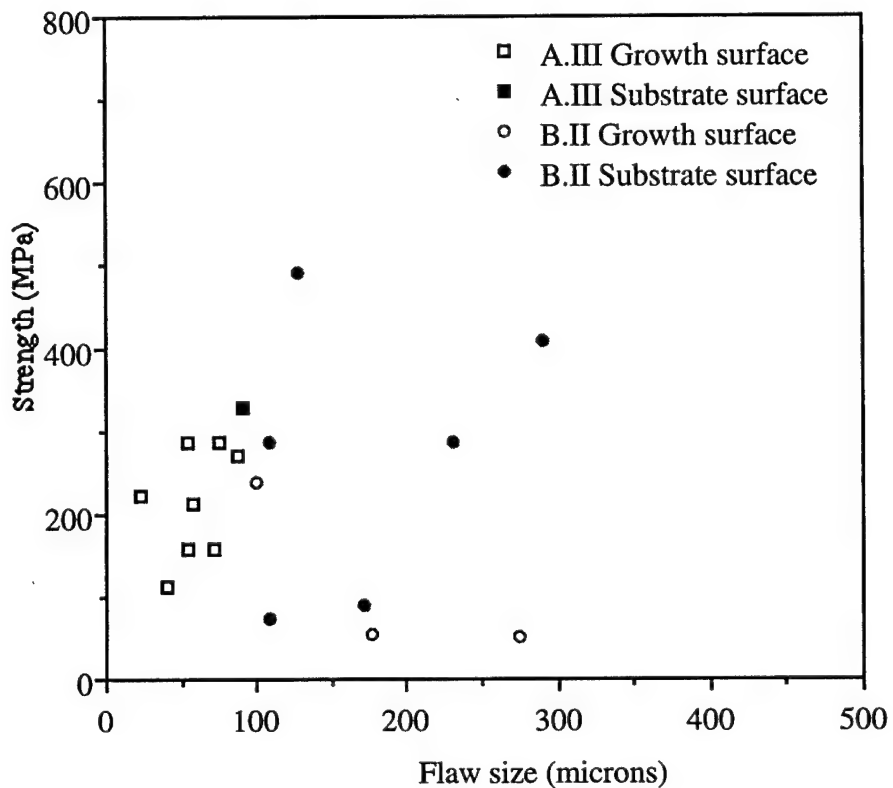


Fig. 8.2 Strength and flaw size relationship for sample sets A.III and B.II. Samples which were fractured on the substrate surface are shown in black.

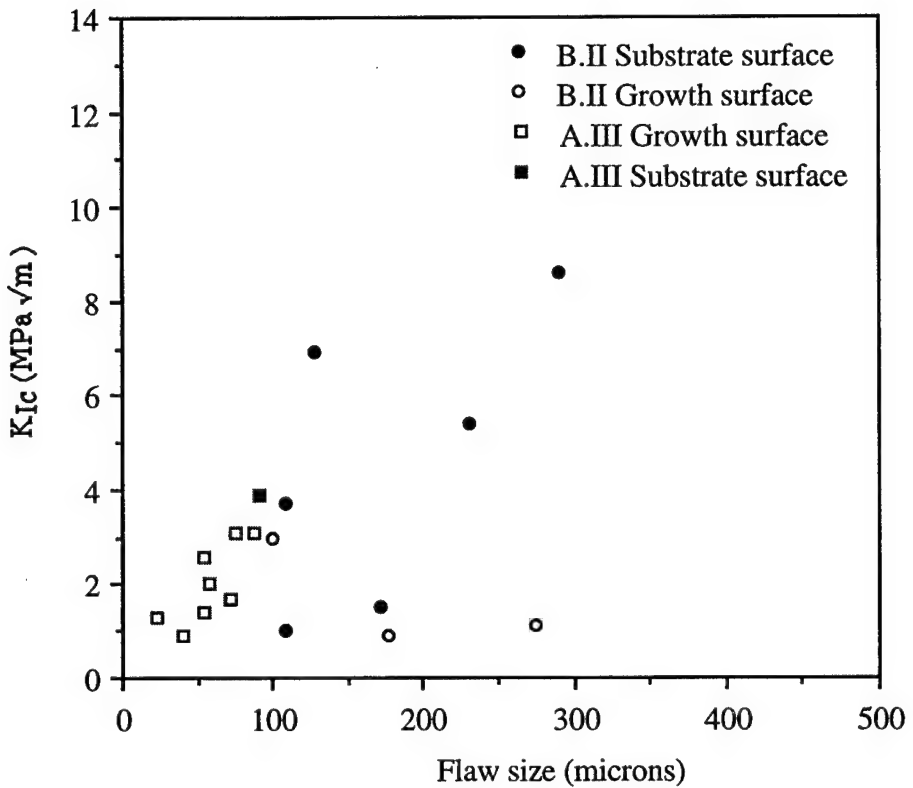


Fig. 8.3 K_{Ic} and flaw size relationship for sample sets A.III and B.II. Samples which were fractured on the substrate surface are shown in black.

CHAPTER 9 MAXIMUM STRESS AS A MEASURE OF STRENGTH

Motivation

Previously, it was implied by observation that the maximum stress of a sample may be a measure of the strength of the sample (defined here as the local stress in the area of the failure origin at failure). The maximum stress data were shown to illustrate various relationships between the strength, critical flaw size, sample thickness, and fracture toughness, K_{Ic} , in situations where the amount of strength data was insufficient to show the trend of the data.

Fracture studies on materials such as polycrystalline CVD diamond require considerable time, effort, and expertise to locate and measure the failure origins. If the investigation is for the purpose of finding the processing variables which give the highest strength, use of the maximum stress would considerably simplify the analysis when ball-on-ring loading is used. In the case of the present study, failure origins could not be found in over two-thirds of the samples. However, maximum stress data from the entire sample set were available without the need to perform failure analysis.

Background

Johnson and Tucker^[44] demonstrated that the failure origin positions of samples loaded to failure in a mathematically defined stress gradient had a distribution which could be used to estimate the parameters of the strength distribution. Johnson and Tucker used randomly generated failure origin positions in a computer simulation to statistically model

the fracture data collection process. The simulation resulted in a Weibull distribution of failure origin positions which was characterized by the same Weibull modulus, m, as the strength distribution.

Johnson and Tucker used three point bending of circular rods as an experimental example. The loading arrangement of the present study (ball-on-ring) is similar in that the stress distribution has a maximum in the center and falls off as a gradient.

The distribution of strengths for a set of identical samples of a given brittle material is described by the Weibull distribution function^[45]:

$$P_f(V) = 1 - \exp\left[-\left(\frac{\sigma}{\sigma_0}\right)^m\right] \quad (9.1)$$

where $P_f(V_0)$ is the cumulative probability of failure. V_0 , σ_0 , and m are constants. The constant m is the Weibull modulus and describes the variability of the strength distribution. A lower value of m such as 5-15, is the range for typical engineering ceramics and indicates the variability or range of strengths is large.^[45] A high value of m such as 100 indicates low variability and the strength may be considered closer to a single well-defined value.^[45]

Taking the natural logarithm of eqn 9.1 twice gives

$$\ln \ln \left[\frac{1}{1 - P_f} \right] = m \ln \sigma - m \ln \sigma_0 \quad (9.2)$$

The Weibull modulus, m, of the distribution is then the slope of the plot of the left side of eqn. 9.2 vs. $\ln \sigma$.

The goal of the Texas Instruments study (set A.I) was to develop processing conditions which maximized strength. For each of the twenty different processing conditions, a set of nine or ten samples were made. Failure origins could be found in only two or three of the nine or ten samples of each processing set. The strength information for

each set is therefore limited and the strength statistics would be greatly improved if the maximum stress data could be used as a measure of strength.

Justification

In Fig. 9.1, the maximum stress is plotted as a function of the corresponding strength for the combined data. The data show a trend that resembles a linear relationship between the maximum stress and strength. The question arises as to whether the strength as defined here (i.e., local stress in the area of the failure origin at failure) has a distribution equivalent to that of the maximum stress data. The relationship shown in Fig. 9.1 indicates that this could be so. Additional verification for this can be made by comparing the Weibull modulus, m , for both the strength and the maximum stress for a single set of similarly processed samples. For one processing set of the Texas Instruments study (set A.I, process 2) as many failure origins as possible were found for the set (seven of the ten samples) and the Weibull modulus, m , calculated for both the maximum stresses and the strengths (Fig 9.2). In addition, the same procedure was carried out for data set A.II (Fig. 9.3) as those samples were all processed under similar conditions.

The log-log Weibull plots used to calculate the Weibull modulus, m , for the strength and maximum stress for the two different sample sets are shown in Figs. 9.2 and 9.3. In Fig. 9.2, the value of m for the strengths is 5.7, and the value for the maximum stresses, 3.6. In Fig. 9.3, the value of m for the strengths is 2.22, and the value for the maximum stresses, 3.3. The m values between the strengths and maximum stresses appear to correspond moderately. The m values for both cases are rather small, indicating a large amount of variability in the data and at these low m values a difference of 1 or 2 is not significant. This study indicates that the maximum stress value can be used to evaluate processing conditions for the effect of the CVD process of diamond on final strength.

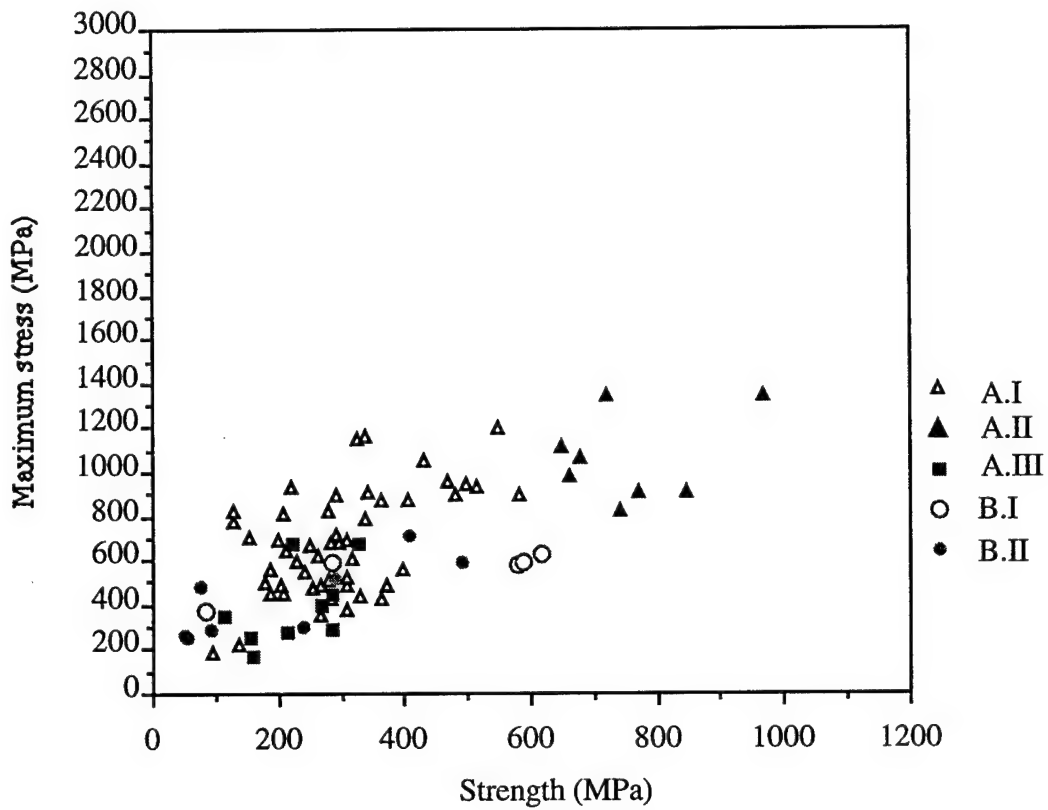


Fig. 9.1 Plot of maximum stress (stress at center of disk at failure) vs. strength (stress at failure origin at failure) for the combined data.

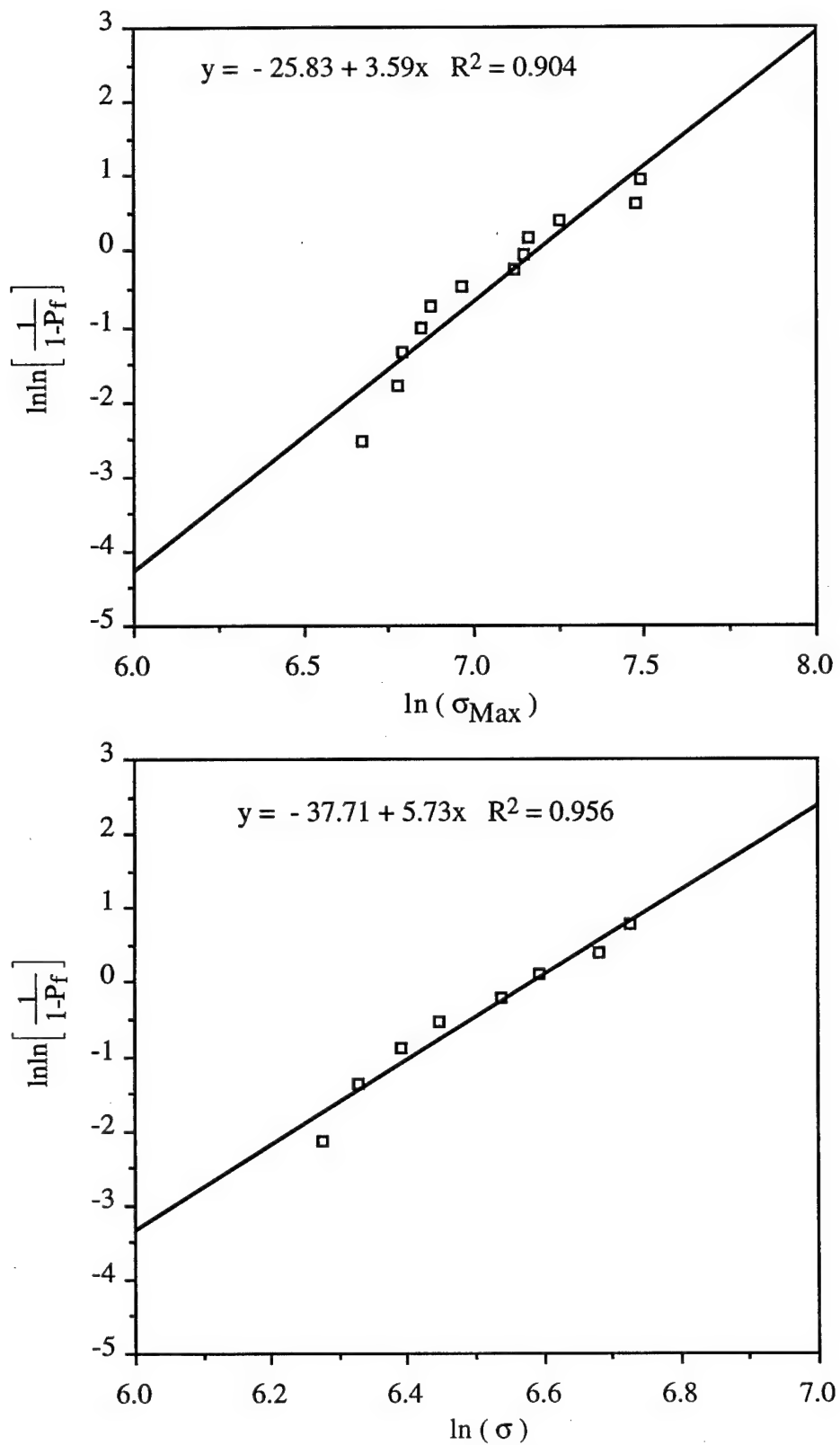


Fig. 9.2 Log-log Weibull maximum stress plot for sample set A.II (top). Log-log Weibull strengths plot for sample set A.II (bottom).

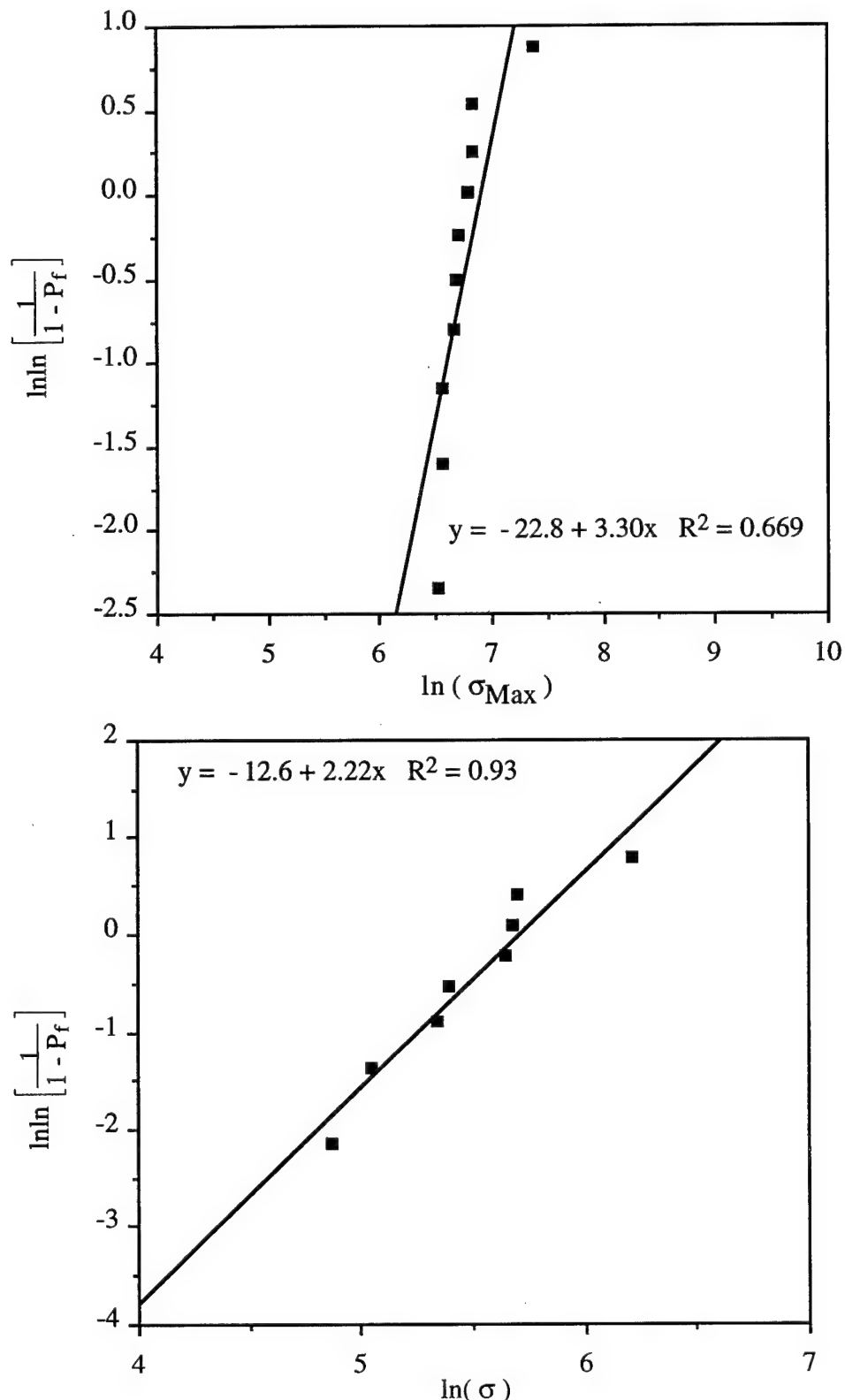


Fig. 9.3 Log-log Weibull strength plot for process 2 of set A.I of the Texas Instruments study (top). Log-log Weibull maximum stress plot for process 2 of set A.I of the Texas Instruments study (bottom).

CHAPTER 10

MEASUREMENT OF RESIDUAL STRESSES IN CVD DIAMOND DEPOSITED ON SILICON

Introduction

Residual stresses in CVD diamond coatings due to intrinsic stresses and thermal expansion mismatch can cause poor substrate adhesion. If these stresses reach the magnitude of the tensile fracture stress of CVD diamond,^[1,3] cracking of the coating can occur. Due to the presence of intrinsic stresses, i.e., stresses resulting from the growth process, the residual stresses can not be predicted on the basis of thermal expansion mismatch alone. Thus, the knowledge of residual stresses in CVD diamond coatings has become critical towards the goal of general application on a variety of growth substrates.

Windischmann et al.^[8] demonstrated the dependence of processing conditions on the residual stress in CVD diamond deposited on Silicon. However, the dependence of stress on coating thickness and temperature has received little attention and hence is the primary focus of this study.

The coefficient of thermal expansion (CTE) plots of diamond and Silicon vs. temperature are shown in Fig. 10.1. The plots contain a crossover point at about 750°C. The CTE mismatch stress can be calculated from the expression^[8]

$$\sigma_{\text{Dia}} = \frac{E_{\text{Dia}}}{1 - v_{\text{Dia}}} \int_{T_0}^T (\alpha_{\text{Si}} - \alpha_{\text{Dia}}) dT \quad (10.1)$$

where T_0 is the deposition temperature (850°C in this study), T the temperature at which the stress is evaluated, and α ^[46] the coefficient of thermal expansion. Calculation of the CTE stress at room temperature (20°C) for coating deposition at 850°C using eqn. 10.1 yields -479 MPa , where the minus sign signifies compressive stress. Therefore, based on CTE mismatch alone, the expected residual stress in the diamond coatings examined in this study is -479 MPa .

Experimental Details

The silicon substrates were preseeded with diamond nuclei before diamond deposition by hot filament CVD. A methanol slurry containing $0.25\text{-}0.5 \mu\text{m}$ diamond powder was gently applied with a cotton swab to avoid producing scratches on the substrate. Diamond films were then deposited by hot-filament chemical vapor deposition.

The HFCVD chamber was constructed out of a six inch diameter, six way stainless steel cross. Five of the ports served as feedthroughs for the power inputs, gas flow tubes, pressure gauge, vacuum pump, and thermocouple. A quartz bell jar sat on top of the sixth port. The filament and substrate were suspended up into the bell jar to eliminate any contamination from the stainless steel cross. The filament was constructed of a 0.5 mm tungsten wire coiled in a 1 cm diameter with seven turns. The temperature of the filament was 2200°C and was measured by an optical pyrometer. The substrates placed 20mm above the filament were heated solely by the filament to 850°C as measured by a K-type thermocouple held on the backside of the substrate. The gases were injected into the system directly below the filament. The total gas flow rate and total pressure were 150 sccm and 40 Torr respectively. The chemistry of the gases was 0.75% methane in balance hydrogen. Under these conditions growth rates of $2\mu\text{m}/\text{hr}$ were achieved. The deposition conditions are summarized in Table 10.1.

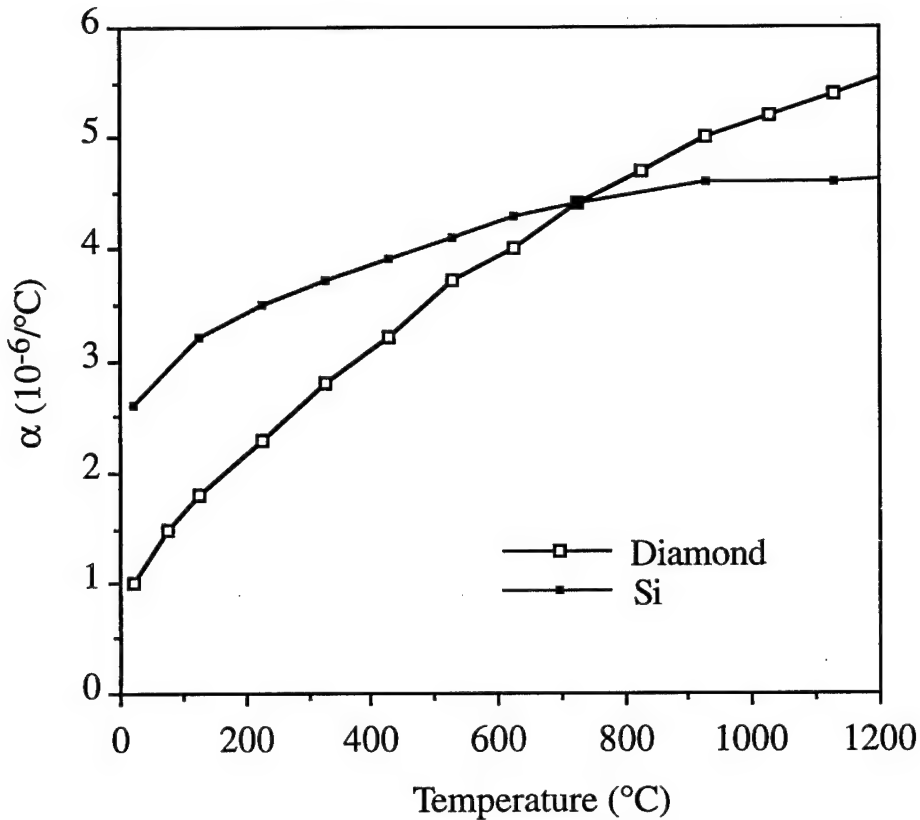


Fig. 10.1. Thermal expansion vs. temperature curves of diamond and Silicon (after Slack and Bartram,[46])

Table 10.1. Deposition conditions

Filament Temperature	2200 $^{\circ}\text{C}$
Substrate Temperature	850 $^{\circ}\text{C}$
Filament-Substrate Distance	20 mm
System Pressure	20 Torr
Gas Flow Rate	150 sccm
Gas Chemistry	0.75% CH ₄ , 99.25% H ₂
Growth Rate	2 $\mu\text{m/hr}$

X-ray Stress Measurement Conditions

A Scintag PTS Residual Stress Goniometer with a rotating anode X-ray source was used to make the X-ray residual stress measurements with a beam spot size of approximately 3mm in diameter. Specimen tilts were made perpendicular to the diffraction plane (so called Chi-tilt method) To verify alignment of the diffractometer, calibration was made to NIST 640b standard silicon powder. Measurements of several peaks of the NIST standard were made at each of the tilt angles (ϕ and χ) used to make the stress measurements. The difference between the measured peak positions and the tabulated standard values was less than $0.01^\circ 2\theta$ for all the tilts thus ensuring the reliability of measurements at all tilt angles. Only the diamond phase was measured for stress. A diagram of the coordinate systems used on the different laminate surfaces is shown in Fig. 10.2.

The strain, $\varepsilon_{\phi\chi}$, measured at an orientation defined by the angles ϕ and χ (Fig. 10.2) is related to the stresses in the sample, σ_{ij} , by eqn 10.2.^[47] Figure 10.2 is adapted from Iancu et al.^[48]

$$\begin{aligned} \varepsilon_{\phi\chi} = \frac{d_{\phi\chi} - d_0}{d_0} &= \frac{1+v_{hkl}}{E_{hkl}} \{ \sigma_{11}\cos^2\phi + \sigma_{12}\sin2\phi + \sigma_{22}\sin^2\phi - \sigma_{33} \} \sin^2\chi \\ &+ \frac{1+v_{hkl}}{E_{hkl}} \sigma_{33} - \frac{v_{hkl}}{E_{hkl}} (\sigma_{11} + \sigma_{22} + \sigma_{33}) \\ &+ \frac{1+v_{hkl}}{E_{hkl}} (\sigma_{13}\cos\phi + \sigma_{23}\sin\phi) \sin2\chi \end{aligned} \quad (10.2)$$

where E_{hkl} and v_{hkl} are Young's modulus and Poisson's ratio for the given hkl reflection used, ϕ and χ the tilt angles, $d_{\phi\chi}$ the d-spacing measured at the orientation defined by the angles ϕ and χ , and d_0 the unstressed d-spacing.

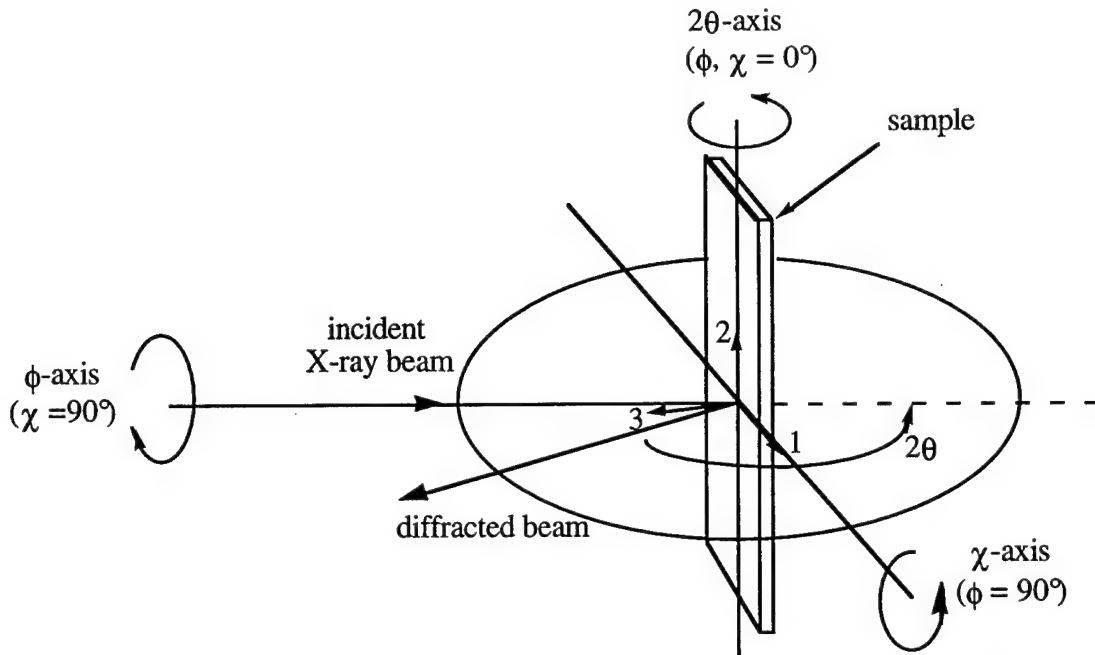


Fig. 10.2. Diagram defining sample coordinate system and angles ϕ , χ and 2θ . After Iancu et al.[48]

The stresses were calculated from eqn. 10.2. by the method of Winholz and Cohen.[49] In the method of Winholz and Cohen, the sample stresses are recognized as being linearly related to the measured strain. If the strain is measured in at least six independent orientations, eqn. 10.2. can be solved for the stresses (i.e., by solving six equations with six unknowns). The accuracy is improved by measuring more than six strains and employing a least squares fit of the data. The method is described in detail in references 49-50. The least squares fitting procedure used was incorporated into a computer program by Abuhasan.[50]

The X-ray procedures used followed that of a previous study reported elsewhere.[51] Cr K_α radiation was used instead of the usual Cu K_α to decrease the penetration depth and hence obtain more scattered intensity from the diamond coating. The mean depth of penetration (the depth below the surface above which half the diffracted X-ray intensity originates) varies with χ -tilt angle.[47,52] For the range of χ -tilts employed in

this study (0° - 55.0°) the mean penetration depth varied from 96-55 μm , respectively. The X-ray penetration depth exceeded the thickness (2.5-15 μm) of all the samples investigated.

Zero-Stress Reference

The accuracy of the stress measurements is highly dependent on the stress free lattice spacing (d_0), therefore the stress free lattice spacing must be measured to the highest accuracy possible. In order to obtain the unstressed lattice spacing, a diamond coating deposited on Si using identical conditions (Table 10.1) was removed from the substrate by etching away the substrate with 3:1 mix of NO_3 and HCl . The free standing coating was then lightly ground in mortar and pestle. The (220) X-ray diffraction peak was extremely broad with a full-width-at-half-max (fwhm) over $1.2^\circ 2\theta$ (compare with a fwhm of $0.280^\circ 2\theta$ for NIST 640b standard silicon powder). The extreme broadening of the peak made it impossible to obtain an accurate (220) peak position necessary for stress measurement. The extreme broadening was due to either internal strains induced by the grinding, small particle size, or the acid etch technique used to remove the coating from the substrate. The composition variations and the possible presence of lattice deformations in the industrial diamond powder eliminated that source of obtaining the d_0 value as well.

The d_0 value was obtained via the method developed by Hauk et al.^[53] This method uses the actual data of the stress method to determine d_0 .^[47] Through the use of the Hauk method a slightly different unstressed lattice spacing was obtained for each sample (Table 10.2). This method assumes the plane stress condition (a reasonable assumption for a thin coating) and eliminates errors in d_0 due to sample displacement errors.

Curvature Stress Method

In order to verify the results of the X-ray diffraction measurements the stresses in several of the samples were measured using a curvature technique. The curvatures were measured by mapping the rise of the sample above a glass slide in a microscope.

Table 10.2 X-ray and Conditions and Physical Properties.

Reflection used	Diamond (220)
Radiation used	Cr K _α 0.22897nm
Young's modulus, E	1141 GPa ^[2]
Poisson's ratio, v	0.07 ^[2]
Thermal expansion	see Fig. 10.3
Unstressed lattice spacings (d ₀)	
Sample 1	0.12606 nm, (130.513° 2θ)
Sample 2	0.12606 nm, (130.510° 2θ)
Sample 3	0.12606 nm, (130.508° 2θ)
Sample 4	0.12606 nm, (130.501° 2θ)
Sample 5	0.12607 nm, (130.490° 2θ)
Sample 6	0.12606 nm, (130.503° 2θ)
Sample 7	0.12606 nm, (130.516° 2θ)
2θ (220) JCPDS-ICDD card 6-675	130.431° 2θ
χ-tilts (see Fig. 2. for definition)	0°, ±28.2, ±42.0, ±55.0
φ-tilts (see Fig. 2. for definition)	0°, 45°, 90°

To obtain a measurable curvature, the silicon beams had to be reduced in thickness by grinding with 600 grit silicon carbide paper to a thickness of less than 200μm. In a separate experiment, the grinding procedure used to reduce the thickness was performed on uncoated Si beams and was found to cause a curvature of the order of that which would be expected due to the tensile residual stresses of the coating. This curvature was due to grinding residual stresses induced on a thin layer of the grinding surface. The Si beams were then ground through progressively smaller grit sizes to a 0.05 μm diamond polish and the curvature successfully removed. This occurred by progressive removal of the grinding

damaged surface layer. By using this modified procedure, the curvature occurring after thickness reduction by grinding could then be attributed to the diamond/Si system stress alone.

The σ_{11} component in the coatings were calculated from the radius of curvature through the expression of Brenner and Senderoff^[54] (modified by replacement of E with the biaxial modulus, E / (1-v)):

$$\sigma_{11} = \frac{E_{Dia}}{1 - v_{Dia}} \frac{t_{Si} (t_{Si} + t_{Dia})}{6Rt_{Dia}} - \left[\frac{E_{Dia}}{1 - v_{Dia}} - \frac{E_{Si}}{1 - v_{Si}} \right] \frac{t_{Si}^3}{6Rt_{Dia}(t_{Si} + t_{Dia})} \quad (10.3)$$

where t_{Si} , t_{Dia} , E_{Dia} , E_{Si} , v_{Dia} , v_{Si} , and R are the thickness of the Si substrate, the thickness of the diamond coating, Young's modulus of the diamond coating, Young's modulus of the Si substrate, Poisson's ratio of the diamond coating, Poisson's ratio of the Si substrate, and the radius of curvature of the strip, respectively.

The curvature method used gave only a rough estimate of the coating stresses (± 100 MPa). However, the data were useful in confirming the sign (tensile) and general order of magnitude of the stresses.

The stress as function of temperature of one of the samples was measured after the Si substrate thickness was reduced to 60 μm through the grinding and polishing procedure described previously. The curvature measurements were made with greater precision than those used to verify the X-ray measurements and the corresponding stresses obtained to a precision of ± 75 MPa.

The Si/diamond strip (sample 5) was heated in a nitrogen atmosphere in a tube furnace and the curvature observed through a window in the door of the furnace with a traveling microscope. The microscope had a magnification of 25X at a distance of 20cm and had fine position control of $\pm 10\mu\text{m}$ in the z-direction (the direction in which the rise of the sample above the level surface was measured) and $\pm 50\mu\text{m}$ in the direction perpendicular to the z-direction (the direction along the length of the sample). A diagram of the

measurement system used is shown in Fig. 10.3. The curvature of the strip was measured as a function of temperature from 200°C to 800°C.

The CTE mismatch stress and experimentally measured stress are plotted as a function of temperature in Fig. 10.4. The two curves are nearly identical except that the experimental plot is displaced upward by a constant from the CTE plot. The difference between the CTE mismatch stress and the experimentally measured stress is temperature independent. This difference is the intrinsic stress. At the deposition temperature (850°C), the experimental stress should be zero, however, it is 520 ± 75 MPa. The intrinsic stress is then 520 ± 75 MPa. At room temperature the CTE mismatch stress is -479 MPa, this is the stress which would be predicted based on CTE mismatch alone.

Qualitative Analysis of Diffraction Patterns

The diffraction peak used for the stress measurement, ((220) diamond at approximately $130.50^\circ 2\theta$ with Cr K α radiation) exhibited a highly broadened fwhm in relation to that of NIST 640B standard silicon powder used in the goniometer alignment. The NIST standard silicon powder has a highly uniform particle size and is free of strain and defect induced broadening. The fwhm of the (220) diamond peak used in the stress measurements was on average about $0.70^\circ 2\theta$ and that of the silicon standard (at $133.540^\circ 2\theta$, near that of the (220) diamond peak) was about $0.280^\circ 2\theta$. The broadening is most likely due to internal micro-strains equilibrated over volumes of the order of a few grains within the material. Broadening of X-ray diffraction peaks is due to either non-uniform strains or the small particle effect which occurs when the particle size is less than about 0.1 μm .^[55] Several studies on X-ray diffraction of CVD diamond have also reported this strain induced broadening.^[7,56,57]

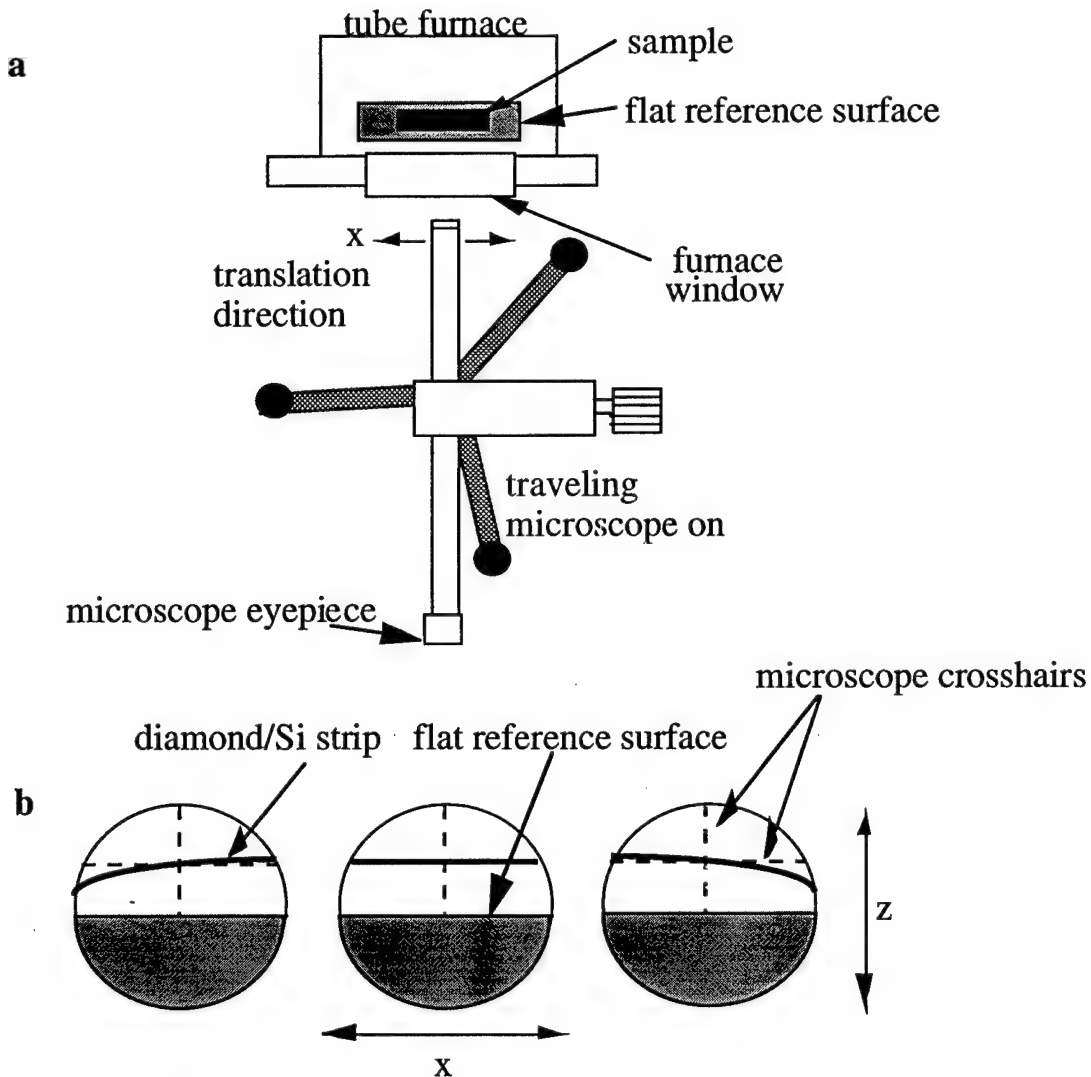


Fig. 10.3. Schematic of the instrumentation used to measure the curvature as a function of temperature of a diamond coated silicon strip. In a., the strip is observed through the window of a tube furnace with a traveling microscope at a magnification of 25X. In b., the curvature is obtained at each temperature by measuring the height of the strip (z-direction) above the flat reference surface at different points along the length of the strip (x-direction). Hashed lines are microscope crosshairs. The three different microscope views shown represent the view of the center of the strip (highest point of elevation of strip above reference surface) and near the left and right ends.

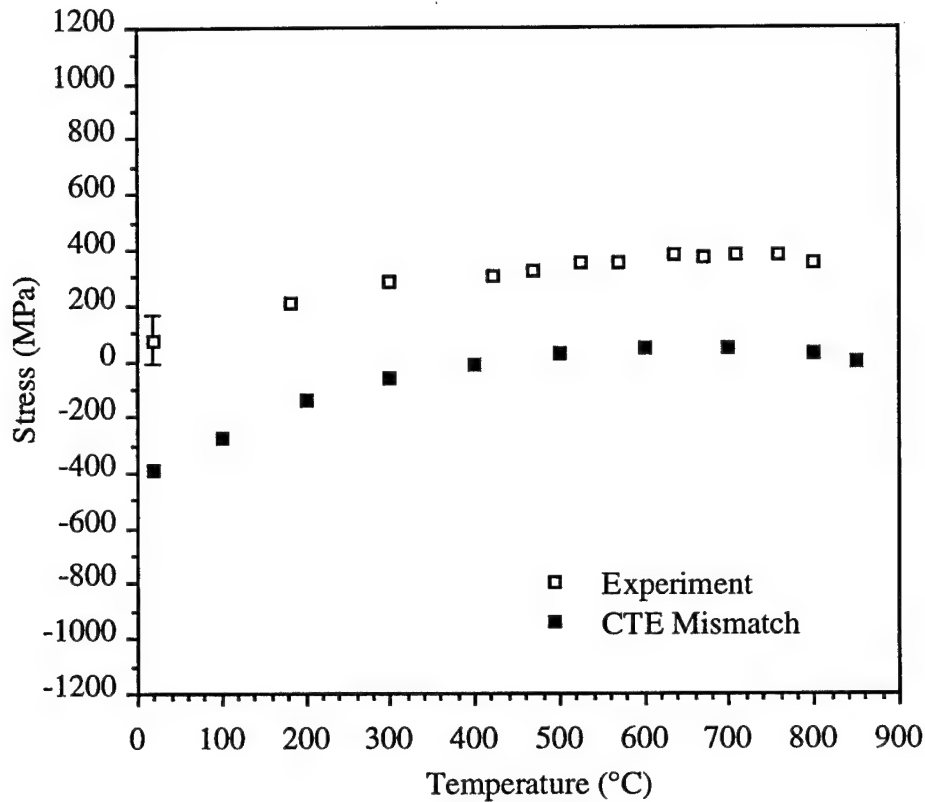


Fig 10.4. CTE mismatch stress and the experimentally measured stress vs. temperature.

Pole Figures

If there is an absence of texture in the polycrystalline material, the assumption of material isotropy can be made and the isotropic elastic constants of the material can be used as a good approximation to the X-ray elastic constants.

The texture is best analyzed with a pole figure of the material. Pole figures were measured in the back reflection Schulz mode^[58] and corrected for the background. The defocusing and absorption correction was done experimentally using a diamond powder with a thickness of several microns (in the range of the film thickness variation). The intensity pole figures clearly show a near random grain orientation, with the exception of an occasional spike due to diffraction from a single large grain.

Growth of thick CVD coatings results in a strong fiber texture due to competitive grain growth.^[59] However, at the beginning of film growth the grain structure is randomly oriented.^[59] It is for this reason that the pole figures show near random grain orientation.

Stress vs. Coating Thickness

A plot of the in-plane stresses (σ_{11} and σ_{22} , defined in Fig 10.5) for the coating versus coating thickness (Fig. 10.6) shows a decrease in stress (less tensile) with increase in thickness. The σ_{11} and σ_{22} values lie along a vertical line for each sample thickness. Sample 3 (3.6 μm coating thickness) appears to be anomalous to this relationship. No apparent cause could be found for the anomalous behavior of this sample.

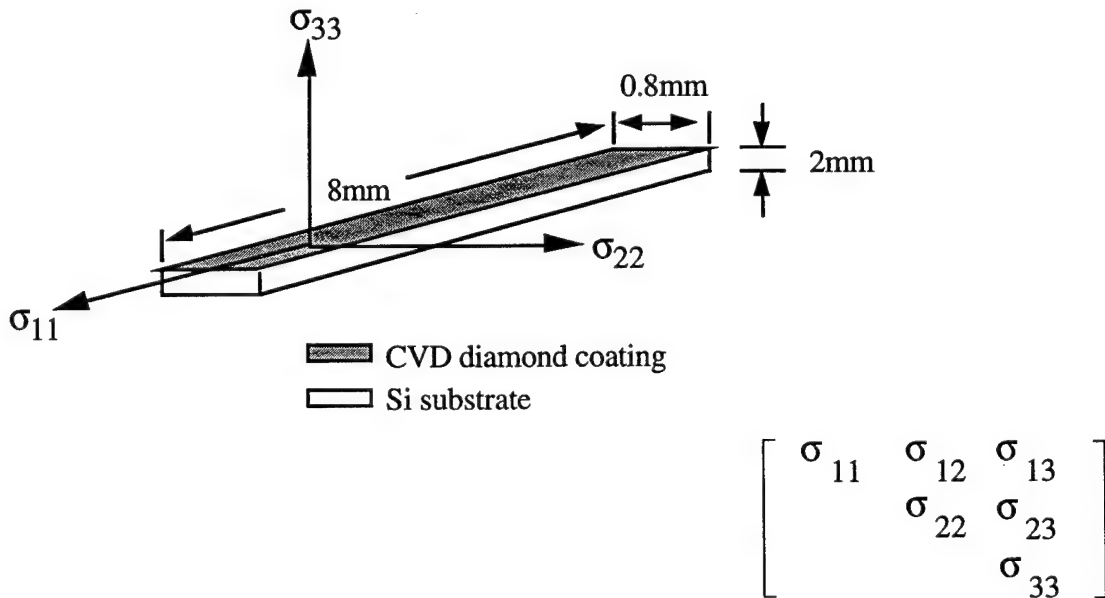


Fig. 10.5 Coordinate system used to describe the stresses in the diamond coatings. At bottom right is the stress tensor, note that σ_{11} and σ_{22} are the two in-plane components, and σ_{33} is in the direction perpendicular to the plane of the coating.

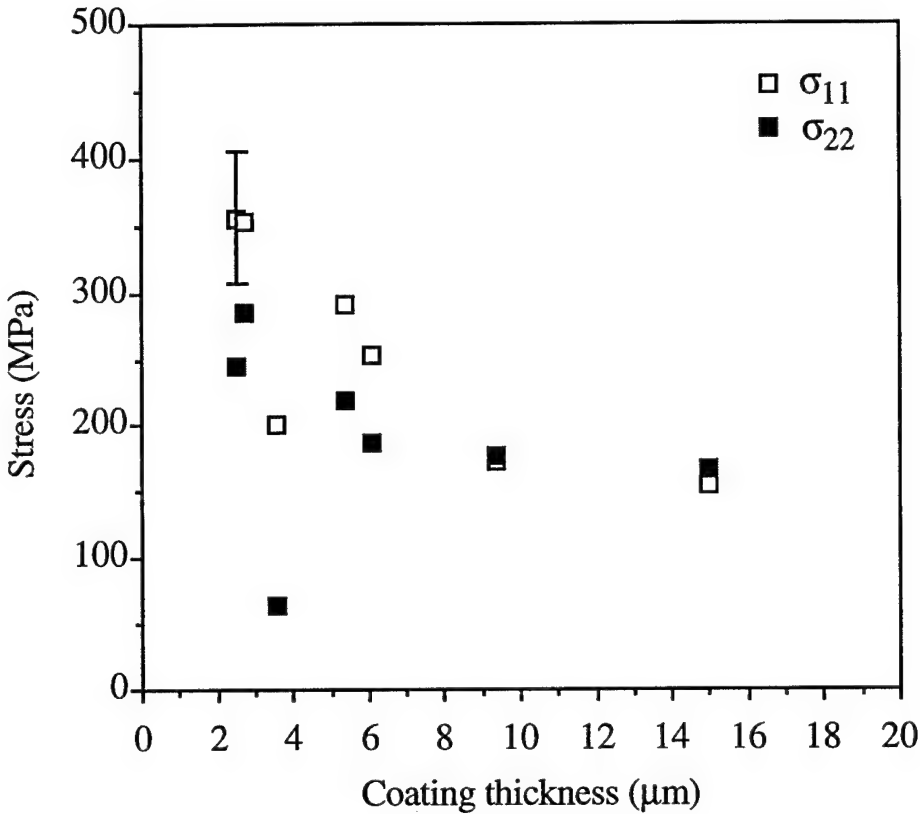


Fig. 10.6. The in-plane stress components (σ_{11} and σ_{22}) as a function of diamond coating thickness. The σ_{11} and σ_{22} values for each sample thickness lie along the same vertical line. Both σ_{11} and σ_{22} appear to decrease (less tensile) with increase of coating thickness. Sample 3 ($3.6\mu\text{m}$ coating thickness) is anomalous to this trend.

Analysis of Coating Stresses

The results of the X-ray residual stress measurements and curvature residual stress measurements are shown in Table 10.3. Looking at the X-ray stress matrices in Table 10.3, intuitively, the σ_{33} stress component should be zero within the error of the measurement ($\pm 50\text{ MPa}$). This is due to the absence of balancing forces perpendicular to the plane of the coating, hence, σ_{33} must vanish at the surface but can exist as a gradient.^[60] All of the samples except sample 7 have a σ_{33} stress component well below the measurement error ($\pm 50\text{ MPa}$). Sample 7 has a σ_{33} stress component (68 MPa)

Table 10.3 Coating residual stresses.

Sample	Coating Thickness (μm) ± 0.1	X-ray Triaxial Residual Stress ($\pm 50 \text{ MPa}$)			σ_{11} Curvature Method Stress ($\pm 100 \text{ MPa}$)
		355	-112 244	1 -36 31	
1	2.5	[355	-112 244	1 -36 31]	Not Measured
2	2.7	[353	-83 285	22 41 4]	265
3	3.6	[200	99 65	-17 21 15]	165
4	5.4	[291	-26 219	-44 -41 44]	457
5	6.1	[254	-25 186	17 -3 2]	245
6	9.4	[173	-43 176	-60 -52 -18]	135
7	15.0	[155	45 166	-5 -3 68]	276 ± 100

only slightly larger than the measurement error. For this same reason the shear components, σ_{13} and σ_{23} , which are shears in planes perpendicular to the plane of the coating surface, should be zero within the measurement error also. All of the samples satisfy this except sample 6 which has σ_{13} and σ_{23} components of -60 MPa and -52 MPa

respectively, but this is only slightly larger than the measurement error. In this way, the σ_{i3} ($i=1, 2, 3$) give a good estimate of the measurement error.

All of the samples except sample 3 ($3.6\mu\text{m}$ coating thickness) exhibit a near-biaxial stress state in the plane of the coating, i.e., σ_{11} and σ_{22} are nearly equal in magnitude. The variation of the in-plane stress components can be caused by the preferred directionality of the deposition conditions. The CVD experimental set-up provided for relatively homogeneous deposition, with no preferred direction.

The σ_{12} shear component which lies in the plane of the coating is a measure of how far off the σ_{11} and σ_{22} components are from the principal stress directions in the plane of the coating. For samples 4-7, σ_{12} is below the measurement error ($\pm 50\text{ MPa}$). In these samples, the σ_{11} and σ_{22} are biaxial ($\sigma_{11} = \sigma_{22}$) within the measurement error.

Comparison of Results with Other Studies

Using a vibrating membrane technique, Berry et al.^[6] found the room temperature stress in CVD diamond coatings deposited on silicon at 850°C to be in the range $10\text{-}140\text{ MPa}$ (tensile), with a growth stress (intrinsic stress) of about 500 MPa (tensile). Using a curvature method, Baglio et al.^[7] obtained room temperature stresses in the range $4\text{-}326\text{ MPa}$ (tensile) with corresponding intrinsic stresses in the range $465\text{-}730\text{ MPa}$ for the diamond/Si system with deposition temperatures in the range $775\text{-}950^\circ\text{C}$. Also using a curvature technique, Windischmann et al.^[8] obtained a value of 200 MPa (tensile) for the diamond/Si system coatings deposited at 850°C . However, the value used for the CTE stress at room temperature, -220 MPa , is much lower than calculated here, -479 MPa . This discrepancy was also noted in Baglio et al.,^[7] and the cause is unclear. Using the CTE stress values calculated here gives an intrinsic stress of 679 MPa (tensile).

Review of Results

Absence of preferred orientation as verified by the intensity pole figures justified the use of polycrystalline elastic constants in the X-ray diffraction method. All of the triaxial X-ray coating stress matrices except that for sample 3 ($3.6\mu\text{m}$ coating thickness) exhibit a near-biaxial stress state in the plane of the coating, i.e., σ_{11} and σ_{22} are nearly equal in magnitude. The in-plane residual stress components (σ_{11} and σ_{22}) were found to decrease (become less tensile) with increase in thickness.

The stresses obtained by the X-ray technique were verified through the use of a curvature technique. To obtain a measurable curvature with the curvature technique, the silicon substrate had to be reduced in thickness by grinding. The grinding procedure caused a curvature of the order (and of the same sign) as that which would be expected due to the tensile residual stresses within coating. A procedure was developed to remove the grinding damaged layer by the use of progressively finer grinding to a fine polish resulting in the elimination of the grinding curvature.

The expected CTE mismatch stress in the coating was calculated to be -479 MPa. However, the stresses measured by the X-ray technique are in the range 65-355 MPa. The difference between the predicted CTE mismatch stress and measured stresses is the so-called intrinsic or growth stress. The residual stress was measured as a function of temperature yielded an intrinsic stress of 520 ± 75 MPa. The intrinsic stress was found to be relatively temperature independent. Several other studies yielded results for the measured and intrinsic stress of similar magnitude and sign to the results of this study.

CHAPTER 11 CONCLUSIONS

Fracture Measurements

One of the most important outcomes of this study was the utilization of the methods of fracture surface analysis to gain insight into the cause of the failure initiating flaws. This in turn may be of use in the future in the adjustment of processing conditions towards development of CVD diamond which is closer to the fracture toughness levels predicted.

This study shows the results of many different processing conditions and sources. The fracture toughness values obtained here varied significantly between each source and in two cases (sample set B.I and B.II) within a particular source. From this study it is clear that the fracture toughness and perhaps, more generally, mechanical properties in diamond are strongly dependent on processing conditions. The combined data from the different sources showed that processing conditions could lead to widely varying fracture toughness values.

A result of the study which appears to be independent of processing is the critical flaw size and sample thickness relationship (Fig. 7.3) for the combined data. Below a sample thickness of about 400 μm , the critical flaw size is first limited by the thickness and increases linearly with thickness. Above a thickness of about 400 μm , a constant flaw size is reached which is independent of sample thickness.

Several studies in the area of strength and fracture toughness of polycrystalline CVD diamond attempted to characterize the material through the measurement of strength alone. It is difficult (if not impossible) to use strength as a material property in brittle materials such as polycrystalline CVD diamond for the reason that the strength is controlled

by the size of the failure initiating cracks. Recalling the strength data of the Texas Instruments study (set A.I), the strength was shown to sharply increase with decrease in sample thickness below 150 μm (Fig. 5.5). The corresponding critical fracture toughness, K_{Ic} , showed no real difference in fracture behavior with change in thickness (Fig. 5.10). However, these strength studies were useful in the context of the careful examination of the procedures necessary to obtain the strength values. The carefully designed strength testing procedures used by Valentine et al.^[34] (burst test) likely produced strength data as accurate as (or better than) the present study. However, the results of the Valentine et al. study would have been greatly enhanced with the inclusion of fracture surface analysis on the failed specimens.

The issue of whether fracture is transgrannular or intergrannular was addressed through the use of fractography. The matching halves of representative fracture surfaces were shown to qualitatively argue that the fracture was mostly transgrannular. In addition, the cleavage marks and river marks which comprise most of the topography of the fracture surface were identified as features resulting from transgrannular fracture.

Residual Stress Measurement

The residual stresses obtained by the X-ray technique were verified through the use of a curvature technique. To obtain a measurable curvature with the curvature technique, the silicon substrate had to be reduced in thickness by grinding. The grinding procedure caused a curvature of the order (and of the same sign) as that which would be expected due to the tensile residual stresses within the coating. A procedure was developed to remove the grinding damaged layer through the use of progressively finer grinding to a fine polish resulting in the elimination of the grinding curvature.

Absence of preferred orientation as verified by the intensity pole figures justified the use of polycrystalline elastic constants in the X-ray diffraction method. All of the triaxial

X-ray coating stress matrices except that for sample 3 ($3.6\mu\text{m}$ coating thickness) exhibit a near-biaxial stress state in the plane of the coating, i.e., σ_{11} and σ_{22} are nearly equal in magnitude. The In-plane residual stress components (σ_{11} and σ_{22}) were found to decrease (become less tensile) with increase in thickness.

The expected CTE mismatch stress in the coating was calculated to be -479 MPa. However, the stresses measured by the X-ray technique are in the range 65-355 MPa. The difference between the predicted CTE mismatch stress and measured stresses is the so-called intrinsic or growth stress. The residual stress was measured as a function of temperature yielded an intrinsic stress of 520 ± 75 MPa. The intrinsic stress was found to be relatively temperature independent. Several other studies yielded results for the measured and intrinsic stress similar in magnitude and sign to the results of this study.

APPENDIX A BALL-ON-RING LARGE DEFLECTION SOLUTION FOR STRESS

Theoretical Development

This appendix addresses the problem of a thin circular plate with overhang, loaded in the center, that may experience large deflection. The closely related problem of a simply supported centrally loaded circular plate with no overhang and a Poisson's ratio, v , fixed at 0.3 was solved approximately by Timoshenko and Woinowsky-Krieger.^[35] However, the accuracy of the solution, and whether or not the approximation could be used to accurately model the stresses in the loading arrangement used in the present study needed to be addressed. The loading used in this study includes overhang of the disk on the support ring and a Poisson's ratio value ($v = 0.07$) considerably lower than that assumed in the solution of Timoshenko and Woinowsky-Krieger. In the solution of Timoshenko and Woinowsky-Krieger, only the radial and tangential bending stresses at the edge of the plate and the radial and tangential membrane stresses at the center and edge of the plate were considered.

A functional form (with undetermined coefficients) for the displacement and strain of the mid plane of the plate (membrane strain) was assumed and the strain energy method employed to determine the coefficients from which the deflection, bending stresses, and membrane stresses were to be determined. The strain energy method proceeds as follows^[35]:

$$\pi = V + V_1 - F\omega_0 \quad (A.1)$$

where π is the total potential energy, $F\omega_0$ (force times displacement of disk center) the work done by the outside force, V , the strain energy due to bending, and V_1 , the strain energy due to strain of the mid plane of the plate (i.e., strain energy due to membrane strains). A free-body diagram of the centrally loaded disk is shown in Fig. A.1 in which the relevant parameters of the problem are defined.

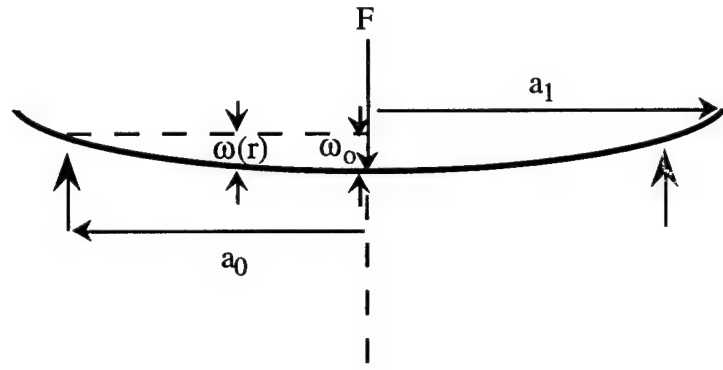


Fig A.1 Free-body diagram of the centrally loaded disk in which the relevant parameters of the problem are defined.

V and V_1 are given by

$$V = \int_0^{2\pi} \int_0^{a_1} \left[\left(\frac{\partial^2 \omega}{\partial r^2} \right) + \frac{1}{r^2} \left(\frac{\partial \omega}{\partial r} \right)^2 + \frac{2v}{r} \left(\frac{\partial \omega}{\partial r} \right) \left(\frac{\partial^2 \omega}{\partial r^2} \right) \right] r dr d\theta \quad (\text{A.2})$$

$$V_1 = \frac{\pi Eh}{1 - v^2} \int_0^{a_1} [\epsilon_r^2 + \epsilon_t^2 + 2v \epsilon_r \epsilon_t] r dr d\theta \quad (\text{A.3})$$

where D is the coefficient of rigidity, ω , the displacement function, a_1 , the plate radius, ϵ_r , the membrane strain, ϵ_θ , the tangential membrane strain; u , the displacement function, E , the Young's modulus, and v , the Poisson's ratio. The coefficient of rigidity, D , is given by

$$D = \frac{Et^2}{12(1-\nu^2)} \quad (A.4)$$

where t is the thickness of the plate. The radial and tangential membrane strains are given by

$$\epsilon_r = u/r \quad (A.5)$$

$$\epsilon_\theta = \frac{\partial u}{\partial r} + \left(\frac{\partial \omega}{\partial r}\right)^2 \quad (A.6)$$

The deflection, ω , and displacement, u , must meet the following boundary conditions:

$$\left(\frac{\partial \omega}{\partial r}\right)_{r=0} = 0 \quad (A.7)$$

$$\omega(a_0) = 0 \quad (A.8)$$

$$u(0) = 0. \quad (A.9)$$

For the problem of a simply supported centrally loaded disk (with overhang) used in this study the following u and ω functions were used:

$$u = c_1 r + c_2 r^2 + c_3 r^3 + c_4 r^4 + \dots \quad (A.10)$$

$$\omega = \omega_0 \left(1 - \frac{r^2}{a_0^2}\right) + \omega_1 r^2 \ln \frac{r}{a_0} \quad (A.11)$$

The ω function chosen above (eqn. A.11) is the small deflection formula (with no overhang) given in Roark et al.[19] with the addition of two undetermined coefficients. The strategy is that if the deflection is moderately large, the deflection will not differ greatly from that given by the small deflection formula and the addition of two undetermined coefficients to the function will further reduce the error.

The coefficients ($\omega_0, \omega_1, c_1, c_2, c_3, \dots, c_i$) are found through the conditions

$$\frac{\partial \pi}{\partial \omega_0} = \frac{\partial \pi}{\partial \omega_1} = \frac{\partial \pi}{\partial c_1} = \frac{\partial \pi}{\partial c_2} = \frac{\partial \pi}{\partial c_3} = \dots = \frac{\partial \pi}{\partial c_i} = 0 \quad (\text{A.13})$$

The software package Mathematica™ was used to numerically calculate the coefficients using eqn. A.1. The computer program is included at the end of this section. The tangential bending stress, σ_t , was calculated from the tangential bending moment, M_t , using

$$\sigma_t = \frac{6 M_t}{h^2} \quad (\text{A.14})$$

$$M_t = -D \left[\frac{1}{r} \left(\frac{\partial \omega}{\partial r} \right) + v \left(\frac{\partial^2 \omega}{\partial r^2} \right) \right] \quad (\text{A.15})$$

The tangential membrane stress was calculated from

$$\sigma_t = \frac{E}{1-v^2} (\epsilon_t + v \epsilon_r) = \frac{E}{1-v^2} \left[\frac{u}{r} + v \frac{\partial u}{\partial r} + \frac{v}{2} \left(\frac{\partial \omega}{\partial r} \right)^2 \right] \quad (\text{A.16})$$

Note that only stress components needed for this study are the tangential components as they are the crack driving stresses.

Verification of Results

In order to verify the results, the solution was checked with that of Timoshenko and Woinowsky-Krieger. Timoshenko and Woinowsky-Krieger consider the problem of a simply supported, centrally loaded circular plate with ν fixed at 0.3 and no overhang. The assumed displacement, u , and deflection, ω , functions of the Timoshenko and Woinowsky-Krieger solution are

$$u = (a_0 - r)(c_1r + c_2r^2 + c_3r^3 + c_4r^4 + \dots) \quad (\text{A.17})$$

$$\omega = \omega_0 (1 - r^2/a_0) \quad (\text{A.18})$$

where the c_i and ω_0 (maximum deflection) are undetermined coefficients and a_0 the supporting radius. The strain energy method was used to calculate the coefficients in the u and ω functions.

The resulting bending and membrane stresses obtained here for the case of no overhang (and $\nu = 0.3$) were compared with the Timoshenko and Woinowsky-Krieger solution. The solution for the center stresses for a 100 μm thick disk with E (Young's modulus) equal to 1114 GPa^[2] (that of CVD diamond) is compared to the Timoshenko and Woinowsky-Krieger approximation in Fig. A.2. In order to obtain sufficient correspondence (better than 1%) between Timoshenko and Woinowsky-Krieger and the solution obtained here it was necessary to take seven terms in the power series for u (eqn. A.10). Only tangential stresses are shown.

The center bending stress was omitted in the Timoshenko and Woinowsky-Krieger analysis; however, the small deflection stress solution from Roark and Young^[19] was used for the comparison in Fig. A.2 (denoted tangential bending stress-linear theory in Fig. A.2.). Both the tangential membrane stresses at the disk edge and the tangential bending

stresses at the disk edge obtained from this analysis matched the solution of Timoshenko and Woinowsky-Krieger very closely (better than 1%). In addition, the present analysis matches the small deflection tangential stress

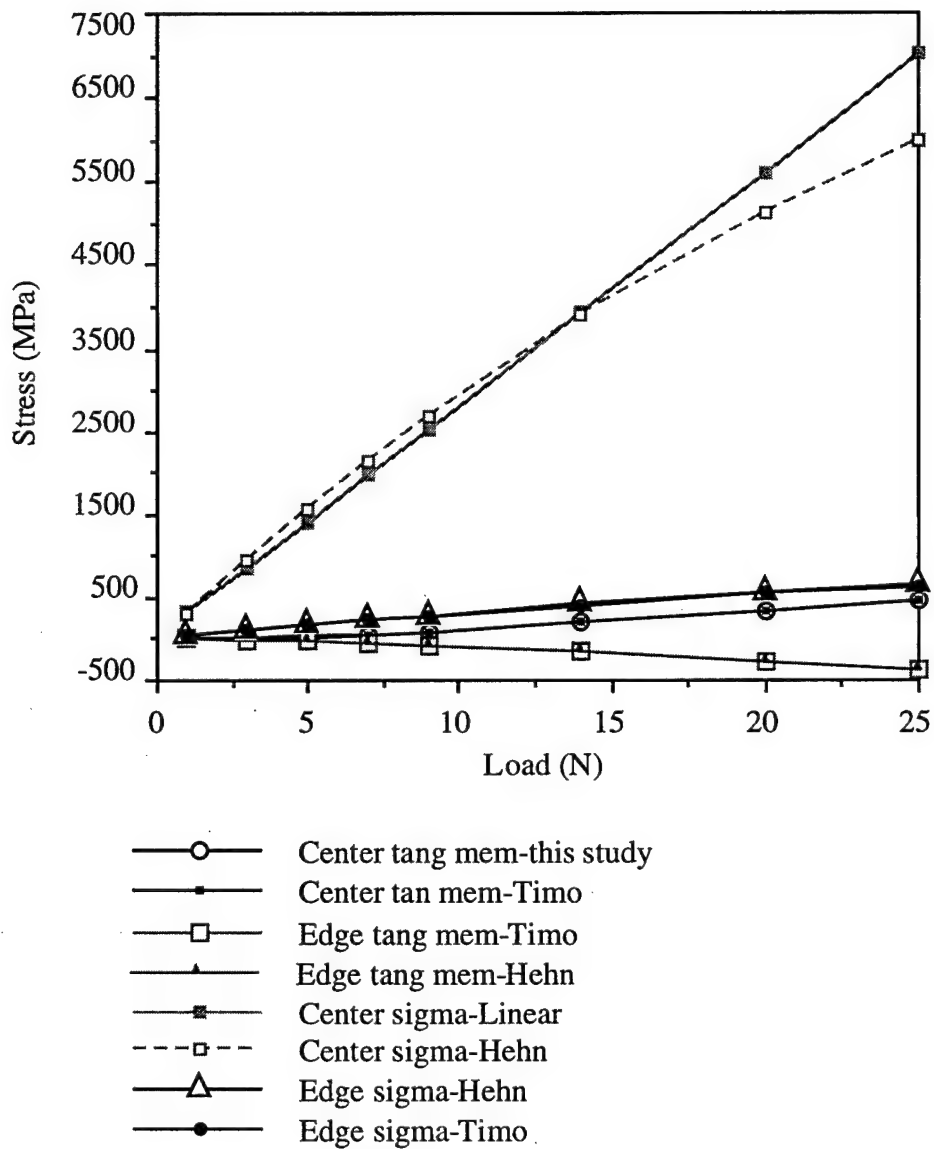


Fig. A.2 Comparison of solution obtained with this study and that of Timoshenko and Woinowsky-Krieger for the case of no overhang and $v = 0.3$.

solution of Roark and Young^[19] (linear theory) closely (better than 5%) until the load becomes sufficiently high enough to cause a large displacement deviation.

In the finite element method solution given by Stein,[61] the radial membrane stresses at the center of a centrally loaded, simply supported circular plate with no overhang was plotted for reduced variables (v , E , and the load P). Substituting the values for v , E , and P used in this study and measuring manually the radial membrane stresses (at the disk center) from the plots, the results of Stein differ from Timoshenko and Woinowsky-Krieger by less than 2%. Thus the accuracy of the method of Timoshenko and Woinowsky-Krieger is established and in addition, the results obtained here are verified by comparison with Stein and Timoshenko and Woinowsky-Krieger.

The computer generated solution obtained here for the case of no overhang compared well with the results of Timoshenko and Woinowsky-Krieger and Stein. Computer generated solutions including overhang were then obtained for the relevant problem of this study. The computer solution for the case of $v = 0.07$ and an overhang of 26% (which was the overhang in our testing configuration) for a range of loads is shown for a $100\mu\text{m}$ thick disk in Fig. A.3. The tangential bending stress of the computer solution deviates from the linear model (including overhang) of Shetty et al.[21] under much smaller loads than the Timoshenko and Woinowsky-Krieger no overhang solution (compare Fig. A.3 with Fig. A.2). The cause of this is either the large difference in Poisson's ratio ($v = 0.3$ in Timoshenko and Woinowsky-Krieger, and $v = 0.07$ in the present study) or the presence of the overhang.

The computer model was run for several disk radii between the actual disk radius used in this study (4.00 mm) and support ring radius (3.175mm). The results are shown in Fig. A.4. From Fig. A.4 it is clear that the overhang has a relatively small effect in comparison with the effect of the change in Poisson's ratio.

As with the linear model (including overhang) of Shetty et al.,[21] the membrane and nonlinear bending stresses of the computer solution also rapidly approach infinity as the disk center is approached. Since the stress is actually applied over a small area and not at a point, the center stresses (membrane and bending) were obtained in the same way as

the linear case, i.e., by substitution of the equivalent radius^[19] for the r variable when evaluating the center stress components (eqn. 2.11).

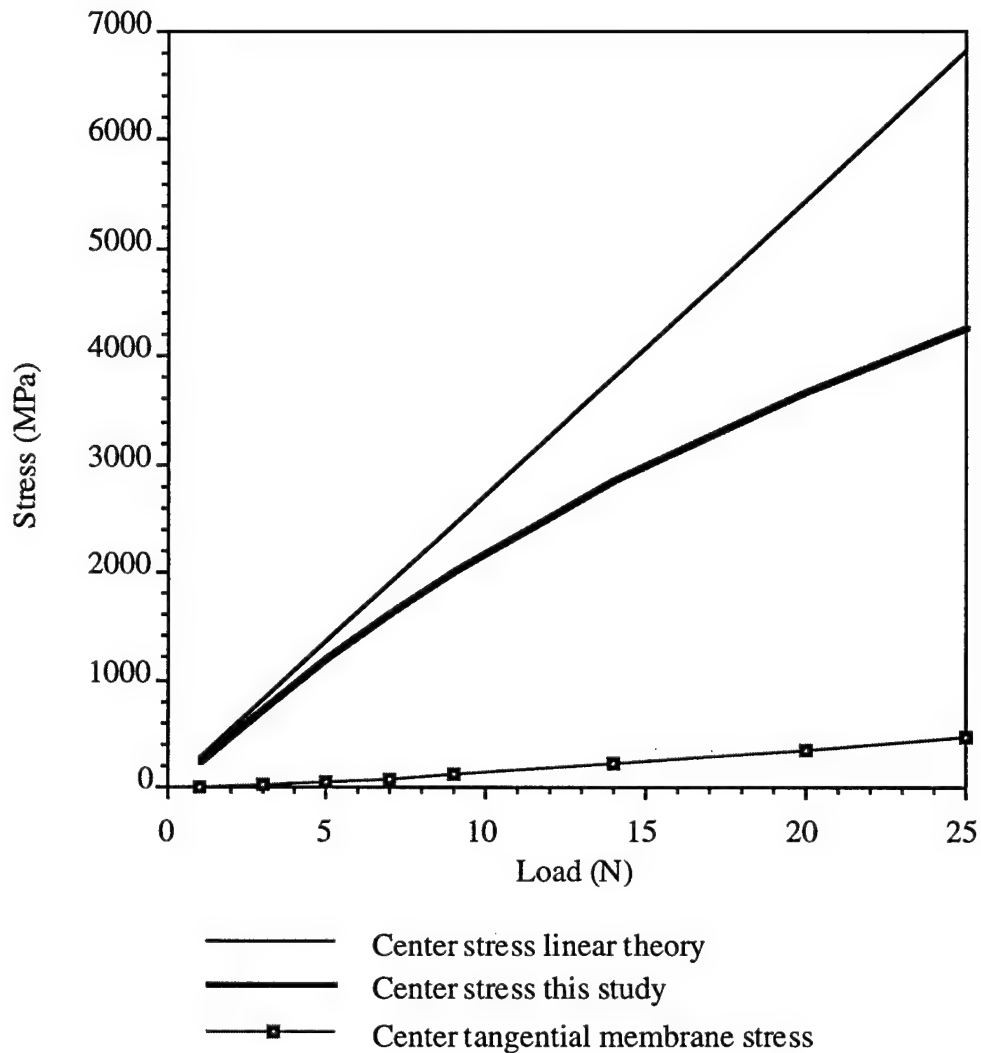


Fig. A.3 Comparison of computer generated solution of this study with linear theory for the case of 26% overhang and $v = 0.07$.

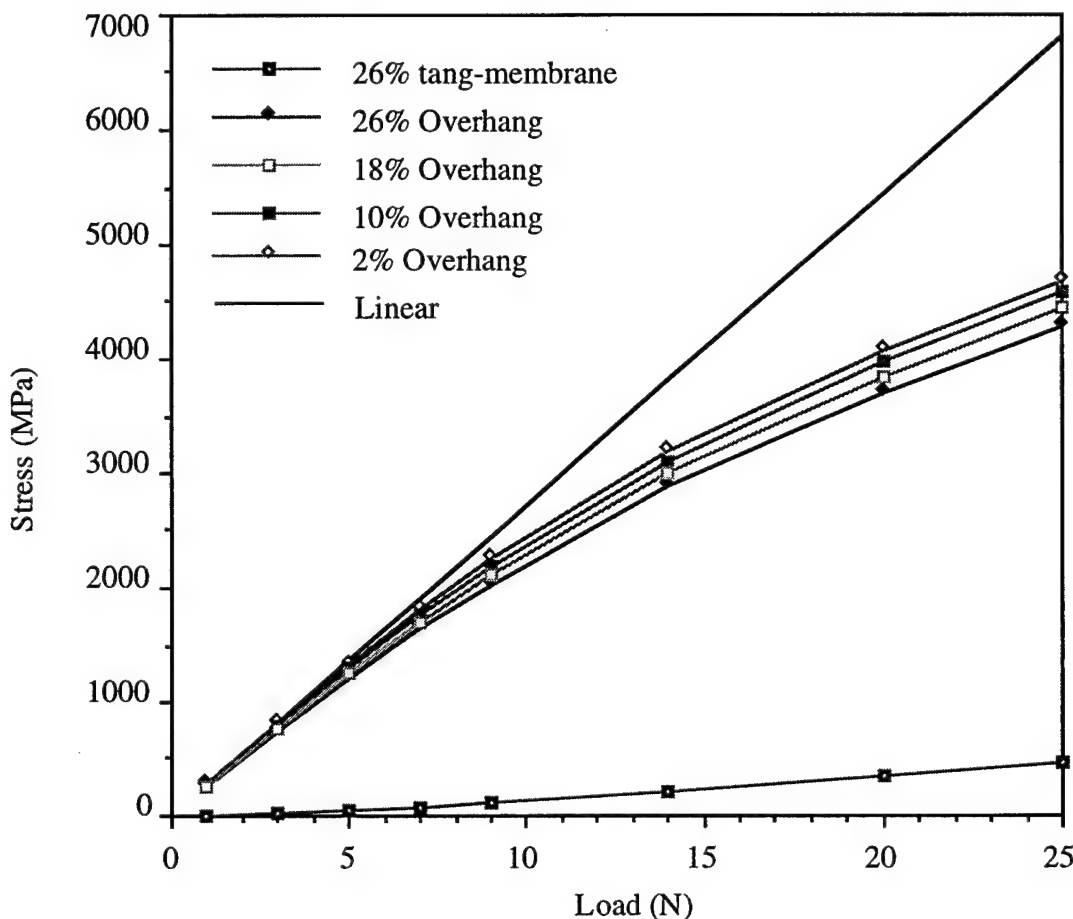


Fig. A.4 The effect of different levels of overhang on the stresses.

MathematicaTM Computer Program for Calculation of Stresses

The MathematicaTM computer program used to calculate the large deflection stresses is given below.

$t[0]=142 \cdot 10^{-6}$ (*Thickness in meters*)
 $a[0]=4.000 \cdot 10^{-3}$ (*Radius of disk in meters*)
 $a[1]=3.175 \cdot 10^{-3}$ (*Support ring radius in meters*)
 $p[0]=9.1616$ (*Load in Newtons*)
 $e=1000 \cdot 10^9$ (*Modulus in Pa*)
 $\nu=0.07$ (*Poisson's ratio of disk*)
 $b[0];$ (*Undetermined Center deflection*)
 $b[1];$ (*Undetermined deflection function coefficient*)
 $c[]'s;$ (*Undetermined displacement function coefficients*)
 $d[0];$ (*Coefficient of rigidity of disk*)

(*Program listed below*)

$r =$

$d[0]:=(e \cdot t[0]^3)/(12(1-\nu^2))$ (*Calculate rigidity*)

$u[r]:=c[1]r+c[2] r^2+(c[3] r^3)+$
 $c[4] r^4+c[5] r^5+c[6] r^6+c[7] r^7$

$w[r]:=b[0](1-(r^2)/(a[1]^2)+(r^2)b[1]\ln[a[1]]-(r^2)b[1]\ln[r]$

$gg[r]:=d[0](3.14159)((r)(D[w[r],{r,2}]^2)+(r^{-1})(D[w[r],r]^2)+$
 $+(2 \nu)(D[w[r],{r,2}])D[w[r],r])$

$j[r]:= \text{Expand}[gg[r]]$

$v1temp:=\text{Integrate}[j[r],\{r,x,a[0]\}]$

$v0=\text{Limit}[v1temp,x \rightarrow 0]$

$er[r]:= \text{Expand}[D[u[r],r]+(0.5)D[w[r],r]^2]$

$n[r]:= \text{Expand}[r er[r]^2]$

$l[r]:= \text{Expand}[u[r]er[r]]$

```

v3temp:=Expand[(12(3.14159)d[0]/t[0]^2)(n[r]+((r^1)u[r]^2)+2 nu l[r])]

v2temp:=Integrate[v3temp,{r,x,a[0]}]

v1=Limit[v2temp,x->0]

v2:=Expand[v1]

pi[r_]:=v2+v0-p[0]b[0]

eq1:=Expand[D[pi[r],c[1]]]==0

eq2:=Expand[D[pi[r],c[2]]]==0

eq3:=Expand[D[pi[r],c[3]]]==0

eq4:=Expand[D[pi[r],c[4]]]==0

eq5:=Expand[D[pi[r],c[5]]]==0

eq6:=Expand[D[pi[r],c[6]]]==0

eq7:=Expand[D[pi[r],c[7]]]==0

eq8:=Expand[D[pi[r],b[0]]]==0

eq9:=Expand[D[pi[r],b[1]]]==0

FindRoot[{eq1,eq2,eq3,eq4,eq5,eq6,eq7,eq8,eq9},
{c[1],1 10^-4},{c[2],-0.1},{c[3],-50},
{c[4],3000},{c[5],-5.0 10^6},{c[6],5 10^8},
{c[7],5 10^8},{b[0],50 10^-6},{b[1],-5.0}]

```

APPENDIX B
DATA SET A.I

Table B. 1 Data corresponding to the Texas Instruments study (set A.I).

Process run	t ($\pm 5\mu\text{m}$)	Load ($\pm 0.01\text{N}$)	σ_{Max} ($\pm 30\text{MPa}$)	r ($\pm 20\mu\text{m}$)	σ_{θ} ($\pm 30\text{MPa}$)	c ($\pm 5\mu\text{m}$)	a/b	KIC ($\pm 0.8\text{MPa}\sqrt{\text{m}}$)	L-D σ_{Max} ($\pm 30\text{MPa}$)	L-D σ_{θ} ($\pm 30\text{MPa}$)
1	82	1.962	825	2280	131	32	1.13	0.9		
1	110	3.021	668				1.60			
1	97	2.227	649							
1	120	3.021	552	932	190	23		1.1		
1	108	3.159	721							
1	97	2.256	651							
1	95	1.942	586							
2	100	2.473	674	516	298	35	1.81	2.2		
2	96	5.996	1787							
2	101	3.754	1001	380	501	30	1.70	3.4		
2	111	3.799	824	908	283	30	2.67	1.9		
2	96	2.847	776	2400	130	26	3.11	0.8		
2	93	2.198	702	1648	156	37	0.82	1.2		
2	98	2.820	803	1177	209	42	0.93	1.7		
2	116	3.603	709	650	292	41	1.13	2.3		
2	98	3.256	927	1300	221	47	1.04	1.9		
2	96	2.998	893							

Table B.1 continued

Process run	t ($\pm 5\mu\text{m}$)	Load ($\pm 0.01\text{N}$)	$\sigma_{\text{Max}}^{(\pm 30\text{MPa})}$	r ($\pm 20\mu\text{m}$)	$\sigma_{\theta}^{(\pm 30\text{MPa})}$	c ($\pm 5\mu\text{m}$)	a/b	KIC ($\pm 0.8\text{MPa}\sqrt{\text{m}}$)	L-D $\sigma_{\text{Max}}^{(\pm 30\text{MPa})}$	L-D $\sigma_{\theta}^{(\pm 30\text{MPa})}$
3	160	6.708	651	1083	213	54	1.10	1.9		
3	159	6.495	639							
3	129	5.036	785							
3	123	5.667	981							
3	141	5.151	661							
3	140	4.929	642							
3	124	4.066	692							
3	134	4.279	614							
3	121	3.559	639							
3	126	3.603	592	746	231	70	2.42	2.4		
4	226	9.733	440							
4	290	21.699	563							
4	312	20.009	441	914	188	78	1.20	2.1		
4	232	10.383	443							
4	272	14.057	421							
4	215	12.900	652							
4	269	21.415	657							
4	231	9.342	402							
4	271	13.968	422							
4	190	10.009	665	920	253	70	4.19	2.6		
5	54	0.952	992							
5	39	0.605	1275	424	520	19	1.00	2.2	833	407
5	33	0.605	1828						971	
5	35	0.560	1492						892	
5	69	2.562	1569						1317	
5	46	0.738	1089						842	

Table B.1 continued

Process run	t ($\pm 5\mu\text{m}$)	Load ($\pm 0.01\text{N}$)	σ_{Max} ($\pm 30\text{MPa}$)	r ($\pm 20\mu\text{m}$)	σ_{θ} ($\pm 30\text{MPa}$)	c ($\pm 5\mu\text{m}$)	a/b	KIC ($\pm 0.8\text{MPa}\sqrt{\text{m}}$)	L-D $\sigma_{\theta}^{\text{Max}}$ ($\pm 30\text{MPa}$)
5	39	0.649	1369	720	443	22	2.03	2.0	343
6	160	5.667	550	153	398	43	1.62	3.2	
6	208	8.123	441						
6	146	5.151	612	650	263	60	1.44	2.5	
6	226	11.103	502						
6	200	7.322	434						
6	255	12.838	444	688	209	143	1.00	3.1	
6	140	4.840	631						
6	134	5.036	722						
6	145	4.689	565						
6	187	7.037	484						
7	127	3.600	577						
7	113	2.766	572						
7	98	2.060	581						
7	127	3.649	585						
7	90	1.334	458						
7	152	4.895	532						
7	166	5.336	478	236	310	52	1.72	2.8	
7	161	5.424	519	295	312	49	2.42	2.7	
7	152	4.983	542						
8	118	6.052	1148	1252	328	42	0.90	2.6	
8	106	4.983	1195	484	549	20	1.16	3.0	
8	106	4.630	1111						
8	119	4.542	846						
8	102	4.179	1081						
8	95	3.924	1185						

Table B.1 continued

Process run	t ($\pm 5\mu\text{m}$)	Load ($\pm 0.01\text{N}$)	σ_{Max} ($\pm 30\text{MPa}$)	r ($\pm 20\mu\text{m}$)	σ_θ ($\pm 30\text{MPa}$)	c ($\pm 5\mu\text{m}$)	a/b	KIC ($\pm 0.8\text{MPa}\sqrt{\text{m}}$)	L-D $\sigma_{\theta}^{\text{Max}}$ ($\pm 30\text{MPa}$)	L-D σ_θ ($\pm 30\text{MPa}$)
8	87	3.237	1183							
8	95	3.894	1176							
9	278	16.469	468							
9	305	14.615	338							
9	331	15.126	291							
9	378	18.313	262							
9	400	19.128	241							
9	406	14.861	181	684	96	151	2.58	1.5		
9	431	19.481	208							
9	403	20.020	248							
9	425	20.020	220	463	139	138	2.32	2.0	513	
10	156	5.366	548						719	
10	102	2.962	766						747	
10	88	2.236	798							
10	217	8.720	431							
10	201	10.054	590	895	230	79	1.42	2.5	548	244
10	182	6.935	507							
10	211	8.897	468							
10	210	9.338	497	1040	180	66	1.66	1.8		
11	84	1.864	743	602	299	25	2.30	1.9	688	311
11	130	3.826	587						547	
11	124	3.208	546	413	275	39	2.70	2.1	508	282
11	69	0.981	601						552	
11	167	5.071	448							
11	68	1.099	685						632	
11	91	2.089	693							

Table B.1 continued

Process run	t ($\pm 5\mu\text{m}$)	Load ($\pm 0.01\text{N}$)	$\sigma_{\text{Max}}^{\text{r}}$ ($\pm 30\text{MPa}$)	$\sigma_{\theta}^{\text{r}}$ ($\pm 20\mu\text{m}$)	c ($\pm 5\mu\text{m}$)	a/b	KIC ($\pm 0.8\text{MPa}\sqrt{\text{m}}$)	L-D $\sigma_{\theta}^{\text{Max}}$ ($\pm 30\text{MPa}$)
11	91	1.903	631					647
11	69	1.157	699					
12	96	1.687	503					
12	77	1.422	686	1050	203	1.60	1.8	
12	129	3.109	485	106	375	54	2.02	3.4
12	182	4.718	345					
12	180	4.983	373					
12	94	1.795	555					
12	111	1.677	361					
12	51	0.696	807					
12	71	1.167	663					
13	38	0.441	984					
13	42	0.893	1603	625	565	15	1.58	2.1
13	34	0.441	1251	499	471	28	0.72	2.2
13	48	1.363	1800					
13	54	1.677	1719					
13	43	0.951	1590					
13	32	0.883	2772					
13	99	3.904	1078					
14	89	1.962	690					
14	67	1.511	986					
14	79	2.138	975	1121	277	45	1.38	2.3
14	79	1.962	894	270	482	15	0.95	2.3
14	87	2.050	757					
14	58	1.167	1026					
14	63	1.324	974					

Table B.1 continued

Process run	t ($\pm 5\mu\text{m}$)	Load ($\pm 0.01\text{N}$)	σ_{Max}^{r} ($\pm 30\text{MPa}$)	r ($\pm 20\mu\text{m}$)	σ_{θ}^{c} ($\pm 30\text{MPa}$)	c ($\pm 5\mu\text{m}$)	a/b	KIC ($\pm 0.8\text{MPa}\sqrt{\text{m}}$)	L-D σ_{Max} ($\pm 30\text{MPa}$)	L-D σ_{θ} ($\pm 30\text{MPa}$)
14	70	1.618	948							
14	86	2.266	849							
15	96	3.208	956	390	469	25	1.10	2.9		798
15	101	4.267	1138							
15	115	4.806	965							
15	142	9.162	1157	1270	340	78	1.76	3.7		
15	142	7.033	888	206	583	28	1.82	3.8		
15	64	2.619	1862							
15	79	3.472	1565							
15	93	3.747	1197							
15	101	4.355	1151							
16	312	21.619	476	909	204	131	1.24	2.9		
16	278	23.757	677	885	286	80	0.84	3.2		
16	55	1.334	1336							
16	238	15.037	606	521	319	59	1.21	3.0		
17	189	7.072	475	436	256	36	0.94	1.9		
17	177	5.071	394							
17	200	9.162	543							
17	195	6.670	418	224	286	52	1.20	2.6		
17	183	4.542	328							
17	222	8.759	410							
17	213	8.593	441							
17	185	7.808	547							
18	167	1.864	165							
18	180	4.002	300							
18	170	4.983	423	80	366	52	2.36	3.3		

Table B.1 continued

Process run	t ($\pm 5\mu\text{m}$)	Load ($\pm 0.01\text{N}$)	σ_{Max} ($\pm 30\text{MPa}$)	r ($\pm 20\mu\text{m}$)	σ_θ ($\pm 30\text{MPa}$)	c ($\pm 5\mu\text{m}$)	a/b	KIC ($\pm 0.8\text{MPa}\sqrt{\text{m}}$)	L-D σ_{θ} ($\pm 30\text{MPa}$)
18	144	3.924	480	333	270	62	1.54	2.6	
18	156	4.267	438	130	333	71	0.69	3.5	
18	130	2.903	442						
18	116	3.021	590						
18	131	4.041	605						
18	112	2.894	610						
18	90	1.981	673						
19	192	4.355	283						
19	189	5.601	376	111	309	58	1.53	2.9	
19	152	3.737	406						
19	177	4.453	346	130	269	71	1.52	2.8	
19	206	5.336	296						
19	130	3.306	503						
19	142	3.463	434						
19	122	2.815	493						
19	113	2.462	509						
20	94	943	943	318	498	30	2.02	3.4	
20	115	911	911						
20	148	862	862						
20	134	868	868	649	367	36	1.49	2.7	
20	151	805	805						
20	105	831	831						
20	86	1074	1074					991	
20	114	959	959						
20	85	1116	1116						1028

APPENDIX C
DATA SET A.II

Table C.1 Data corresponding to Group A sample set A.II.

Sample	t ($\pm 5\mu\text{m}$)	Load ($\pm 0.01\text{N}$)	$\sigma_{\text{Max}}^{\text{r}}$ ($\pm 30\text{MPa}$)	r ($\pm 20\mu\text{m}$)	$\sigma_{\theta}^{\text{c}}$ ($\pm 30\text{MPa}$)	c ($\pm 5\mu\text{m}$)	a/b	KIC ($\pm 0.8\text{MPa}\sqrt{\text{m}}$)	L-D σ_{Max} ($\pm 30\text{MPa}$)	L-D σ_{θ} ($\pm 30\text{MPa}$)
1	399	62,000	818	153	744	87	1.59	9		
2	210	17,644	972	290	664	87	1.39	8		
3	406	71,200	904	129	847	66	1.53	9		
4	215	20,178	1055	355	680	107	1.93	9		
5	589	587.556								
6	174	9,556	909	122	770	37	1.24	6		
7	391	97.067	1340	370	971	43	2.46	8		
8	194	20,400	1338	560	720	42	0.86	6		
9	303	45,556	1112	580	650	103	0.90	8		
10	312	43,333	932							
11	187	21,067	1491							
12	658	25,333	108							
13	43	2,044	3595						1766	
14	257	42,667	1426							
15	199	21,067	1308							
16	42	2,178	4033							1785

APPENDIX D
DATA SET A.III

Table D.1 Data corresponding to Group A sample set A.III.

Sample	t ($\pm 5\mu\text{m}$)	Load ($\pm 0.01\text{N}$)	σ_{Max} ($\pm 30\text{MPa}$)	r ($\pm 20\mu\text{m}$)	σ_{θ} ($\pm 30\text{MPa}$)	c ($\pm 5\mu\text{m}$)	a/b	K_{IC} ($\pm 0.8\text{MPa}\sqrt{\text{m}}$)	$L\text{-D}\sigma_{\text{Max}}$ ($\pm 30\text{MPa}$)	$L\text{-D}\sigma_{\theta}$ ($\pm 30\text{MPa}$)
1	160	3.02	286	23	287	55			2.6	
2	391	31.38	403	414	270	87			3.1	
3	302	7.29	167	97	159	72			1.7	
4	196	9.47	669	936	329	91			3.9	
5	217	4.44	251	497	156	54			1.4	
6	226	10.22	449	333	286	75			3.1	
7	262	8.67	274	196	213	58			2.0	
8	362	18.44	338							
9	188	4.44	344	2260	111	41			0.9	
10	218	4.44	249							
11	78	1.29	675	1660	221	23			1.3	
12	240	6.62	300							
13	250	9.02	374							
14	366	22.80	340							
15	226	5.64	248							
16	226	7.69	338							
17	433	13.33	136							

APPENDIX D
DATA SET A.III

Table E. 1 Data corresponding to Group B sample set B.I.

Sample	t ($\pm 5\mu\text{m}$)	Load ($\pm 0.01\text{N}$)	$\sigma_{\text{Max}}^{}$ ($\pm 30\text{MPa}$)	r ($\pm 20\mu\text{m}$)	$\sigma_{\theta}^{}$ ($\pm 30\text{MPa}$)	c ($\pm 5\mu\text{m}$)	a/b	KIC ($\pm 0.8\text{MPa}\sqrt{\text{m}}$)	L-D $\sigma_{\text{Max}}^{}$ ($\pm 30\text{MPa}$)	L-D $\sigma_{\theta}^{}$ ($\pm 30\text{MPa}$)
1	584	114.267	589	768	287	147			4.3	
2	584	112.311	579	64	579	114			7.7	
3	643	140.400	579	30	579	121			7.9	
4	641	140.933	586	70	586	110			7.6	
5	572	70.000	378	2605	82	200			1.4	
6	643	151.911	627	157	618	104			7.8	

Table E. 2 Data corresponding to Group B sample set B.II.

Sample	t ($\pm 5\mu\text{m}$)	Load ($\pm 0.01\text{N}$)	$\sigma_{\text{Max}}^{}$ ($\pm 30\text{MPa}$)	r ($\pm 20\mu\text{m}$)	$\sigma_{\theta}^{}$ ($\pm 30\text{MPa}$)	c ($\pm 5\mu\text{m}$)	a/b	KIC ($\pm 0.8\text{MPa}\sqrt{\text{m}}$)	L-D $\sigma_{\text{Max}}^{}$ ($\pm 30\text{MPa}$)	L-D $\sigma_{\theta}^{}$ ($\pm 30\text{MPa}$)
1	791	193.689	483	2518	75	109			1.0	
2	790	115.556	289	1555	90	172			1.5	
3	793	121.956	302	352	239	100			3.0	
4	832	117.200	260	2236	51	275			1.1	
5	765	94.622	255	2050	56	176			0.9	
6	733	171.333	519	31	287	108			3.7	
7	727	217.556	717	326	408	291			8.6	
8	701	196.844	585	441	492	128			6.9	
9	765	171.333	519	521	287	230			5.4	

APPENDIX E
DATA SET B

APPENDIX F RING-ON-RING DATA

Table F. 3 Data corresponding to Group B sample set B.III (broken elsewhere in ring-on-ring loading and donated for fracture surface analysis).

sample	t ($\pm 5\mu\text{m}$)	c ($\pm 5\mu\text{m}$)	a/b
1	832	163	0.83
2	880	88	1.06
3	876	69	1.73
4	914	159	2.10

REFERENCES

- [1] G. F. Cardinale and C. J. Robinson, *J. Mater. Res.* 6, 1432-37 (1992).
- [2] J. E. Field, The Properties of Natural and Synthetic Diamond, Academic Press, New York, 1992.
- [3] L. Hehn, Z. Chen, J. J. Mecholsky, Jr., P. Klocek, J. T. Hoggins, and J. M. Trombetta, *J. Mater. Res.* 9, 1540-45 (1994).
- [4] B. J. Feder, *Applied Optics* 29, 2976-77 (1990).
- [5] C. Johnston, A. C. Crossley, A. M. Jones, R.R. Chalker, F. L. Cullen, and I. M. Buckley-Golder, *Journal De Physique IV*, Colloque X2, Suppl. Au Journal De Physique II, 931-37, 1991.
- [6] B. S. Berry, W. C. Pritchett, J. J. Cuomo, C. R. Guarnieri, and S. J. Whitehair, *Appl. Phys. Lett.* 57, 302-3 (1990).
- [7] J. A. Baglio, B. C. Farnsworth, S. Hankin, G. Hamill, and D. O'Neil, *Thin Solid Films* 212, 180-5 (1992).
- [8] H. Windischmann, Glenn F. Epps, Yue Cong, and R. W. Collins, *J. Appl. Phys.* 69, 2231-37 (1991).
- [9] H. Chen, M. I. Nielsen, C. J. Gold, R. O. Dillon, J. DiGregorio, and T. Furtak, *Thin Solid Films* 212, 169-72 (1992).
- [10] D S. Knight and W. B. White, *J. Mater. Res.* 4, 385-393 (1989).
- [11] M. D. Drory, R. H. Dauskardt, A. Kant, and R. O. Ritchie, *J. Appl. Phys.* 78, 3083-8 (1995).
- [12] R. Rice, Fractography of Glasses and Ceramics II, Vol. 17, edited by V. D. Fréchette and J. R. Varner, American Ceramic Society, Westerville, OH, 509-45, 1991.
- [13] W.D. Kingery, H.K. Bowen, and D.R. Uhlmann, Introduction to Ceramics, John Wiley & Sons, New York, 1976.
- [14] M.F. Ashby and D.R. Jones, Engineering Materials I, Pergamon Press, New York, 1980.
- [15] R. W. Rice, S. W. Freiman, and J. J. Mecholsky, Jr., *J. Am. Ceram. Soc.* 63, 129-36 (1990).
- [16] G. R. Irwin, *J. Appl. Mech.* 29, 651-54 (1962).

- [17] P. N. Randall, ASTM Special Technical Publication 410, 88-125 (1967).
- [18] G. K. Bansal, J. Am. Ceram. Soc. 58, 87-88 (1975).
- [19] R. J. Roark and W. C. Young, Formulas for Stress and Strain, (6th ed.). McGraw-Hill, New York, 1989.
- [20] F. F. Vitman and V.P. Pukh, Aavodskaya Laboratoriya 29, 863-67 (1963).
- [21] D. K. Shetty, A. R. Rosenfeld, P. McGuire, G. K. Bansal, and Winston H. Duckworth, Ceram. Bull. 59, 1193-97 (1980).
- [22] J. E. Ritter, Jr., K. Jakus, A. Batakis, and N. Bandyopadhyay, Journal of Non-Crystalline Solids 38, 419-24 (1980).
- [23] R. R. Cook and B. R. Lawn, Comm. Am. Ceram. Soc. C, 200-1 (1983).
- [24] J. Y. Chan, unpublished Masters thesis, University of Florida (1996).
- [25] D. K. Shetty, A. R. Rosenfeld, and W. H. Duckworth, J. Am. Cer. Soc. 69 437-42 (1986).
- [26] D. K. Shetty, A. R. Rosenfeld, P. McGuire, G. K. Bansal, and W. H. Duckworth, Ceram. Bull. 59, 1193-97 (1980).
- [27] J. J. Mecholsky, Jr., S.W. Freiman, and R. W. Rice, J. of Mat. Sci. 11, 1310-1319 (1976).
- [28] S. W. Freiman, J.J. Mecholsky, Jr., and P. F. Becher, Fractography of Glasses and Ceramics II, Vol. 17, edited by V. D. Fréchette and J. R. Varner, American Ceramic Society, Westerville, OH, 55-78, 1991.
- [29] H. P. Kirchner and J. C. Conway, Jr., J. Am. Ceram. Soc. 70, 565-69 (1988).
- [30] Y. L. Tsai and J.J. Mecholsky, Jr., Int. J. of Fract. 57, 167-82 (1992).
- [31] G. R. Anstis, P. Chantikul, B. R. Lawn, and D. B. Marshall, J. Am. Ceram. Soc. 64, 533-38 (1981).
- [32] M. D. Drory, C. F. Gardinier, and J. S. Speck, J. Am. Ceram. Soc. 74, 3148-50 (1991).
- [33] N. V. Novikov and S. N. Dub, J. Hard Mater. 2, 3-11 (1991).
- [34] T. J. Valentine, A.J. Whitehead, R. S. Sussman, C. J. H. Wort, and G. A. Scarsbrook, Proceedings of the Diamond 93' Conference, Lisbon, Portugal (1993).
- [35] S. Timoshenko and S. Woinowsky-Krieger, Theory of Plates and Shells (2nd ed.). McGraw-Hill Book Company, New York, 1959.
- [36] A. C. Ugural, Stresses in Plates and Shells. McGraw-Hill Book Company, New York, 1981.

- [37] H. A. Hoff, K.A. Snail, A. A. Morrish, and J. E. Butler, Fractography of Glasses and Ceramics II, Vol. 17, edited by V. D. Fréchette and J. R. Varner, American Ceramic Society, Westerville, OH, 25-54, 1991.
- [38] R. Kao, N. Perrone, and W. Capps, *J. Am. Cer. Soc.* 54, 217-24 (1971).
- [39] J. J. Mecholsky, Jr., S. W. Freiman, and R. W. Rice, *J. Am. Cer. Soc.* 60, 114-17 (1976).
- [40] J. D. Sullivan and P. H. Lauzon, *J. of Mat. Sci.* 11, 247-248 (1986).
- [41] D. B. Marshall, B. R. Lawn, and P. Chantikul, *J. Mater. Sci.* 14, 2001-2012 (1979).
- [42] R. W. Rice and J. J. Mecholsky, Jr., *NRL Memorandum Report 4077*, 10-29 (1979).
- [43] R. W. Rice and J. J. Mecholsky, Jr., *NBS Spec. Pub.* 562, 351-378 (1979).
- [44] C. A. Johnson and W. T. Tucker, *Proceedings of the Twenty-Third Automotive Technology Development Contractors Coordination Meeting*, Society of Automotive Engineers, 265-269 (1986).
- [45] M. F. Ashby and D. R. H. Jones, Engineering Materials 2. Pergamon Press, Oxford, 1986.
- [46] G. A. Slack and S. F. Bartram, *J. Appl. Phys.* 46, 89-98 (1975).
- [47] C. V. Noyan and J. B. Cohen, Residual Stress: Measurement by Diffraction and Interpretation. Springer-Verlag, New York, 1987.
- [48] O. Iancu, D. Munz, B. Eigenmann, B. Scholtes, and E. Macherauch, *J. Am Ceram. Soc.* 73, 1144-52 (1990).
- [49] R. A. Winholtz and J. B. Cohen, *Austral. J. Phys.* 41, 189-96 (1988).
- [50] A. Abushasan, unpublished Ph.D. dissertation, University of Denver (1990).
- [51] L. Hehn, C. R. Hubbard, Z. Chen, and J. J. Mecholsky, Jr., *J. Mat. Sci.* 30, 1277-1282 (1995).
- [52] Y. M. Cheong and H. L. Marcus, Advances in Surface Treatments: Technology-Applications-Effects, Vol. 4. Pergamon Press, New York, 115-34 1987.
- [53] V.M. Hauk, R. W. M. Oudelhoven, and G.H.J. Vaessen, *Met. Trans. A*, 1239-49 (1982).
- [54] A. Brenner and S. Senderoff, *J. Res. Natl. Bur. Std.* 42, 105-31 (1949).
- [55] B. D. Cullity, Elements of X-ray Diffraction, (2nd ed.). Addison-Wesley, Reading, MA, 1978.

- [56] E.D. Specht, R.E. Clausing, and L. Heatherly, J. Mater. Res. 5, 2351-59 (1990).
- [57] H. Guo and M. Alam, Thin Solid Films 212, 173-179 (1992).
- [58] L. G. Schulz, J. Appl. Phys. 20, 1033-37 (1949).
- [59] C. Wild, N. Herres, and P. Koidl, J. Appl. Phys. 68, 973-83 (1990).
- [60] H. Dölle and J. B. Cohen, Metall. Trans. A, 159-71 (1980).
- [61] M. Stein, NASA Tech. Brief NASA TN D-3768 (1966).